MAGNETIC LOSS PHENOMENA IN FERROMAGNETIC MATERIALS

Prepared by

D. J. EPSTEIN

with the cooperation of:

N. G. Anantha
R. P. Hunt
J. F. Janak
B. Frackiewicz
W. F. Kelly
B. W. Lovell
A. J. Mac Millan
J. J. Judy

Magnetics Group
Laboratory for Insulation Research
Massachusetts Institute of Technology
Cambridge, Massachusetts

Contract No. AF 19(604)-5482

Project 5620

Task 56203

FINAL REPORT

July 1962

Prepared for

ELECTRONICS RESEARCH DIRECTORATE
AIR FORCE CAMBRIDGE RESEARCH LABORATORIES
OFFICE OF AEROSPACE RESEARCH
UNITED STATES AIR FORCE
BEDFORD, MASSACHUSETTS

Requests for additional copies by Agencies of the Department of Defense, their contractors, and other Government agencies should be directed to the:

ARMED SERVICES TECHNICAL INFORMATION AGENCY
ARLINGTON HALL STATION
ARLINGTON 12, VIRGINIA

Department of Defense contractors must be established for ASTIA services or have their "need-to-know" certified by the cognizant military agency of their project or contract.

All other persons and organizations should apply to the:

U.S. DEPARTMENT OF COMMERCE
OFFICE OF TECHNICAL SERVICES
WASHINGTON 25, D. C.

AFCRL-62-553

MAGNETIC LOSS PHENOMENA IN FERROMAGNETIC MATERIALS

Prepared by

D. J. EPSTEIN

with the cooperation of:

N. G. Anantha
R. P. Hunt
J. F. Janak
B. Frackiewicz
W. F. Kelly
B. W. Lovell
A. J. Mac Millan
J. J. Judy

Magnetics Group
Laboratory for Insulation Research
Massachusetts Inst tute of Technology
Cambridge, Massachusetts

Contract No. AF 19(604)-5482

Project 5620

Task 56203

FINAL REPORT

July 1962

Prepared for

ELECTRONICS RESEARCH DIRECTORATE
AIR FORCE CAMBRIDGE RESEARCH LABORATORIES
OFFICE OF AEROSPACE RESEARCH
UNITED STATES AIR FORCE
BEDFORD, MASSACHUSETTS

MAGNETIC LOSS IN FERROMAGNETIC MATERIALS

ABSTRACT

Studies have been made of a variety of unusual magnetic properties found in certain polycrystalline yttrium iron and lutetium iron garnets, namely: permeability relaxation, magnetic anneal, and a new type of hysteretic behavior.

The room-temperature permeability spectrum of these garnets is characterized by two regions of dispersion: one at microwaves, the other at r-f frequency. The former is identified as gyromagnetic in origin. The r-f dispersion exhibits a temperature-activated shift to lower frequency with decreasing temperature; the activation energy for this process is very nearly equal to that for the a-c resistivity.

Polycrystalline disks of these materials develop uniaxial magnetic properties when cooled to low temperature in a field. The anisotropy energy of the uniaxial effect can amount to about 20% of the first-order crystalline anisotropy constant.

In these same materials unusual hysteretic effects are found. A 60-cps loop taken at room temperature appears quite normal. As the temperature is lowered, normal behavior persists to ca. -100°C where the loop begins to develop some squareness. With a further decrease in temperature the rectangularity increases and at liquid-nitrogen some cores show almost perfect square-loop behavior. However, if, at this temperature, the excitation frequency is reduced, a critical frequency is reached at which the loop reverts to normal behavior. Thus, these materials are not square loop in the usual sense but exhibit "dynamic squareness," a phenomenon which is quite new.

The foregoing effects are explained in terms of a model in which it is presumed that we are dealing with a slightly off-stoichiometric garnet con-

taining some Fe^{2+} ions which replace Fe^{3+} ions in octahedral sites. The octahedral sites, therefore, basically comprise a system of Fe^{3+} ions to which additional electrons have been added. The observed magnetic effects can be explained by assuming that there is a preferred ordering of these electrons relative to the axis of spontaneous magnetization. At temperatures low enough to "freeze in" the ordering, a uniaxial magnetic axis develops. At somewhat higher temperatures, where electron diffusion can more readily occur, any sudden change in large-scale or local orientation of the magnetic axis is accompanied by a diffusion-controlled electron redistribution; the energy dissipated in this process appears as a magnetic loss term and leads to a relaxation in the permeability.

Detailed analysis of this loss mechanism reveals that a domain wall moving through a crystal is subjected to a viscous drag force that decreases with increasing wall velocity. For a 180° wall the drag drops to zero at finite wall velocity, at which point the wall becomes unstable. We attribute "dynamic squareness" to this effect.

Dynamic squareness can be deliberately produced in YIG by fabricating samples from oxide mixtures in which the ratio Y:Fe is deliberately made different from 3:5. In a series of ceramics prepared from prefired mixes $(3+x)Y_2O_3+(5-x)Fe_2O_3$, dynamic squareness is very pronounced for $x = \pm 0.1$, $x = -0.2$, and is evident for $x = +0.2, \pm 0.3, -0.4$. The electric and magnetic properties of this series, with $-0.4 \leq x \leq 0.4$, are described in some detail. The compositions $x = -0.3, -0.4$ have a permeability essentially independent of temperature from 20° to $250^{\circ}C$, and consequently may be of some technical importance.

The magnetostrictive properties of polycrystalline and single-crystal YIG have been measured. For the polycrystalline material we find for the

the saturation magnetostriction parallel to the direction of magnetization $\lambda_{s\text{-par}} = -2.5 \times 10^{-6}$. For the single crystal: $\lambda_{111} = -2.1 \times 10^{-6}$; $\lambda_{100} < 0.1 \times 10^{-6}$, $\lambda_{110} < 0.5 \times 10^{-6}$.

Two major instruments, developed under the contract, are described: one a vibrating sample magnetometer, the other an automatic torque magnetometer.

The following work peripheral to the major program was also carried out: (a) a detailed study of the electric and magnetic properties of V_2O_3 and related sesquioxides; (b) a study of the conductivity of TiO_2 at high temperature.

TABLE OF CONTENTS

MAGNETIC LOSS PHENOMENA IN FERROMAGNETIC MATERIALS

1. Introduction

It is well known that any dynamic magnetization process is inevitably accompanied by a certain amount of energy dissipation. In a metal, the magnetization losses arise from the flow of eddy currents induced by the time-varying magnetic flux. In nonmetallic materials, e.g. ferrimagnetic spinels and garnets, certain intrinsic losses, associated with the dynamic excitation of the spin system, are always present.

In both metals and nonmetals, additional losses may occur because of the presence of quasi-mobile impurities. A classic example of this sort is found in carbonyl iron. Here it has been well established that the carbon impurity atoms tend to occupy certain interstitial sites which are preferentially established by the magnetic axis.[1] A change in the direction of the spontaneous moment forces a redistribution of impurities -- a process which involves energy dissipation. This type of loss, frequently referred to as diffusion lag or diffusion aftereffect, is also found in certain spinels, where the role of the "impurity atom" is played by a quasi-mobile electron.[2,3] In these materials the magnetic axis establishes a preferential ordering of Fe^{2+} and Fe^{3+} cations; the change in ordering that accompanies a shift in the magnetic axis is effected by a transfer of an electron from Fe^{2+} to Fe^{3+}.

The subject contract was initiated shortly after it was discovered in the Laboratory for Insulation Research that diffusion lag occurred in slightly conductive samples of polycrystalline yttrium-iron and lutetium-iron garnet (YIG, LuIG). During the course of this contract we have examined in detail the way in which the basic lag mechanism affects a wide variety of magnetic properties in these garnets.

Samples used in our study were, for the most part, prepared within the Laboratory for Insulation Research. Techniques of preparation and compositions employed are described in Ch. 2 of the present report. In Ch. 3, measurements of a number of electrical properties of our samples are presented: dielectric

---

1 L. Néel, J. Appl. Phys., Supplement to Vol. 30, No. 4, 3S (1959).
2 H. P. J. Wijn and H. van der Heide, Revs. Mod. Phys. 25, 98 (1963).
3 D. J. Epstein, Conference on Magnetism and Magnetic Materials, A. I. E. E. Publication T-91, Feb. 1957.

constant and loss, conductivity, and thermoelectric power.

In garnets, as in spinels, the diffusion lag is responsible for relaxation behavior in the permeability spectrum. The lag mechanism provides a viscous-like drag on a moving domain wall. This drag, acting in combination with the spring-like restoring force, which restrains small-amplitude wall excursions, determines a critical frequency above which the wall will not follow the applied field. The drag force being diffusion controlled is strongly temperature-dependent and, consequently, the critical frequency for wall motion shifts markedly with the temperature. Our investigation of the permeability spectrum on YIG and LuIG is discussed in detail in Ch. 4.

In considering the implications of our model for diffusion lag it seemed reasonable to expect that if there were, in fact, a magnetically induced "impurity" ordering we might be able to freeze-in a preferential order, that would extend throughout the entire volume of a polycrystalline sample, by cooling to a sufficiently low temperature in a strong magnetic field. Indeed, precisely this effect was found; its manifestation is in the development of uniaxial anisotropy in a polycrystalline disk cooled in a field from room temperature to liquid nitrogen. The induced anisotropy can be quite strong, amounting in some cases to about 20 percent of the first-order crystalline anisotropy energy of the pure garnet. The experimental technique used to study magnetic anneal, the results obtained, and their interpretation are contained in Ch. 5.

In Ch. 6 a dramatically new magnetic effect is described. In garnets which show permeability relaxation and magnetic anneal, we find that the low-temperature hysteresis loop can be extremely "square," but the "squareness" only occurs above a critical frequency; below this threshold the loop reverts to a "normal" shape. We have coined the term "dynamic squareness" to describe this type of square-loop behavior. We attribute "dynamic squareness" to the same basic mechanism which accounts for diffusion lag. Analysis of the motion of domain walls damped by diffusion after-effect reveals that the damping force is a non-linear function of wall velocity. Indeed, for 180^{o} walls, conditions are such that for velocities in excess of a threshold value an increase in wall velocity results in a decrease in the diffusion-damping force. At this point the wall is no longer retarded in its motion by the diffusion drag and there is a discontinuous increase in velocity. It is unstable behavior of this sort which we believe to be responsible for dynamic squareness. Unstable behavior will not occur for 90^{o} walls.

It is clear that the high proportion of 180^{o} walls needed for "dynamic squareness" can be established by magnetic anneal. In an effort to obtain direct evidence of a field-induced preferential domain structure, the magneto-optical studies described in Ch. 7 were carried out. Using the Faraday effect we were able to see maze-type domain structures in polycrystalline samples approximately 1 mil thick. These patterns were probably strain determined. Attempts to relieve the strain by etching were of no avail; the samples were so thin that exposure to the etchant destroyed the sample before any basic change in the maze structure was noticeable.

In Ch. 8, measurements of magnetostriction on single-crystal and polycrystalline YIG are described. To our knowledge our results on single crystals are the first to be reported.

In our garnet samples it is likely that the quasi-mobile particle responsible for diffusion aftereffect is an electron, which, as in spinel, is transferred between Fe^{2+} and Fe^{3+} cations in octahedral sites; a correlation between conduction and diffusion lag is therefore to be anticipated. Accordingly, an investigation of the conductive properties of garnets was initiated in the early stages of the contract (see Ch. 3.) As the program evolved, our conductivity studies acquired a direction which had only an indirect relevance to our work on garnets. However, because these conductivity studies on V_2O_3 and TiO_2 are of sufficient interest in themselves, we feel that their inclusion as Ch. 9 of the present report is well warranted. The work on V_2O_3 is of particular interest because here for the first time it is established that the p-type conductivity characteristic of the room-temperature phase is an intrinsic property of the material and not a consequence of departure from stoichiometry. In contrast, the conductivity of V_2O_3 in its low-temperature modification is shown to be strongly dependent on the oxygen content. The properties of V_2O_3 as a valency-controlled semiconductor have also been examined.

Two major instruments were constructed under the contract. These, described in Ch. 10, include a vibrating-sample magnetometer and a self-balancing torque magnetometer. The former, designed for magneto-thermal studies over the temperature range from liquid helium to ca $875^{o}K$, will measure a magnetic moment down to about 3×10^{-3} emu. The torque magnetometer provides a direct chart record of torque vs. angle, and has been an invaluable tool in our magnetic-anneal studies.

2. MATERIALS PREPARATION

2.1 Compositions

It has been indicated in the Introduction that the variety of unusual magnetic effects (permeability relaxation, magnetic anneal, and dynamic squareness) observed in certain polycrystalline garnets can be explained in a consistent way by a diffusion after-effect model. The following chapters will document this point of view.

Essential to diffusion after-effect is the presence in the crystal lattice of a quasi-mobile particle. In our garnets, the magnetic and electrical data suggest that this particle is an electron which hops from Fe^{2+} to Fe^{3+}. In stoichiometric YIG and LuIG, however, iron is present only as Fe^{3+}; therefore, for Fe^{2+} to be present we must be dealing with a structure slightly deficient in oxygen. (A less likely possibility is that the quasi-mobile particle is a hole that is loosely bound to Fe^{3+}. In this case there would be magnetic ordering of Fe^{3+} and Fe^{4+} cations.)

In preparing materials for this study it was our objective to prepare compositions which on the one hand were precisely stoichiometric and on the other deviated from stoichiometry. In this way we sought to establish a correlation between composition and magnetic behavior. This objective, unfortunately, was only partially met. In general, we found that if we set out to make garnets in which diffusion-lag effects would occur we were invariably successful. However, if we endeavored to fabricate a stoichiometric garnet we were able to avoid diffusion lag only about half the time. The occurrence and absence of lag could be correlated with electrical resistivity; samples without lag would possess a d-c resistivity ordinarily a decade higher than those in which lag was found. We can only conclude that our conditions of preparation did not always allow for complete oxidation of iron.

To prepare garnets which were deliberately off composition we employed starting mixtures in which the ratio of rare earth to iron was altered from the stoichiometric ratio 3:5. For example, we prepared a series of materials corresponding to the prefired compositions $(3 + x)\ Y_2O_3 \cdot (5 - x)\ Fe_2O_3$, $-0.4 \leq x \leq +0.4$, with x varying in increments of 0.1. It is known from studies of the phase diagram for YIG (Fig. 2.1) that the structure will not tolerate much departure from stoichiometry; consequently, any excess of Y or Fe in the starting composition leads to the precipitation of phases other than garnet. Thus, for $x \neq 0$ we expect and find that the sintered product contains YIG plus foreign phases. (Indeed, even for $x \neq 0$ a foreign precipitate may form if conditions of firing are not correct.)

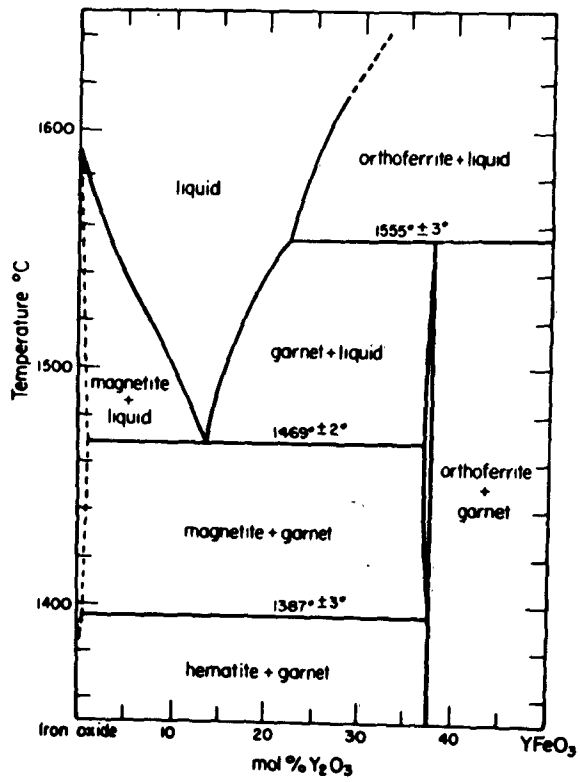

Fig. 2.1. Phase diagram for the system Fe_2O_3-Y_2O_3 in air."

The fact that for compositions with $x \neq 0$ we always found pronounced diffusion lag indicates that the use of off-stoichiometric ratios in the starting materials actuallyleads to the development in the multiphase ceramic of a garnet phase that deviated from its exact chemical formula.

2.2 Sample Preparation

Except for a few samples obtained from outside sources, the garnets used in the investigation were prepared by the Ceramics Group of the Laboratory for Insulation Research.

Most of our yttrium-iron garnet samples were prepared by the following method: The starting materials -- Cabot Corp. pyrogenic Fe_2O_3 (E - 7) * and Lindsay Chemical Co. Y_2O_3 (Code 1116) † -- were weighed to three decimal places (batches of approx. 250 grams total oxides) with an accuracy of ± 0.005 gm per constituent. These were dry milled in one-quart polyethyene bottles until a uniform color resulted; then denatured alcohol (1.5 ml/g of oxide) and 3/16" steel balls were added and the milling continued for 90 hours. The contents were next evaporated to dryness with infrared lamps, and the dried cake broken up and reacted at 1000°C for 2 hours in air. Upon cooling, 12 percent by volume (calculated) of Carbowax No. 4000, in trichloroethylene, was added as an aqueous solution, followed by granulation through a 20-mesh screen and drying overnight at 85°C.

The required shapes were pressed in steel dies at 15,000 p.s.i.; in some cases this was followed with hydrostatic pressing at 30,000 p.s.i. Sintering was at 50°C/hr temperature rise to 300°C, holding for 2 hours and then continuing to the peak temperature (1400°C-1450°C depending upon the specimens involved) which was held for 24 hours. Cooling was at 75°C/hr to about 850°C where normal furnace cooling took over. Oxygen enrichment was used in the firing cycle in some cases.

Our samples of lutetium-iron garnet were prepared by a procedure slightly different from the foregoing. Because the amount of Lu_2O_3 available to us was small, we felt that better mixing of the starting materials would be achieved by employing a chemical precipitation method rather than by straight ball milling. In this procedure Lu_2O_3 ** and "Puron" iron, †† in carefully weighed proportions, were dissolved in

---

* 99.48 percent Fe_2O_3, total oxide impurities< 0.2 percent, the remainder being volatiles.
† 99.97 percent Y_2O_3, the remainder being rare earth oxides.
Note: These analyses supplied by the manufacturers.
**We are indebted to the Contractor Officer for providing this material.
†† 99.95 percent Fe with carbon as the major impurity (Westinghouse Electric Corp.

HNO_3. Ammonia was added to the solution while stirring vigorously to facilitate complete precipitation. To ensure that nothing would be lost from the mix, no filtration was used. The whole mix was evaporated to dryness in the same evaporating dish, then ignited with a bunsen burner to drive off volatile decomposition products. The product was cooled, broken up to pass a 200-mesh screen and then reacted in air at 900°C for 24 hours in dense alumina crucibles. The garnet thus formed was ground again to pass a 200-mesh screen; 15 percent by volume Carbowax No. 4000 was added to aid in pressing (at 20,000 p.s.i.) the desired shapes. Sintering was according to the procedure described for YIG.

The specific YIG compositions prepared are listed in Table I. As mentioned previously, compositions deviating from the ideal were made in an attempt to force the Fe^{3+} ion into other valence states so that we might study the effect of this multivalency on magnetic relaxation processes. The garnet structure can only tolerate slight deviations from stoichiometry, as is evident from the phase diagram (Fig. 2.1); the compositions listed on the left in Table I are consequently not achieved upon sintering. Instead, we have a multicomponent system consisting of a parent garnet phase plus a precipitate which may be hematite, perovskite, or magnetite, depending on the starting materials and the condition of firing. The approximate amount of pure garnet to be anticipated is shown in the right-hand column of Table I.

Table I

Theoretical Composition $(3 + x)\ Y_2O_3 \cdot (5 - x)\ Fe_2O_3$	Excess Component oxide equivalents/mole
$x = -0.4$	0.867 ($Y_3Fe_5O_{12}$) +0.535 (Fe_2O_3)
$x = -0.3$	0.900 +0.400
$x = -0.2$	0.933 +0.265
$x = -0.1$	0.966 +0.135
$x = 0$	1.00 $Y_3Fe_5O_{12}$
$x = +0.1$	0.980 ($Y_3Fe_5O_{12}$) +0.080 (Y_2O_3)
$x = +0.2$	0.960 +0.160
$x = +0.3$	0.940 +0.240
$x = +0.4$	0.920 +0.320

The oxide equivalents are given here to show the amount of excess component which would theoretically be present. This should not be confused with phases actually present as shown by the phase diagram; excess Fe_2O_3 gives Fe_3O_4 and $Y_3Fe_5O_{12}$ between 1390°C and 1470°C, and excess Y_2O_3 gives $YFeO_3$ and $Y_3Fe_5O_{12}$ below 1555°C.

Near the end of the contract period we attempted to achieve valency control of the iron by chemical substitution and began the preparation of the composition series listed in Table II. This work had entered only its initial stages at the time the contract period expired.

Table II

Substituted YIG compositions

$Y_{3-x}Ca_xFe_5O_{12}$			$Y_3Fe_{5-y}Si_yO_{12}$	
x	Fe^{4+}		y	Fe^{2+}
0.005	0.005		0.005	0.005
0.010	0.010		0.010	0.010
0.020	0.020		0.020	0.020
0.040	0.040		0.040	0.040
0.160	0.160		0.160	0.160

2.3 Microstructure, X-ray and Magnetic Analysis

The ceramic garnets prepared according to the methods of Sec. 2.2 were of high density and were ordinarily free of cracks and large-scale voids.

Sintered bodies of YIG prepared from prefired compositions x = 0 had densities in excess of 98 percent of theoretical. Metallographic examination revealed a reasonably well developed grain structure with an average particle size of about 15 microns. In some samples there was evidence of a precipitate (probably $YFeO_3$) along grain boundaries.

For the compositions x = 0.1, -0.1 the grain structure was similar to that for x = 0. For larger deviations from stoichiometry there was a progressive decrease in particle size and a deterioration in the grain structure, the deterioration being more rapid on the excess yttrium side than for the prefired compositions rich

in iron. Occasionally, for x = 0 and for compositions slightly rich in iron, large grains (ca. 50 microns) were found.

X-ray powder patterns for the composition x = 0 revealed only the garnet phase. As we have indicated, the microstructure showed evidence of a foreign phase in this composition, but apparently the amount present was below the limit of X-ray detectability.

For compositions $x > 0$, the X-ray results indicated that both YIG and the perovskite, $YFeO_3$, were present. On the iron-rich side, $x < 0$, the powder patterns showed the presence of $YFeO_3$ and Fe_3O_4, in addition to YIG.

The X-ray results are confirmed by the data on saturation magnetization shown in Fig. 2.2. For compositions $x > 0$ the magnetic data is satisfactorily explained if it is assumed that the excess yttrium leads to the formation of the non-magnetic $YFeO_3$ as a precipitate. For $x > 0$, the magnetic moment lies below the curve calculated on the assumption that all excess iron precipitates as magnetite. We can interpret this situation as implying that a non-magnetic phase is also precipitated. The X-ray data indicates that this additional phase is $YFeO_3$.

3. ELECTRICAL PROPERTIES OF GARNETS

3.1 Resistivity and Thermoelectric Power

The results of d. c. resistivity measurements on polycrystalline garnets having the prefired composition $(3 + x)\ Y_2O_3 \cdot (5 - x)\ Fe_2O_3$ are shown in Figs. 3.1 and 3.2. The temperature of 100°C was selected for these measurements in order to avoid spurious surface conductivity due to absorbed water vapor.

For a given series of samples similarly prepared and fired, the maximum resistivity is obtained for the composition x = 0. However, the magnitude of the peak ρ is not reproducible and may vary by about 1 decade. The unusual magnetic effects that are described in subsequent chapters are found only in those YIG samples having a d. c. resistivity (at 100°C) below about 10^{11} ohm-cm.

As shown in Fig. 3.2, the resistivity as a function of temperature has the thermally activated behavior typical of a semiconductor. *

---

* For the data of Fig. 3.2 the activation energy is 1 ev. From one run of samples to the next there can be considerable scatter in the data for both resistivity and activation energy; scatter will occur even within a given run. Activation energies for the d. c. resistivity are typically in the range 0.5 to 1 ev. In Ch. 4 we point out that the resistivity and the activation energy are functions of frequency.

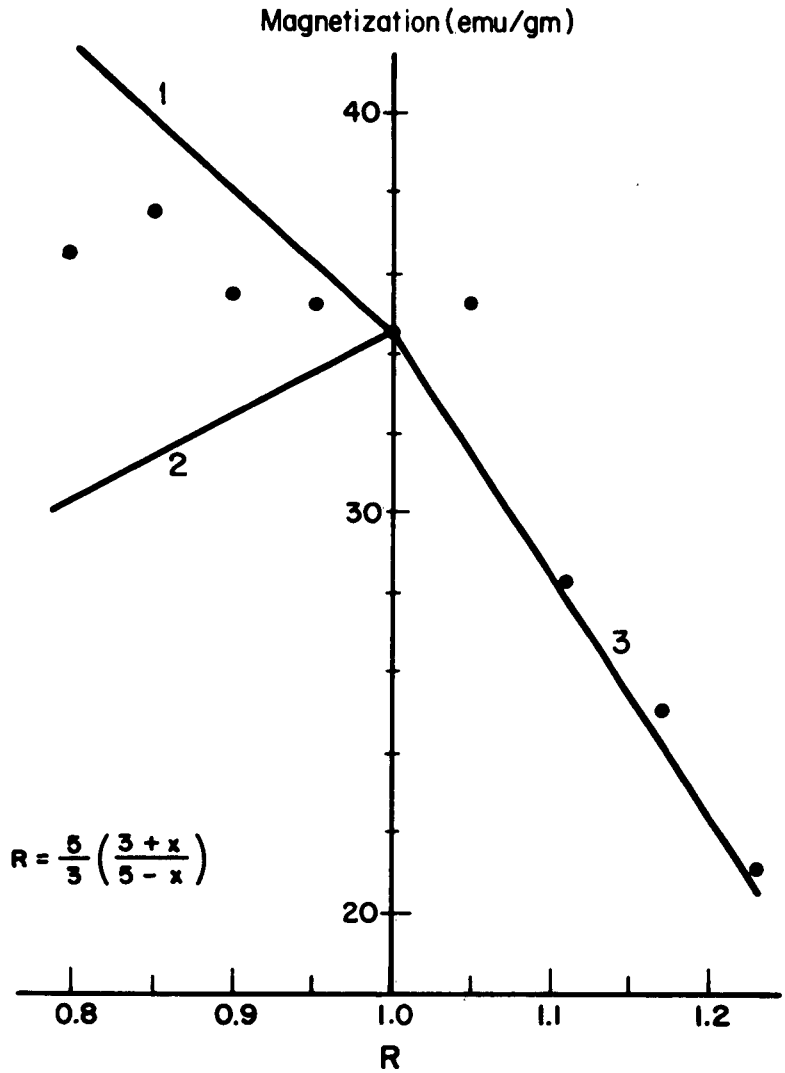

Fig. 2.2. Saturation magnetization of ceramic garnets at -196°C. Points are experimental; curve (1) is based on the assumption that excess iron precipitates as magnetite; for curve (2) excess iron is assumed to precipitate as hematite; for (3) excess yttrium precipitates as $YFeO_3$.

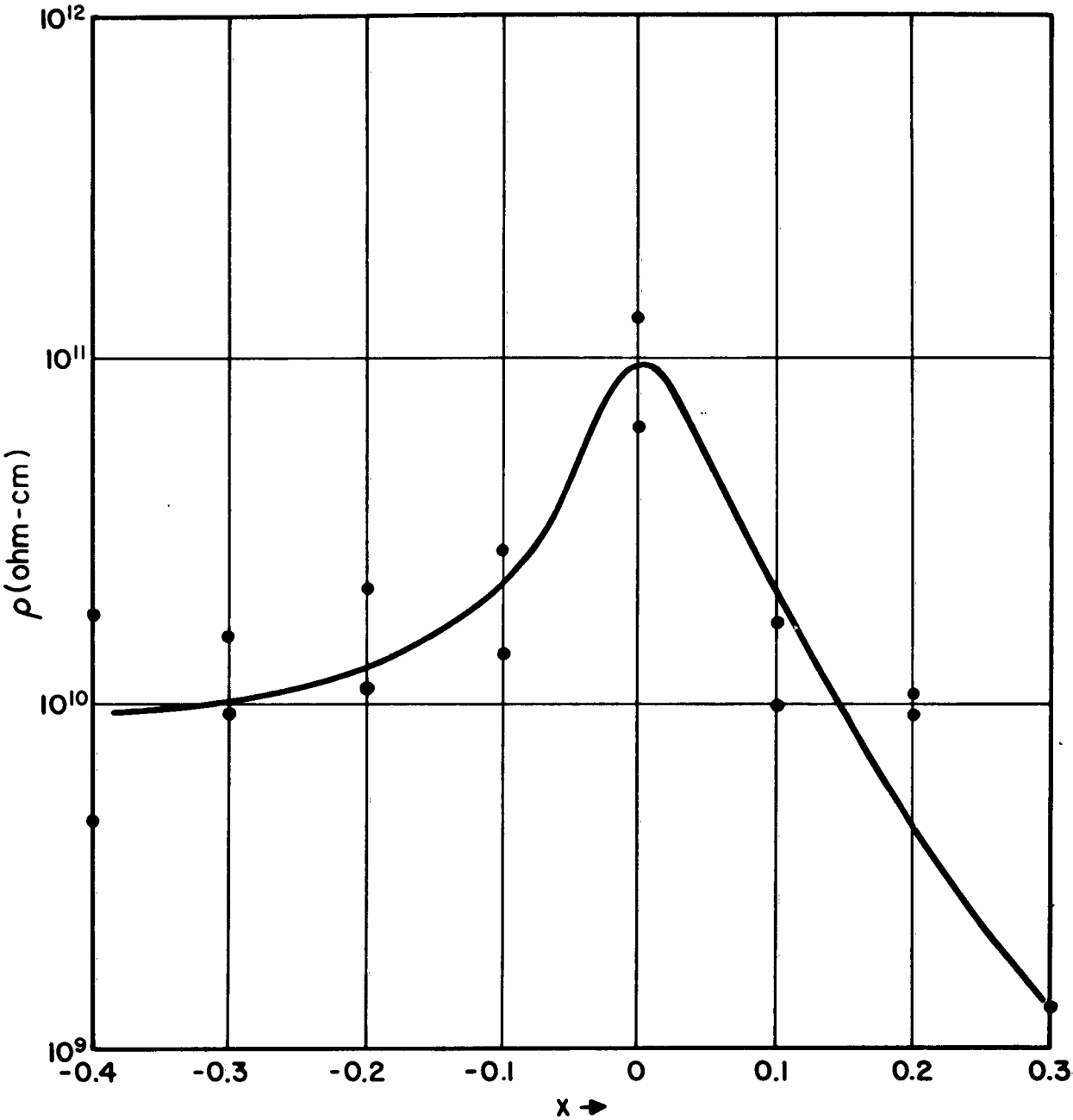

Fig. 3.1. D-c resistivity for series $(3+x)Y_2O_3 \cdot (5-x)Fe_2O_3$ at 100°C. Data shown are for two samples of each composition.

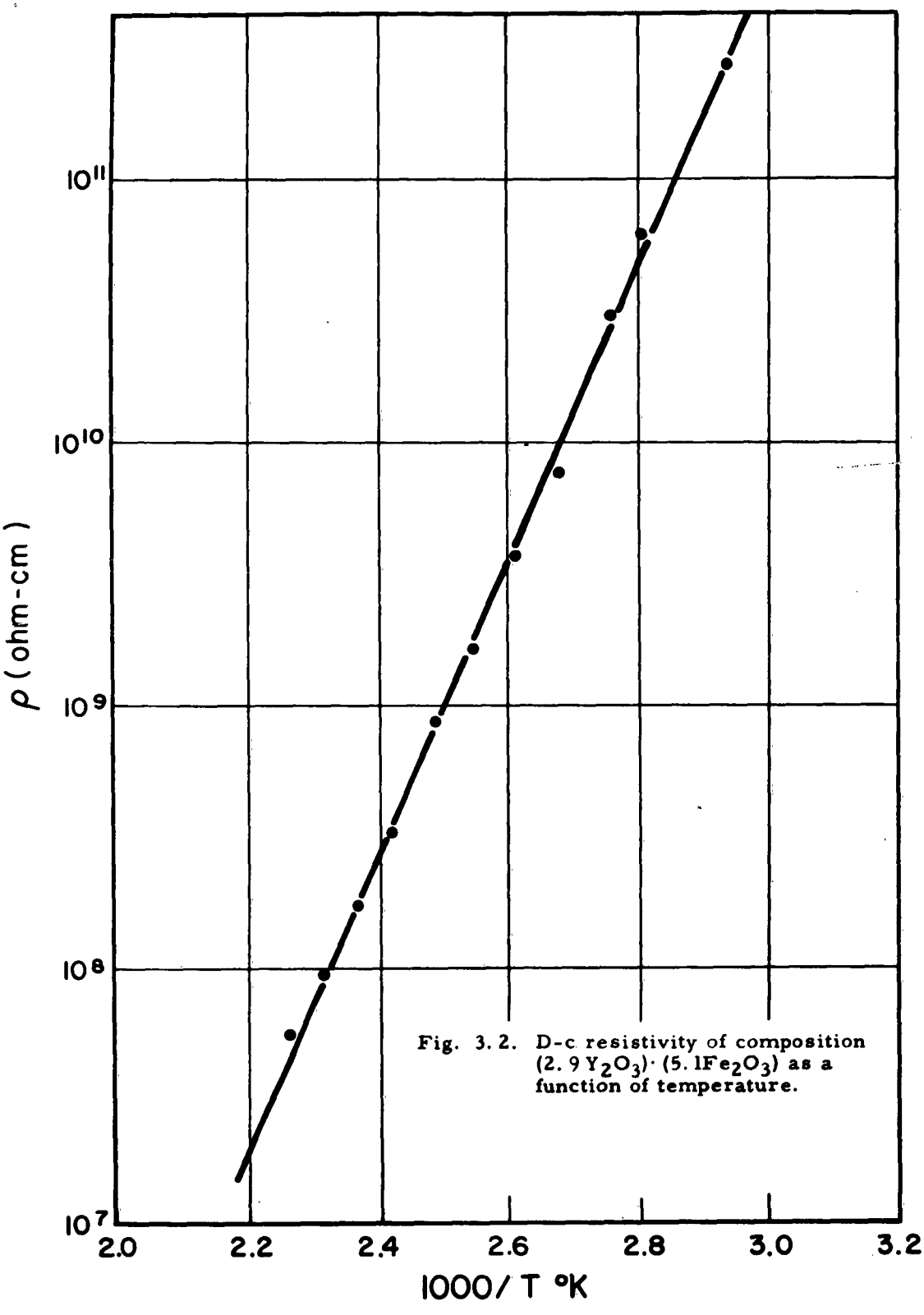

Fig. 3.2. D-c resistivity of composition $(2.9\,Y_2O_3)\cdot(5.1Fe_2O_3)$ as a function of temperature.

Measurements of Seebeck coefficient (Fig. 3.3) indicate that conduction is n-type for $|x| \lesssim 0.3$.

The electrical data is difficult to interpret because of the precipitates that readily occur in this system. Even small amounts of precipitate can have a pronounced effect on the d. c. electrical properties.

The apparatus used for resistivity and thermoelectric measurements is shown in Fig. 3.4. The top and bottom plates of the holder can be maintained at any desired temperature between 20°C and 200°C by pumping silicone oil through the copper tubing, the temperature of the coil being controlled by a bi-metallic regulator. The teflon disc used as an electrical insulator between top and middle plates is gold plated on its flat surfaces to minimize spurious surface charge effects. The sample is placed between pure silver contacts embedded in the surfaces of the middle and bottom copper plates. To avoid stray electrostatic voltages, the top and bottom plates are connected to a grounded cylindrical shield placed around the electrode system.

Resistivity is determined by the voltmeter-ammeter method, the voltage across the sample being measured by a vibrating-reed electrometer having an input resistance of about 10^{16} ohms. This same electrometer is used to measure the Seebeck voltage which appears across the sample when a thermal gradient is established between top and bottom plates of the sample holder.

3.2 Dielectric Properties

Dielectric properties of the series $(3 + x)\ Y_2O_3 \cdot (5 - x)\ Fe_2O_3$ were measured at 1 KC over the range 20°C to liquid-nitrogen temperature. The dielectric behavior reflects the fact that as we depart from the composition $x = 0$ the sintered product becomes more heterogeneous and, accordingly, both the dielectric constant (Fig. 3.5) and loss (Fig. 3.6) increase because of the enhanced role of interfacial effects[4] in the polarization process.

A comparison of Fig. 3.6 with the d. c. resistivity data shown in Fig. 3.1 will reveal that the 1 KC resistivity has fallen considerably from the d. c. value, the fall-off being less pronounced for the composition $x = 0$ than it is for the other members of the series.

---

[4] A. R. Von Hippel, "Dielectrics and Waves," John Wiley and Sons, Inc., New York (1959), Ch. 31.

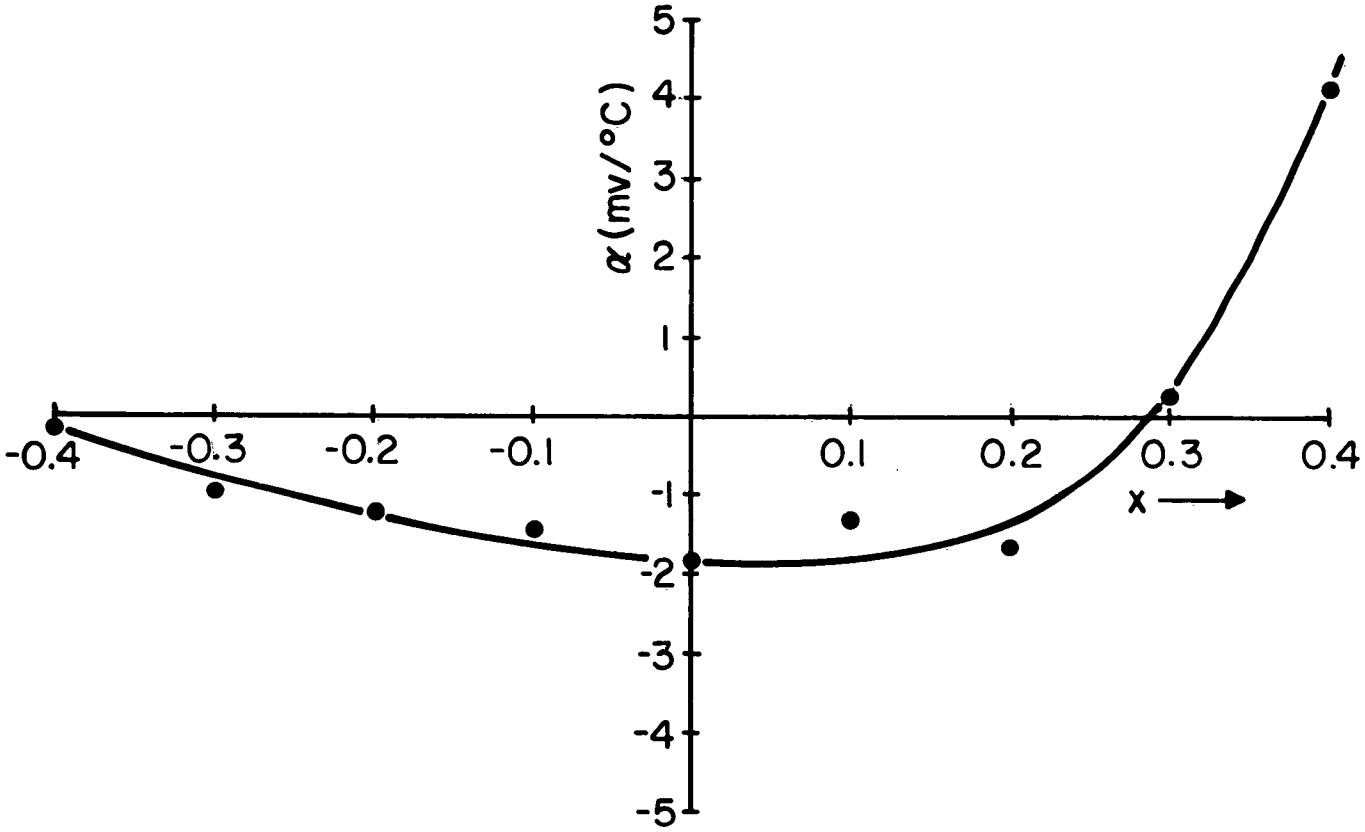

Fig. 3.3. Seebeck coefficient of series $(3+x)Y_2O_3 \cdot (5-x)Fe_2O_3$; mean temperature of sample 50°C.

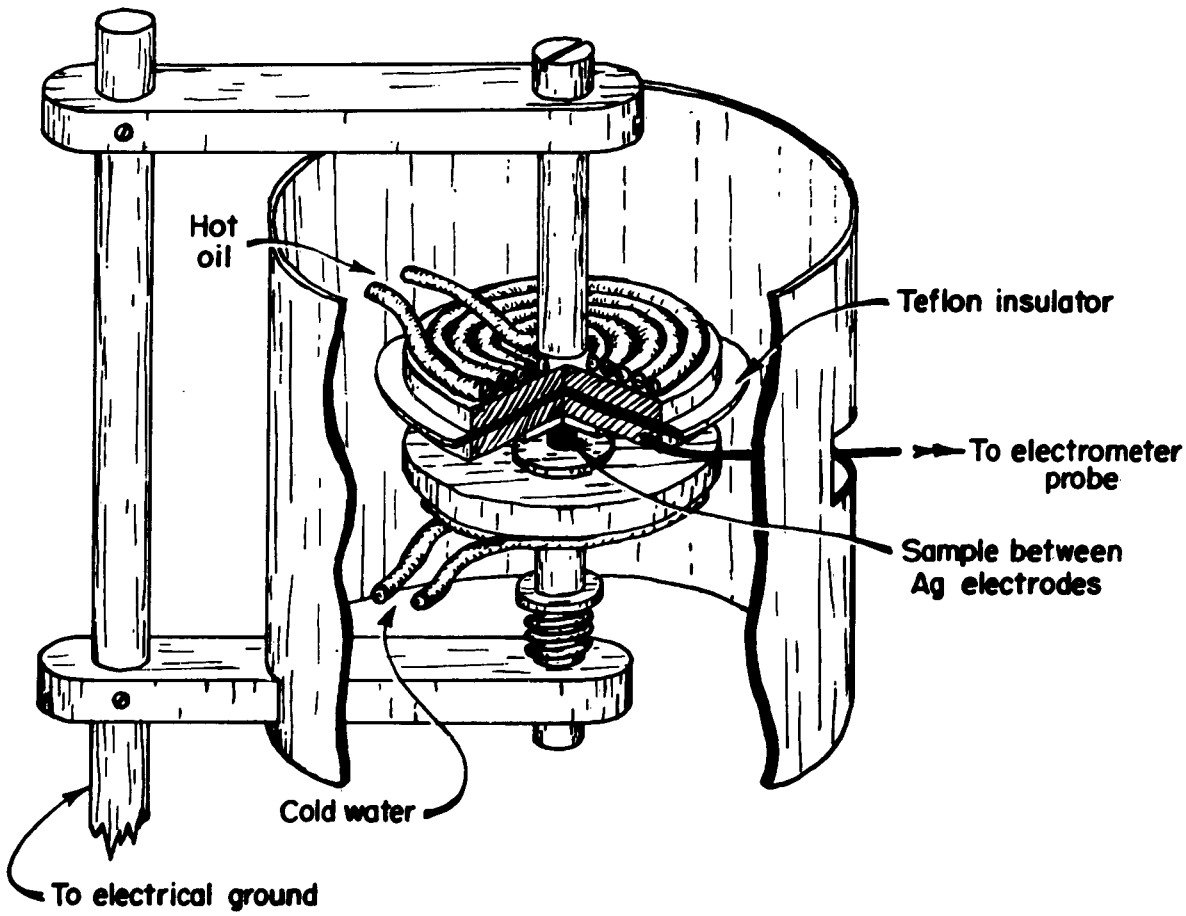

Fig. 3.4. Sample holder for resistivity and thermoelectric measurements.

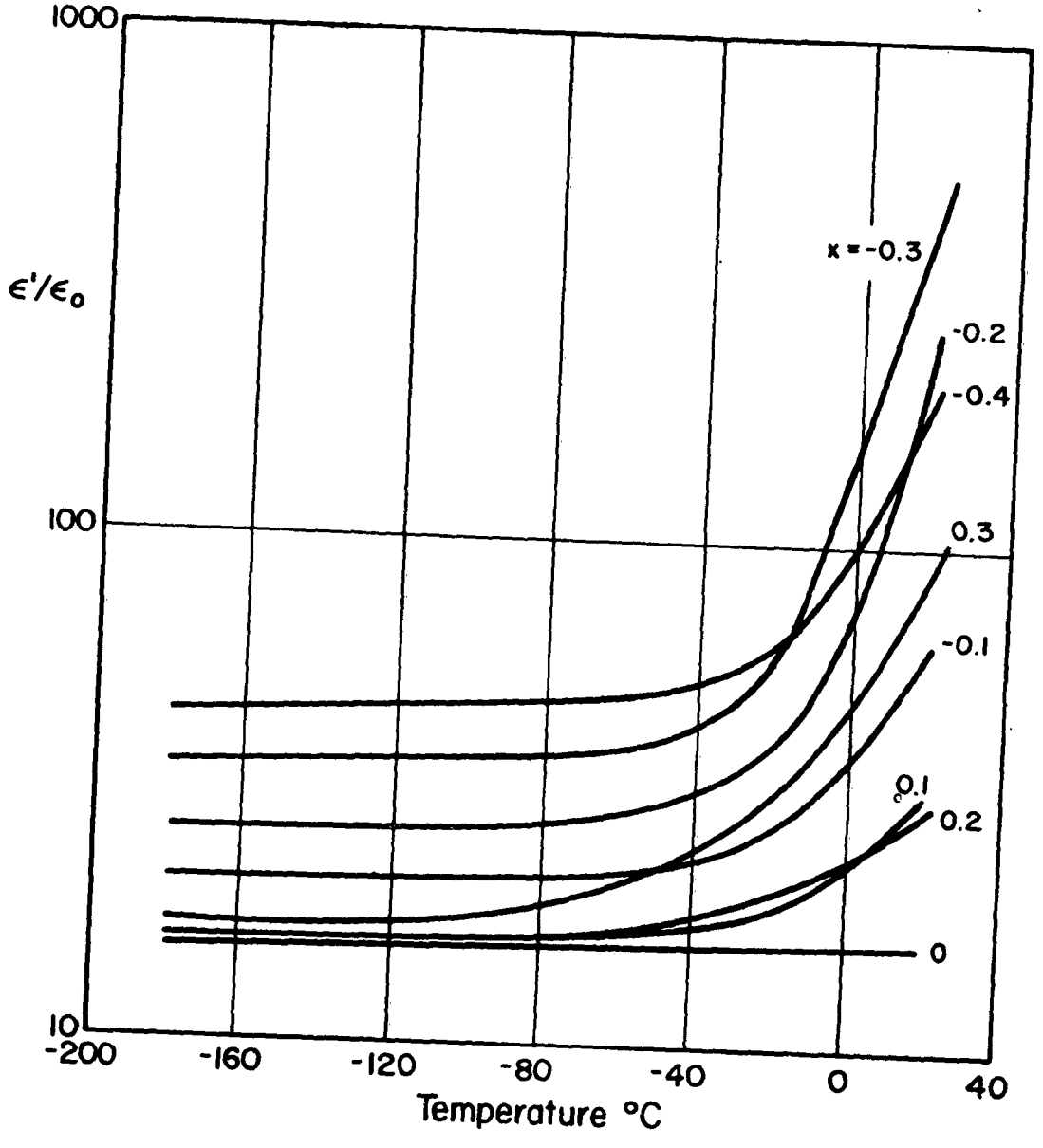

Fig. 3.5. Dielectric constant vs. temperature for series $(3+x)Y_2O_3 \cdot (5-x)Fe_2O_3$. Measurements at 1000 cps.

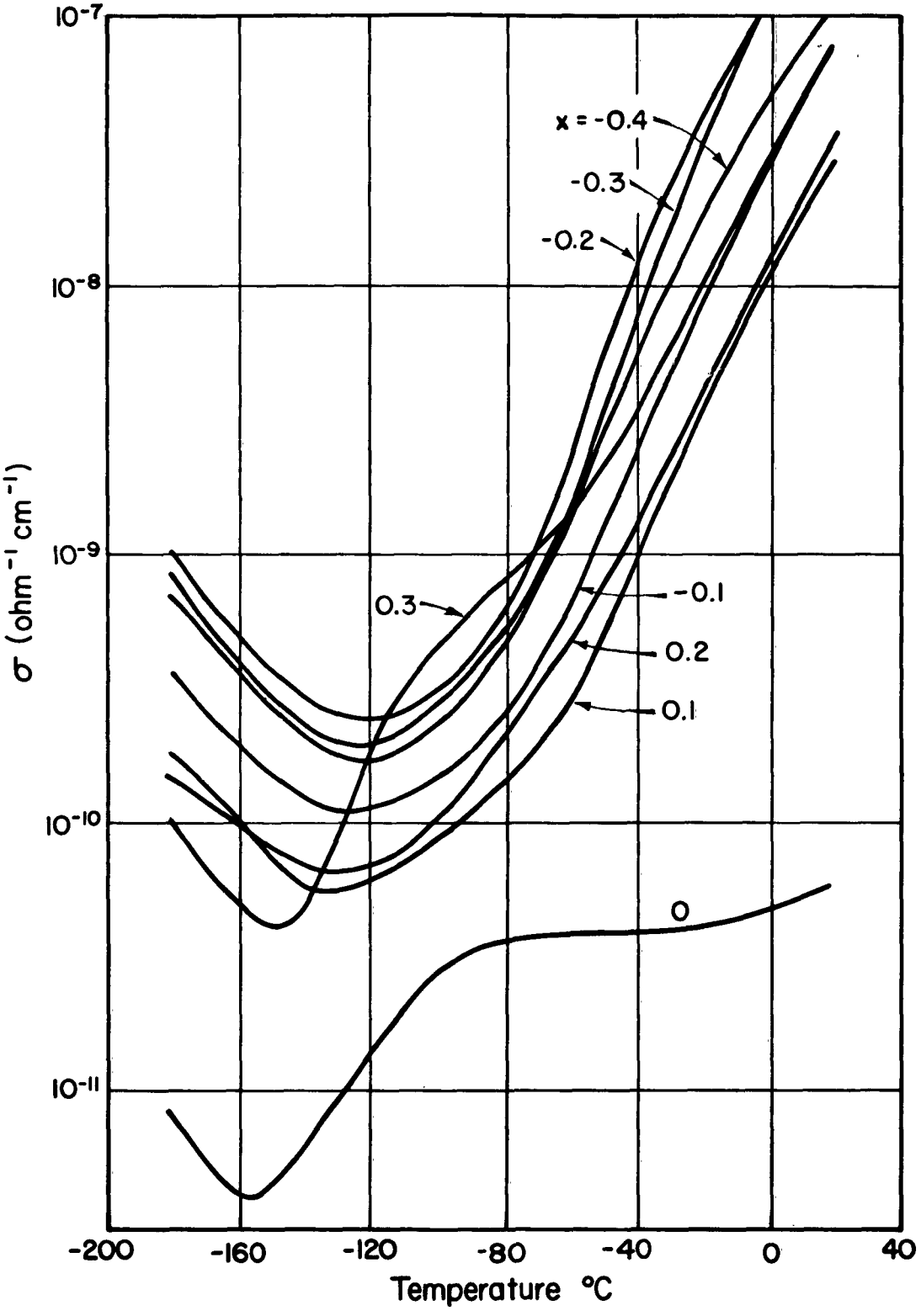

Fig. 3.6. Dielectric conductivity vs. temperature for series $(3+x)Y_2O_3 \cdot (5-x)Fe_2O_3$ at 1000 cps.

The occurrence of increased dispersion in conductivity with an increase in heterogeneity is typical of the interfacial polarization mechanism.

4. PERMEABILITY SPECTRA

4.1 Mechanism for Initial Permeability

The initial permeability of a magnetic material arises in two distinct ways: from domain-boundary displacements and from the reorientation of the magnetization vector within the individual domains. Although both mechanisms can and do occur simultaneously it is convenient, for analysis, to treat them separately.

The reorientation of the magnetization vector within a domain proceeds under the influence of two main torques. One arises from the crystalline anisotropy energy and tends to keep the spontaneous magnetization $\overline{M}_s$ in line with the easy direction of magnetization; the other is established by the external magnetic field. For an external field applied at right angles to the easy direction it is readily shown[5] that the static susceptibility is

$$\chi_{\perp s} = \frac{\mu_o M_s^2}{2\alpha K} \qquad (4.1)$$

where K is the first order anisotropy constant and α is a number. In a material with an easy direction along $[100]$, $\alpha = 1$; when $[111]$ is the easy direction, $\alpha = -\frac{2}{3}$

For a polycrystalline material, or a multidomain crystal, it becomes necessary to average Eq. 4.1 over all orientations of field and easy direction. For non-interacting domains, and for torques caused only by the external and anisotropy fields, the average rotational susceptibility for a random distribution is[5]

$$\chi_{s\text{-rot}} = \frac{2}{3} \quad \chi_{\perp s} \qquad (4.2)$$

To find the susceptibility as a function of the excitation frequency, it is necessary to solve an appropriate equation of motion for the system of magnetic

---

[5] J. Smit and H. P. J. Wijn, "Ferrites," John Wiley and Sons, N. Y. (1959), p. 244

spins. Such a calculation has been carried out by Kittel,[6] who takes as a starting point the equation of motion due to Landau and Lifshitz,[7] and finds that

$$\frac{\chi^{*}_{\text{rot}}(\omega)}{\chi_{\text{s-rot}}} \approx \frac{\dfrac{1+\mu_o\lambda}{\omega_o\ \chi_{\text{s-rot}}}\left(\dfrac{j\omega}{\omega_o}+\dfrac{\mu_o\lambda}{\omega_o\ \chi_{\text{s-rot}}}\right)}{1+\left(\dfrac{j\omega}{\omega_o}+\dfrac{\mu_o\lambda}{\omega_o\ \chi_{\text{s-rot}}}\right)^2} \tag{4.3}$$

where λ is the Landau-Lifshitz damping parameter and ω_o is the undamped resonance of the spin system. (We use the asterisk to denote that $\chi(\omega)$ is a complex number.) It can be shown that

$$\omega_o = \mu_o \gamma \frac{2\alpha K}{\mu_o M_s} \tag{4.4}$$

where γ is the magnetomechanical ratio.

Eq. 4.3 reveals that the susceptibility is characterized by a resonance behavior. The sharpness of the resonance is determined by the parameter

$$Q = \frac{\omega_o\ \chi_{\text{s-rot}}}{\mu_o \lambda} = \frac{2}{3}\left(\frac{M_s}{\lambda}\right) \tag{4.5}$$

When $\lambda \ll M_s$, Q is large, and in the limit $\lambda / M_s \to 0$ the susceptibility is governed by the relation

$$\chi_{\text{rot}}(\omega) = \frac{\chi_{\text{s-rot}}}{1-\dfrac{\omega^2}{\omega_o^2}} \tag{4.6}$$

In the other limit, $\lambda >> M_s$, we find that the average rotational susceptibility

---

[6] C. Kittel, Colloques Internationaux, CNRS 28, 184 (1951).
[7] L. Landau and E. Lifshitz, Physik Z. Sowjetunion 8, 153 (1935).

becomes

$$\chi^*_{rot}(\omega) = \frac{\chi_{s-rot}}{1 + j\omega\chi_{s-rot}\frac{\lambda}{\mu_o}} \tag{4.7}$$

Thus, depending upon the magnitude of the damping parameter, the initial susceptibility may exhibit either a resonance or a relaxation behavior.

In actual materials a sharp resonance is never observed, but this situation does not necessarily imply a large damping. It is more likely the result of a distribution of natural resonance frequencies ω_o. Such a distribution can readily arise because, in addition to the anisotropy torque acting on the magnetization vector, there are torques caused by the fields of neighboring domains or particles, by demagnetizing fields at voids and grain boundaries, and by magnetostriction. Such torques vary from point to point within a bulk sample, and thereby cause local variations in the resonant frequency.

Application of a field tends not only to reorient the magnetization vector within each domain, but also to rearrange the domain boundaries or walls. The motion of the walls may be reversible or irreversible depending upon the field strength. Only for sufficiently small fields is the motion and the resultant contribution to the permeability reversible. This behavior is in contrast to the rotational permeability which is ordinarily reversible at all field strengths.

To examine the nature of the wall displacement process we consider the simple model of a crystalline containing a single plane wall. For small displacements from equilibrium the dynamic behavior of the wall can be described by the equation of motion

$$2\mu_o M_s H = Rx + \beta \dot{x} \tag{4.8}$$

where x is the wall displacement measured from the equilibrium position x = o. The term on the left represents a pressure exerted on the wall by the applied field H; this pressure is opposed both by a restoring force Rx which tends to hold the wall to its position of static equilibrium and by a damping force $\beta \dot{x}$.

When H varies sinusoidally it is easy to show that the susceptibility due to wall displacement is

$$\chi^*_w = \frac{\chi_{s-w}}{1 + j\omega\tau'} \tag{4.9}$$

where

$$\chi_{s-w} = 4\mu_o M_s^2/RL \tag{4.9a}$$

is the static susceptibility, and

$$\tau' = \beta/R \tag{4.9b}$$

The complex susceptibility is therefore characterized by a relaxation spectrum. Doering[8] has pointed out that the moving wall has associated with it a kinetic energy term proportional to $\dot{x}^2$; thus, the wall may be regarded as having an effective mass. The inclusion of a mass term in Eq. 4.8 leads to a resonance behavior in χ_w^*. However, the mass term is extremely small and may ordinarily be disregarded.

The foregoing models are useful in interpreting the essential features of the permeability spectra observed for polycrystalline garnets. As they stand, however, they are too simple to fit the experimental facts in detail. However, in some cases, as we shall see they may be readily extended, in a semi-empirical way, to provide a close fit to the experimental data.

4.2 Initial Permeability of Polycrystalline Samples of YIG and LuIG

In slightly conductive samples of polycrystalline YIG and LuIG we have found permeability relaxation effects similar to those previously observed in a number of ferrimagnetic spinels[2,3]. The typical room-temperature spectrum (Fig. 4.1) exhibits two dispersive regions. * The lower-frequency branch occurs in the radio frequency portion of the spectrum, covers about two decades in frequency and accounts

---

[8] W. Doering, Z. Natur. 3a, 373 (1948).

* The data of Figs. 4.1 to 4.4 and of Fig. 4.7 were taken on samples fabricated at the Bell Telephone Laboratories, Murray Hill, N. J., and supplied to us through the courtesy of Dr. M. A. Gilleo. These samples were nominally stoichiometric; however, the fact that they were characterized by a d. c. resistivity about a decade lower than can be achieved suggests that they actually depart slightly from exact composition. Compositions made in our laboratory were not extensively checked with respect to permeability spectrum; to do so would have required the preparation of a variety of fairly large samples, e. g. disks and toroids with an o. d. 1" or larger. Most of our material preparation program was aimed at producing 3/8" disks for the anneal and hysteresis studies described in Chs. 5 and 6. However, based on a few spot checks of permeability and on a comparison of low temperature lag effects as observed in hysteresis loops, it appears that those samples (of composition x = 0) of ours which were in the same resistance range as BTL's were magnetically similar.

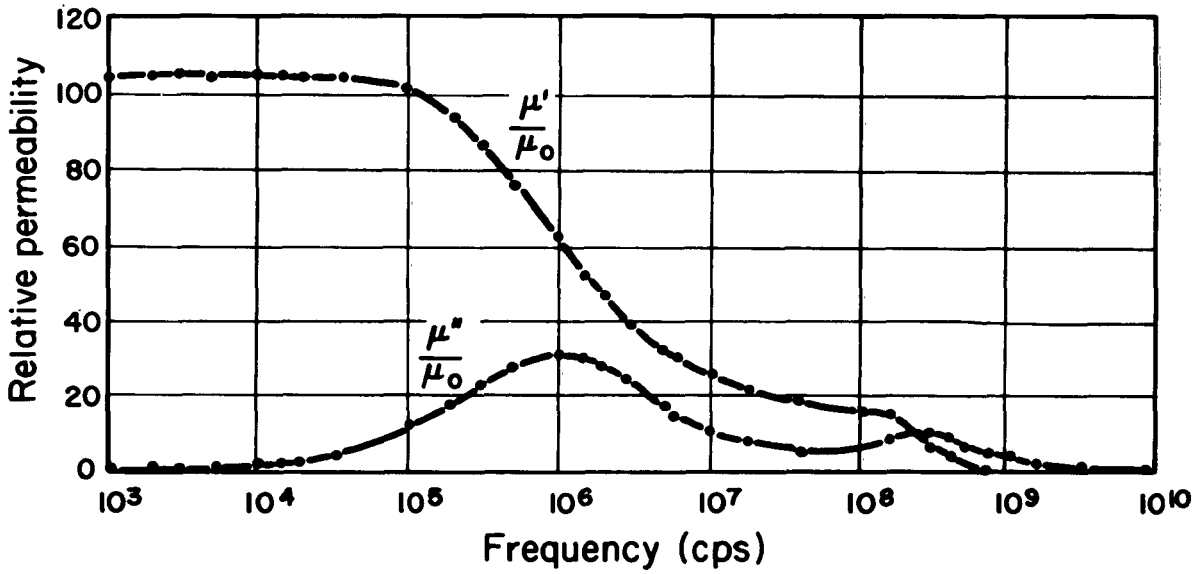

Fig. 4.1. Complex initial permeability spectrum of ceramic YIG at room temperature.

for about 80 percent of the static initial permeability. The higher frequency branch occurs in the microwave region and is less than a decade wide.

The latter we identify as a gyromagnetic resonance of the spin system in the effective anisotropy field. For a random distribution of crystallites, of cubic symmetry and with an easy axis along [111] we obtain from Eq. 4.4 that the resonance frequency (c.p.s.) should be

$$\nu_o = 2\gamma K / 3\pi M_s \qquad (4.10)$$

However, as already pointed out, in polycrystalline materials the torque on the spin system arises not only from the crystalline anisotropy but, in addition, there are torques exerted by demagnetizing fields created at domain walls, voids, and grain boundaries. Kriessman et al[9] have found that in a number of spinels for which K was known ($MgFe_2O_4$, $NiFe_2O_4$, Fe_3O_4) the values of ν_o predicted by Eq. 4.10, differed consistently from the experimental data by a constant factor. They, therefore, suggested that K in Eq. (4.10) should be replaced by an "effective" anisotropy constant K_e, which for spinels was empirically found to equal 2K. Making this adjustment we find ν_o = 330 Mc. a result in good agreement with the experimental value, 300 Mc.

The low-frequency branch of the dispersion shows a strong temperature dependence (Figs. 4.2, 4.3.) The point at which the magnetic loss is a maximum ν_m, exhibits a temperature activated shift to lower frequency with decreasing temperature, governed by the relation (Fig. 4.4)

$$\nu_m = \nu_o \exp(-U/kT) \qquad (4.11)$$

where ν_o is a constant. The activation energy U for the process is 0.38 ev.

In LuIG we have investigated only the low frequency branch of the spectrum (Figs. 4.5, 4.6, and 4.7.) The behavior is quite similar to that found in YIG samples.

4.3 Comparison with Spinel Spectra

The permeability spectra described above find a close counterpart in the temperature-activated domain-wall relaxation observed in slightly reduced spinels[2,3].

The origin of relaxation in the spinels is well accounted for by the folloiwng mechanism. When divalent iron is present in the spinel lattice, there tends to be an ordering of divalent and trivalent iron which is preferential with respect to the magnetic axis. Any alteration of the spin directions, and specifically, the reorientation

---

[9] C. J. Kriessman, S. E. Harrison and H. S. Belson, J. Appl. Phys. 29, 452 (1958).

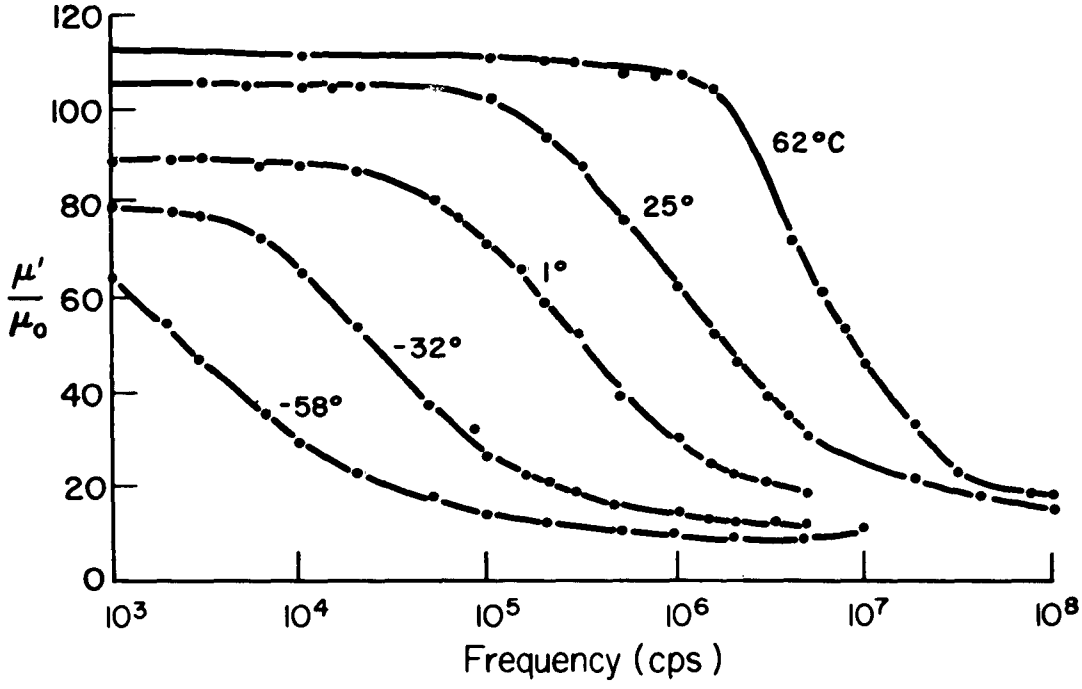

Fig. 4. 2. Permeability spectra of polycrystalline YIG at several temperatures.

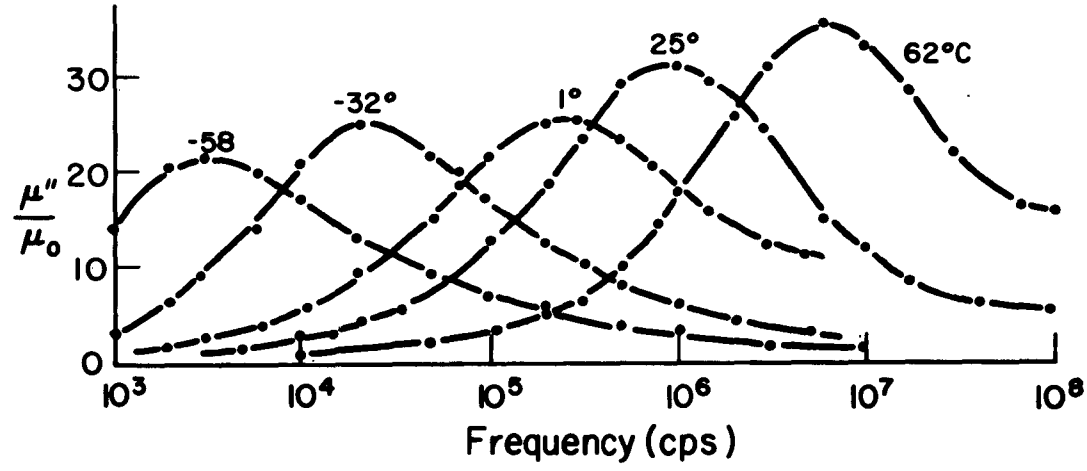

Fig. 4. 3. Magnetic-loss spectra of polycrystalline YIG at several temperatures.

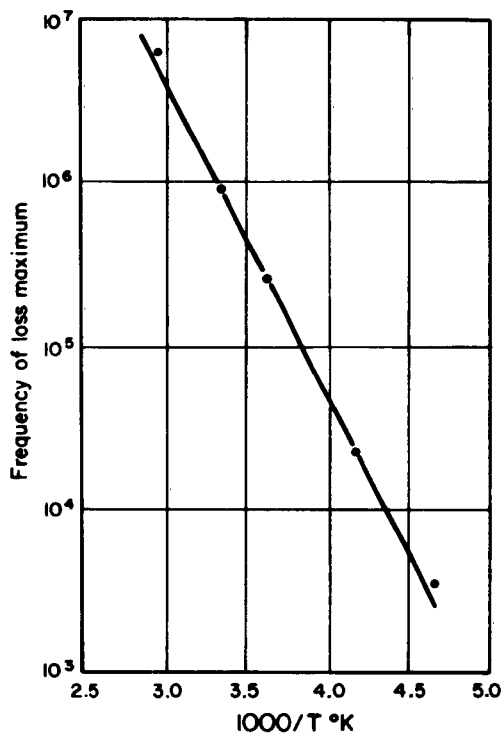

Fig. 4.4. Frequency of magnetic loss maximum as a function of reciprocal temperature (YIG).

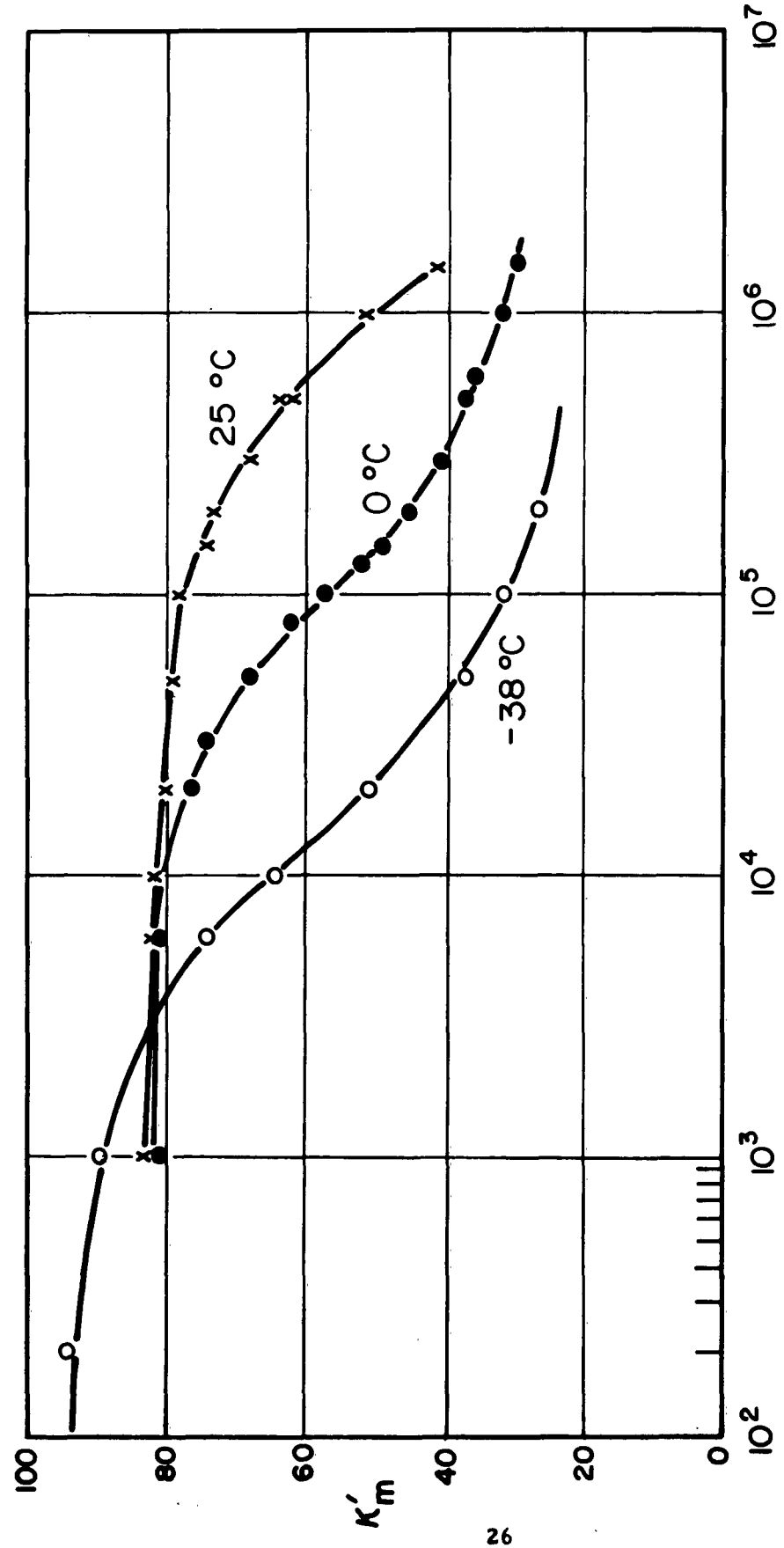

Fig. 4.5. Permeability spectra of LuIG at various temperatures.

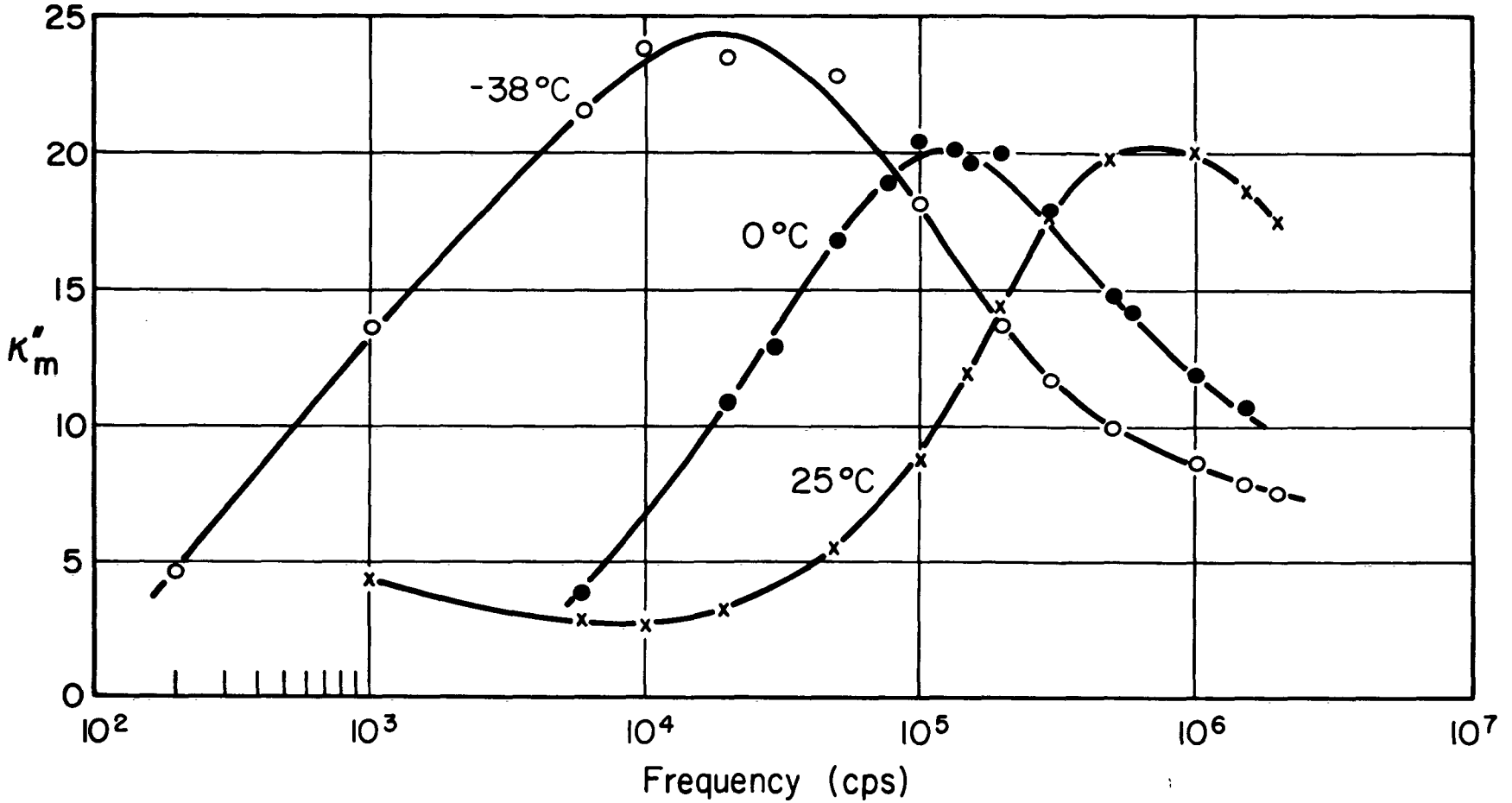

Fig. 4.6. Magnetic loss spectra for LuIG at various temperatures.

that occurs within a moving domain wall, forces a redistribution of the cation ordering. Since the cations involved are Fe^{3+} and Fe^{2+}, the reordering can be effected by electron transfer from Fe^{2+} to Fe^{3+}. The energy dissipated in this process is taken into account as a damping term in the equations of motion for the wall. Because the electron transfer is temperature activated, the wall damping behaves similarly. A major point in support of this model is found in the fact that the activation energy for the wall damping corresponds to that for electric conduction. (See Table III.)

Table III

Comparison Between Activation Energies for Magnetic Loss and for Resistivity

Composition		Activation Energy	
Nominal	Actual	from resistivity	from magnetic loss
$NiFe_2O_4$	$Ni_{1.0}Fe^{2+}_{0.07}Fe^{3+}_{1.86}O_4$	0.14 e.v.	0.17 e.v.
$Ni_{0.8}Zn_{0.2}Fe_2O_4$	$Ni_{0.8}Zn_{0.2}Fe^{2+}_{0.04}Fe^{3+}_{1.91}O_4$	0.14	0.12
$Ni_{0.3}Zn_{0.7}Fe_2O_4$	$Ni_{0.315}Zn_{0.685}Fe^{2+}_{0.03}Fe^{3+}_{2.02}O_4$	0.14	0.13

We believe that this same mechanism is responsible for the temperature-activated lag found in our samples of YIG; In view of the high d-c resistivity of these specimens ($\approx 10^9$-10^{10} ohm-cm at 100°C), one might at first be inclined to argue that any divalent iron present is much too small to make the proposed mechanism effective. However, measurements of resistivity in these polycrystalline garnets must be examined more carefully. We find that when a-c measurements are made, there is a pronounced dispersion in the a-c resistivity. For example, the measurements at 25°C show a monotonic decrease of resistivity with frequency up to about 10^5 cps, where a plateau at 3×10^4 ohm-cm is reached (Fig. 4.8.) It would appear that the high d-c resistivity is due to grain-boundary effects and that the resistivity at the plateau is more representative of the bulk material. The activation energy for the d-c resistivity is 0.66 ev; for the a-c resistivity, measured at the r-f plateau, we find a considerably lower activation energy, 0.31 ev. The latter value is more nearly comparable with the value 0.38 ev obtained in our magnetic-loss measurements.

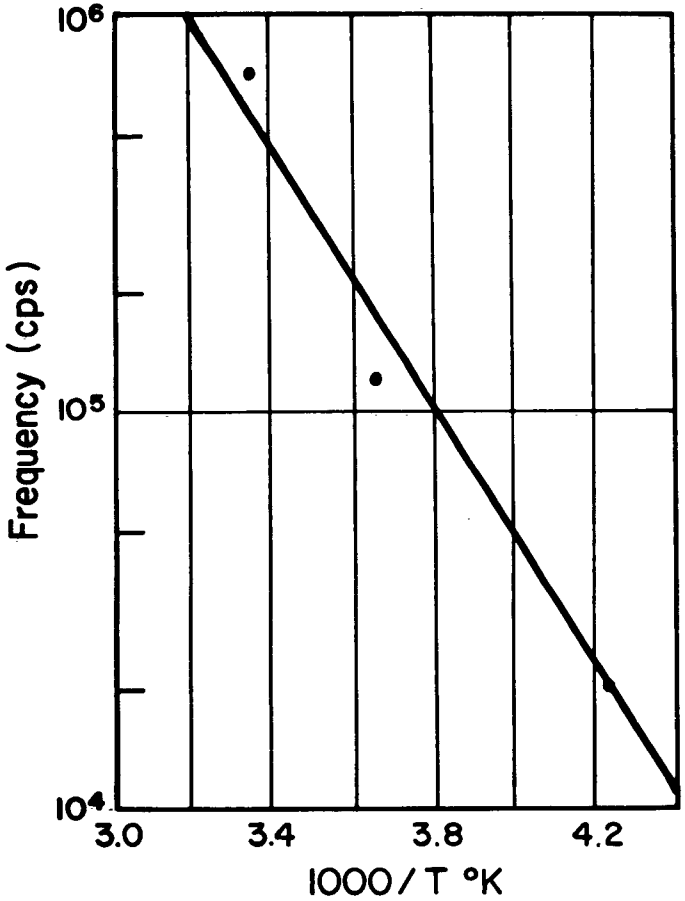

Fig. 4.7. Frequency of magnetic loss maximum for LuIG as a function of temperature. Activation energy is 0.3 ev.

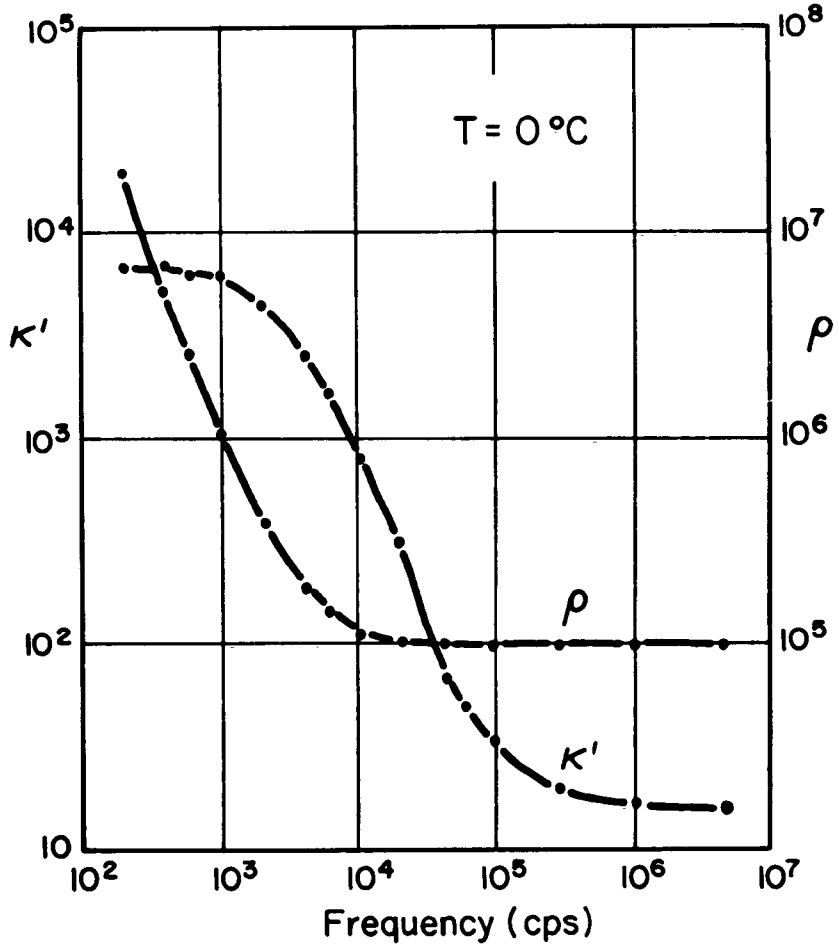

Fig. 4.8. Dielectric constant and a-c resistivity of YIG.

It should be pointed out that the very fact that the activation energy for the magnetic process is relatively low suggests an electronic rather than an ionic activation process.

We have examined, to a limited extent, a number of polycrystalline garnets of high density (order of 99 percent of theoretical) and higher resistivity than the aforementioned samples (resistivity 10^9 ohm-cm at 10^5 cps.) In these samples * there was no evidence of a magnetic relaxation, a result which also bears out the idea that the damping is electronic in origin.

In contrast with the spinels, the stoichiometric garnet phase does not contain divalent iron. The presence of any Fe^{2+} would occur only in a non-stoichiometric composition which would, presumably, contain oxygen vacancies. The existence of a defect structure has been suggested by Gibbons and Chirba[10] who have found a stress-induced relaxation in the Young's modulus of YIG which they attribute to electron migration.

4.4 Analysis of the Data

The damping force produced on a moving domain wall by magnetically induced electron transfer from Fe^{2+} to Fe^{3+} has been calculated by Galt[11] and Clogston,[12] the starting point for their work being a model proposed by Néel to explain relaxation effects in carbonyl iron. Clogston finds the wall velocity to be related to the driving field by

$$v = \frac{6.8\mu_0 M_s d}{\left(\frac{Na^2}{kT}\right)\tau} H \qquad (4.12)$$

where d is the wall thickness parameter N is the concentration of Fe^{2+}, "a" is the energy of (magnetically induced) ordering (per electron) and τ is a relaxation time constant which may be expressed as

$$\tau = \tau_\infty e^{A/kT} \qquad (4.13)$$

---

* These YIG garnets were obtained from Lincoln Laboratory.

[10] D. F. Gibbons and V. C. Chirba, Phys. Rev. 110, 770 (1958).

[11] J. K. Galt, Bell System Tech. J. 33, 1023 (1954).

[12] A. M. Clogston, Bell System Tech. J. 34, 739 (1955).

with τ_∞ a constant and A the activation barrier which must be overcome by an electron jumping from Fe^{2+} to Fe^{3+}.

For a 180^o wall unrestrained by a restoring force Eq. 4.8 reduces to

$$\beta \dot{x} = \beta v = 2\mu_o M_s H \tag{4.14}$$

which result, compared with Eq. 4.12, yields

$$\beta = \left(\frac{1}{3.4d}\right)\left(\frac{Na^2}{kT}\right)\tau \tag{4.15}$$

We have shown that for a 180^o wall, driven sinusoidally, the susceptibility has a relaxation time constant $\tau' = \beta/R$ given by Eq. 4.9b. For β we take the value given by Eq. 4.15, and we obtain for the wall-relaxation time constant

$$\tau' = \frac{1}{3.4d}\left(\frac{Na^2}{kT}\right)\frac{\tau}{R} = \frac{1}{3.4d}\left(\frac{Na^2}{kT}\right)\frac{\tau_\infty}{R}\, e^{A/kT} \tag{4.16}$$

Because the static susceptibility arising from the wall motion is given by

$$\chi_{s-w} = \frac{4\mu_o M_s^2}{LR} \tag{4.9a}$$

we can eliminate R from Eq. 4.16 obtaining

$$\tau' = \frac{\chi_{s-w} L}{13.6\ \mu_o M_s^2}\left(\frac{Na^2}{kT}\right)\tau_\infty\, e^{A/kT} \tag{4.17a}$$

$$= \tau'_\infty e^{A/kT} \tag{4.17b}$$

Quantitatively this result is not too useful because it contains a number of constants we are unable to evaluate, e.g. a, L. It does, however, demonstrate two important qualitative features of the wall relaxation process:

a) τ' is proportional to the concentration of divalent iron, and

b) is governed by the activation energy for electron transfer from Fe^{2+} to Fe^{3+}.

Because this electron transfer process must also be responsible for conduction in these oxides the activation energies for magnetic relaxation and for conduction should correspond, as we have found.

The equation of motion (Eq. 4.8) that we have used in describing the harmonic behavior of a plane wall enables us to compute the contribution to the total susceptibility made by one individual domain in a complex aggregate. To find the susceptibility of the assemblage we must sum over all the domains in a unit volume. The effect of such averaging may be reasonably represented as a relaxation process which is

governed by a distribution of relaxation time constants rather than by a single time constant. Thus, we have

$$\chi_w^*(\omega) = \chi_{s-w} \int_0^\infty \frac{f(\tau')d\tau'}{1 + j\omega\tau'} \tag{4.18}$$

where $f(\tau')$ is a weighting function giving the fractional contribution to the susceptibility of domain walls having a relaxation time constant between τ' and $\tau' + d\tau'$. It follows that

$$\int_0^\infty f(\tau')d\tau' = 1 \tag{4.19}$$

The total susceptibility of the system is given by

$$\chi^*_{(\omega)} = \chi^*_w(\omega) + \chi_\infty \tag{4.20}$$

where χ_∞ denotes the contribution to the susceptibility arising from rotational processes. Here we assume that the critical relaxation time constants for the rotational processes are short compared to those for wall displacement, so that in the frequency range in which the walls are undergoing relaxation the rotational susceptibility remains essentially constant.

Combining Eq. 4.20 with Eq. 4.18 we obtain as the expression for the permeability spectrum

$$\mu^* = \mu_\infty + (\mu_s - \mu_\infty) \int \frac{f(\tau')\, d\tau'}{1 + j\omega\tau'} \tag{4.21}$$

where

$$\frac{\mu_\infty}{\mu_o} = 1 + \chi_\infty \tag{4.21a}$$

and

$$\frac{\mu_s}{\mu_o} = 1 + \chi_\infty + \chi_{s-w} \tag{4.21b}$$

For $f(\tau')$ a unit impulse function, Eq. 4.21 reduces to the simple form

$$\mu^* = \mu_\infty + \frac{\mu_s - \mu_\infty}{1 + j\omega\tau'} \tag{4.22}$$

It is well known that a plot of this function in the μ^* plane leads to a semicircular

locus (Fig. 4.9a.) Each point on the locus corresponds to a particular frequency, and as we increase frequency we traverse the arc in a counterclockwise direction.

In the magnetic materials we have studied the locus has the form of a segment of a circle with its center depressed below the real axis (Fig. 4.9b.) Cole and Cole[31] have demonstrated that such a locus can be interpreted in terms of a distribution of relaxation time-constants

$$g(z) = \frac{1}{2\pi} \frac{\sin \alpha\pi}{\cosh (1-\alpha)z - \cos \alpha\pi} \qquad (4.23)$$

where $z = \ell n (\tau'/\tau'_m)$, τ'_m being the logarithmic mean time constant of the distribution and where α is an empirical parameter determined from the locus as shown in Fig. 4.9b.

For the Cole-Cole data plots shown in Fig. 4.10 we may take as a representative angle $\alpha\pi/2 = 18^\circ$. The distribution determined by this angle has a 5:1 range of time constants, measured between half amplitude points on g(z.) This range is considerably smaller than found in spinels where typical values of $\alpha\pi/2$ are nearer 40° and the corresponding range of time constants is the order of 80:1.

From the Cole-Cole plots we are able to estimate the contributions to the initial permeability arising from wall and rotational processes. For YIG at room temperature, we conclude that of the total permeability ($105\mu_o$), 80 percent is due to wall motion, the remainder to rotation.

4.5 Permeability as a Function of Temperature

The relaxation time constants appearing in Eq. 4.21 are temperature activated and, in consequence, the permeability measured as a function of temperature at fixed frequency will show a relaxation effect.

In Fig. 4.11 the upper curve is a plot of the 1 KC permeability * obtained on a sample of YIG which was demagnetized at room temperature, cooled in zero field to liquid N_2, and measured on slow warming. The change in permeability between room temperature and -40°C represents the typical drop-off resulting from an increase in anisotropy constant with decreasing temperature. Below -40°C there occurs a

---

* The data shown is actually a plot of μ^* vs. T.

[31] K. S. Cole and R. H. Cole, J. Chem. Phys. 9, 341 (1941).

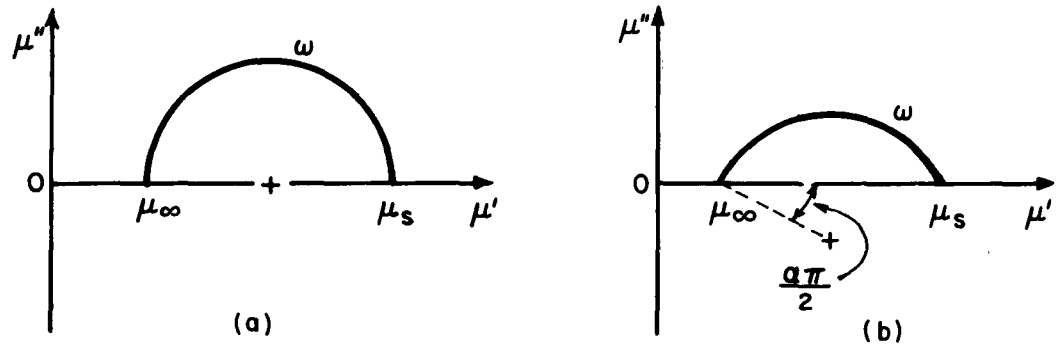

Fig. 4.9. Cole-Cole plots: (a) single relaxation time constant; (b) distribution of relaxation times.

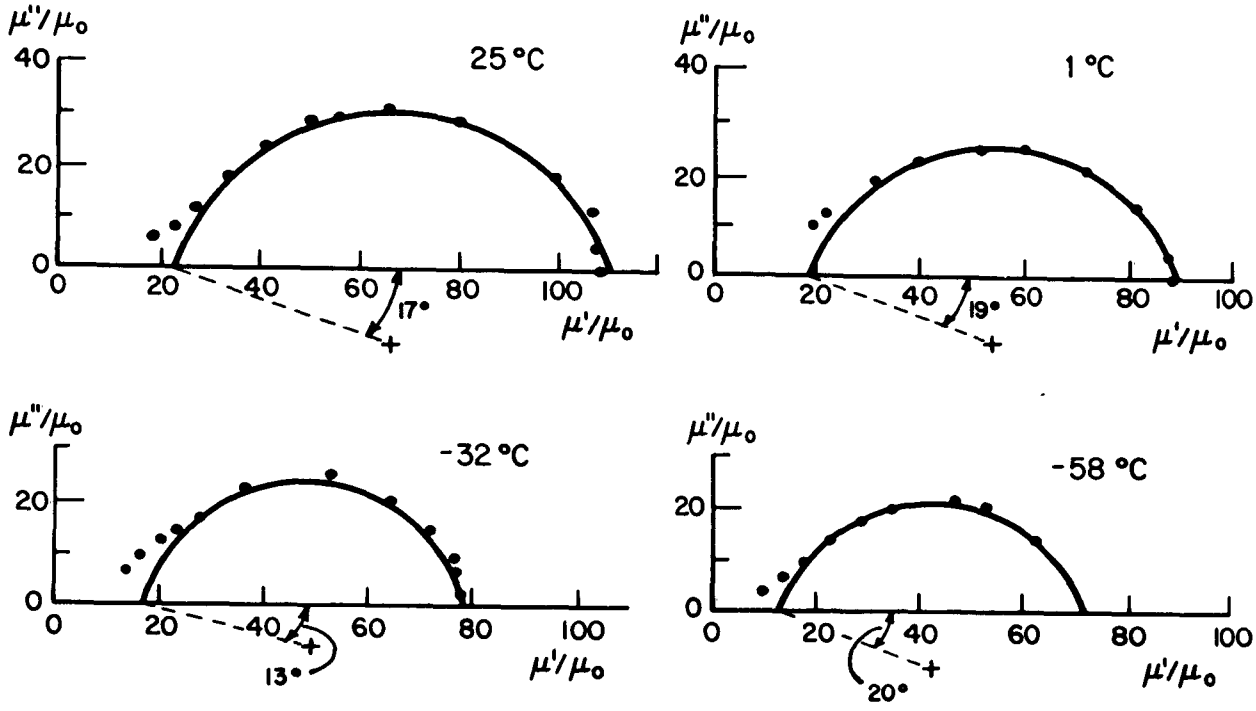

Fig. 4.10. Cole-Cole plots for polycrystalline YIG at several temperatures.

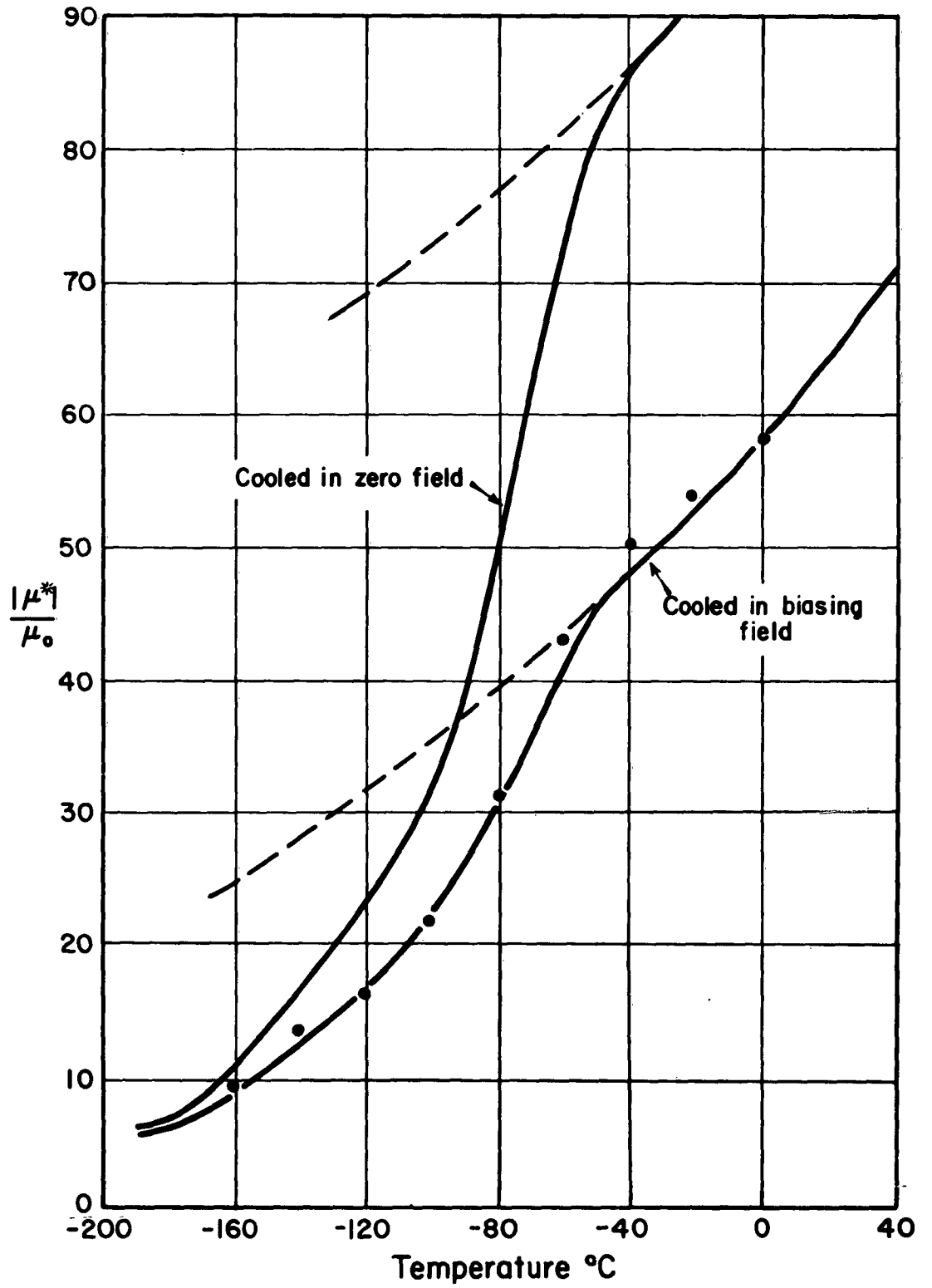

Fig. 4.11. Permeability of ceramic YIG at 1 kc as a function of temperature. Curves are experimental; points are calculated from Eq. 4.24.

precipitous fall in permeability resulting from the relaxation in domain-wall motion.

The lower curve in Fig. 4.11 was obtained on the same sample during a warming run but after the sample was cooled to nitrogen temperature in a 60 cps magnetizing field of peak intensity ca 165 oersteds. When so cooled, this particular sample had a frozen-in remanence even after the 60-cps field was reduced slowly to zero. In the remanent state the initial permeability is typically lower than in the demagnetized state. The interesting feature of the results is the fact that the two curves are quite similar. Indeed, by a simple scaling the curves can be brought into essential coincidence. The points shown on the lower curve were calculated by such a scaling procedure from the empirical formula

$$\mu_2 = (\mu_1 - \mu_\infty)\ \alpha + \mu_\infty \tag{4.24}$$

where μ_1 is the permeability measured on the upper curve, μ_2 the scaled permeability (the value plotted as a point in Fig. 4.11) and α, the scaling factor, was chosen to be 0.48. For the rotational permeability μ_∞ we have assumed a temperature dependence that is linear in the interval 0°C to -200°C, that is,

$$\mu_\infty = 5\mu_o + (T + 200)\ \left(\frac{15}{200}\right)\ \mu_o\ ;\ T \text{ in } {}^\circ C \tag{4.25}$$

We conclude that the two curves in Fig. 4.11 differ only in that the lower curve represents a remanent state in which ca 50 percent of the total wall-motion contribution has been lost.

4.6 Permeability in the Series $(3 + x)Y_2O_3 \cdot (5 - x)Fe_2O_3$

As anticipated, the occurrence of precipitates in compositions with $x \neq 0$ leads to a progressive reduction in initial permeability with increasing magnitude of x (Figs. 4.12, 1.13.)

The compositions $x = -0.3, -0.4$ are particularly noteworthy in that they have a permeability essentially independent of temperature over a wide temperature range. This feature can be of considerable technical importance for the design of communication cores where requirements frequently demand that the permeability be highly stable with respect to environmental changes. We have not had the time in our program to carry out the detailed evaluation needed to determine whether we have in these garnets a material comparable in stability to the powdered iron cores now employed in communication work. Our preliminary results, however, indicate that such an evaluation is indeed called for.

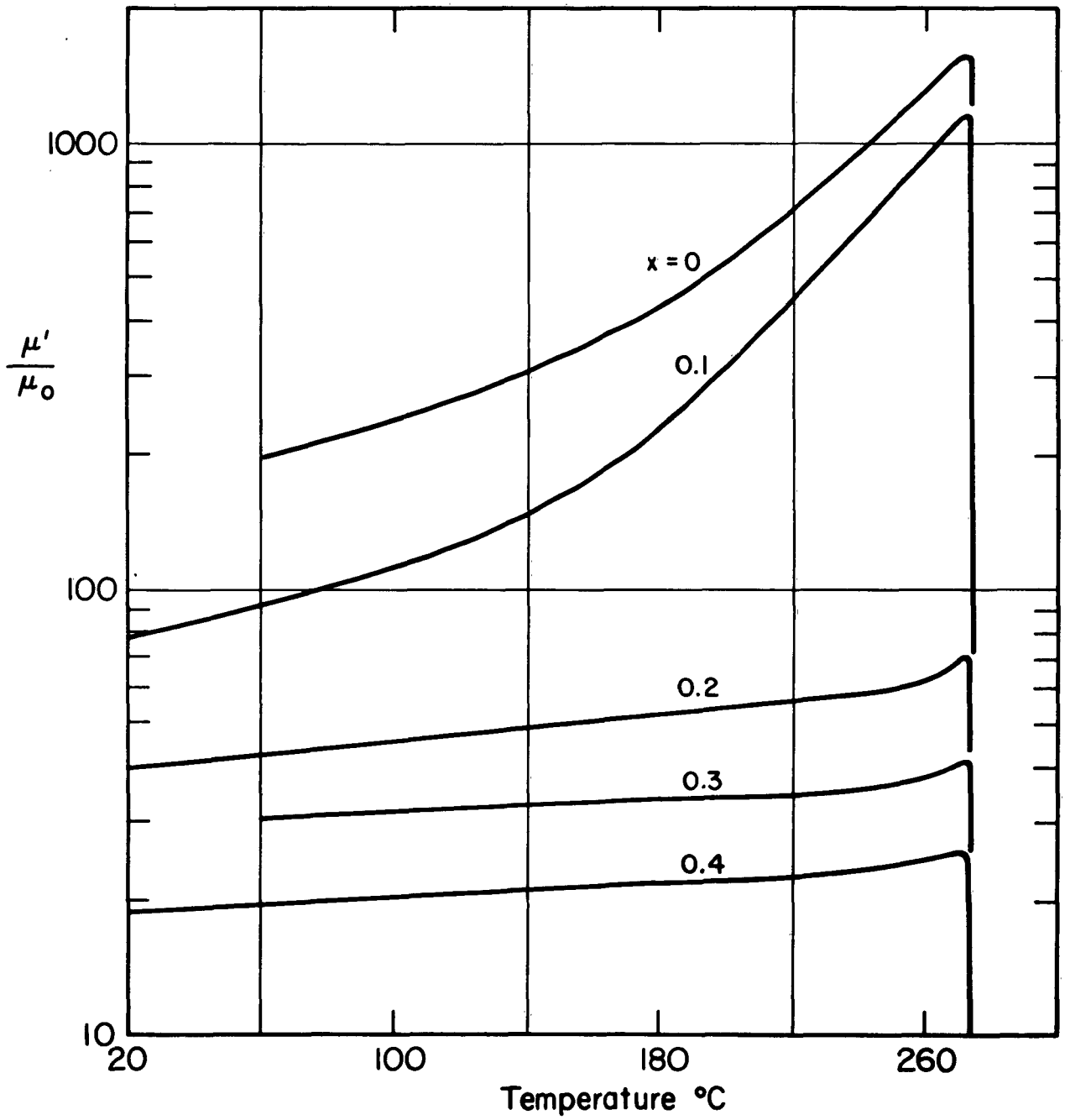

Fig. 4.12. Initial permeability vs. temperature at 1 kc for series $(3+x)Y_2O_3 \cdot (5-x)Fe_2O_3$; $x \geq 0$.

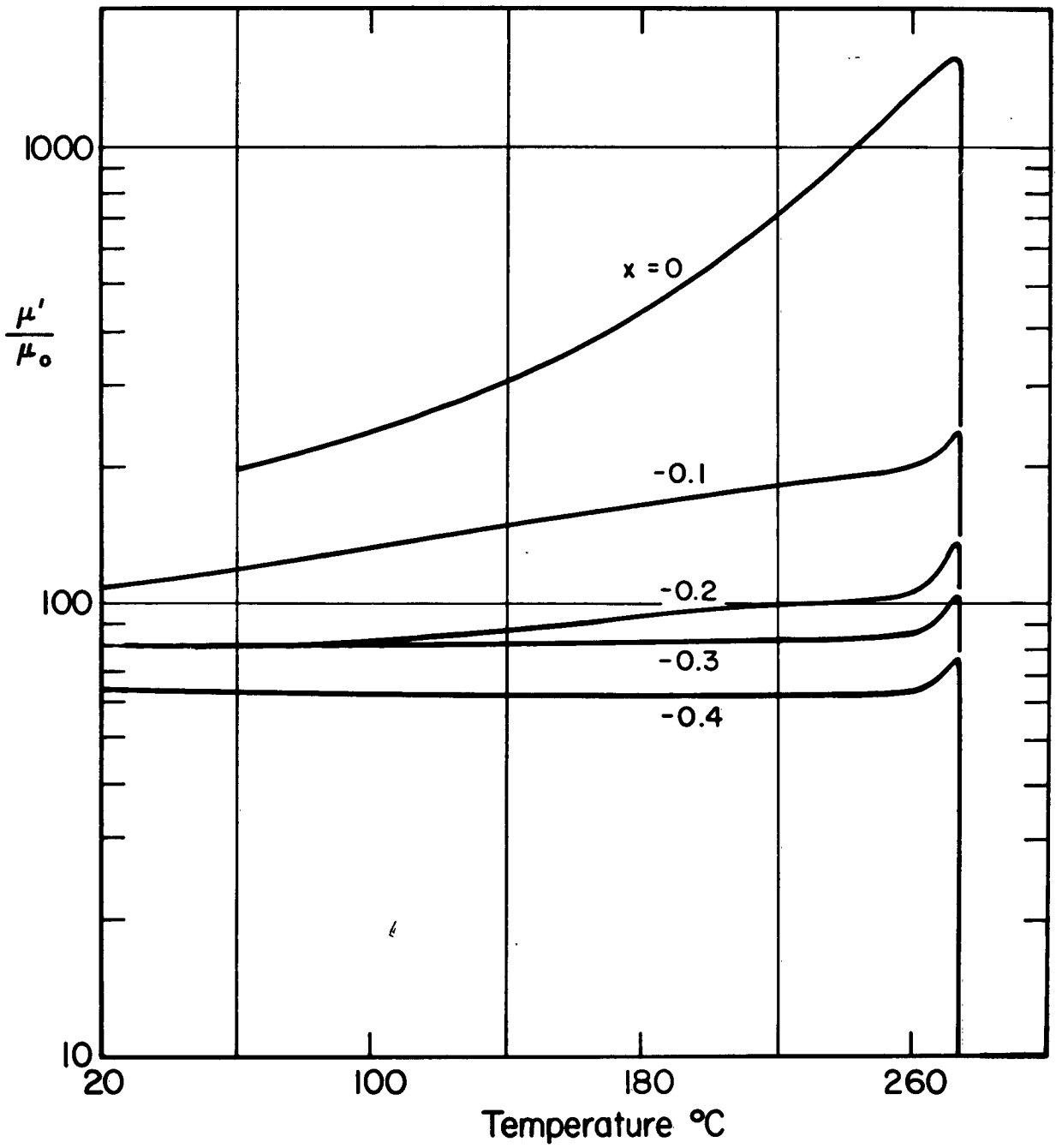

Fig. 4.13. Initial permeability vs, temperature at 1 kc for series $(3 + x)Y_2O_3 \cdot (5 - x)Fe_2O_3$; $x \leq 0$.

5. MAGNETIC ANNEAL

In polycrystalline garnets which show a temperature-activated relaxation in the permeability, we find pronounced magnetic anneal effects.

In a typical experiment the following procedure was employed: A ceramic garnet disk was attached to the shaft of a recording torque magnetometer * and a room-temperature curve was traced to ensure that any torques caused by shape anisotropy were negligible. The sample was then cooled to 78°K in a field of 6 kgauss and allowed to "soak" at low temperature for a short period (5-10 min.) With the sample held fixed in angular position, the field-producing electromagnet was rotated at approximately uniform speed through 360° and the torque exerted on the sample was automatically recorded as a function of angle, a complete trace taking about 20 sec.; curve 1 in Fig. 5.1 was obtained in this way. After completing this trace the magnet was repositioned at zero and the sample was allowed to "soak" in the 6-kguass field for an additional 10 min. The magnet was rotated quickly to the position of maximum torque (45°) and the torque variation was recorded as a function of time. As shown in Fig. 5.2, the torque was observed to relax according to an exponential law from a peak value at t = 0. For the particular LuIG sample described by Figs. 5.1, 5.2, the peak torque corresponded to a uniaxial anisotropy energy of 4500 erg/cc, and the relaxation time constant was very nearly 15 sec. If, with the magnet held at the 45° position, we allowed the usual soaking time, and then proceeded to take a torque trace, we obtained curve 2 of Fig. 5.1. Note that this curve has its zero crossings intermediate between 0° and 45°.

The preceding results may be interpreted in the following way. Upon cooling in a field, the polycrystalline disk develops a unique magnetic anneal axis coincident with the applied field. This axis can be shifted in direction at low temperature by a reanneal; that is, by altering the orientation of the field. The preferred axis tends to shift from its initial position to the new direction with a relaxation-time constant. However, the shift is not complete because the disk "remembers" the axis of initial cooling. The over-all behavior is consistent with an expression for anisotropy energy made up of the sum of two terms, each having uniaxial character:

$$U = \left[K_o + K_1 f(t)\right] \sin^2\Theta + K_1 \left[1 - f(t)\right] \sin^2(\Theta - \alpha), \qquad (5.1)$$

---

* The instrument employed is described in Sec. 10.2.

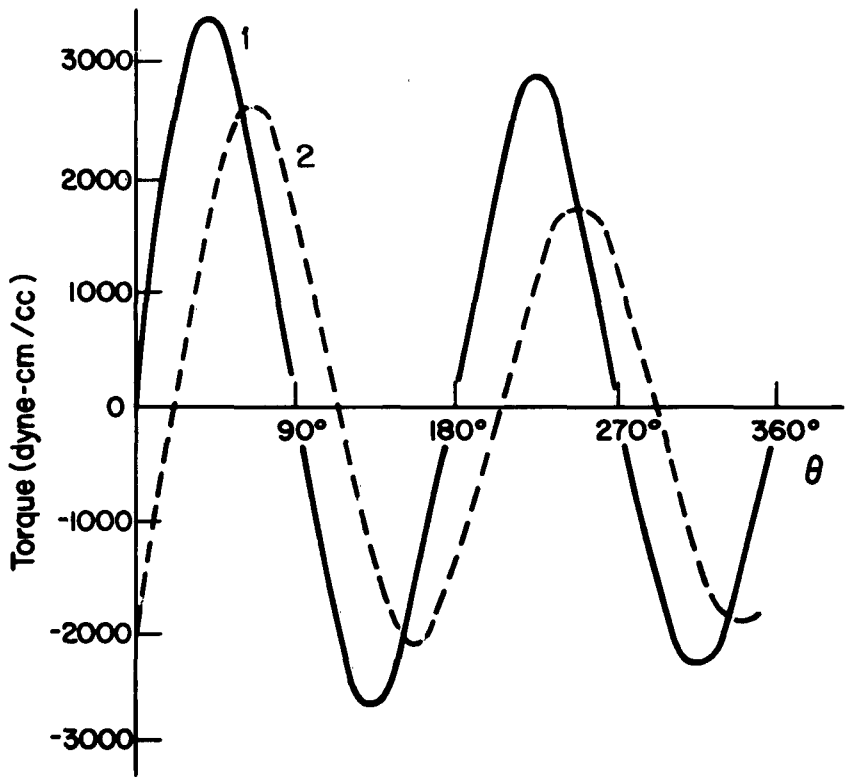

Fig. 5.1. Torque curves for LuIG ceramic at -196°C. Curve 1 is for disk cooled in a field from room temperature; curve 2 is obtained after reanneal at -196°C in a direction $\theta = 45^{\circ}$.

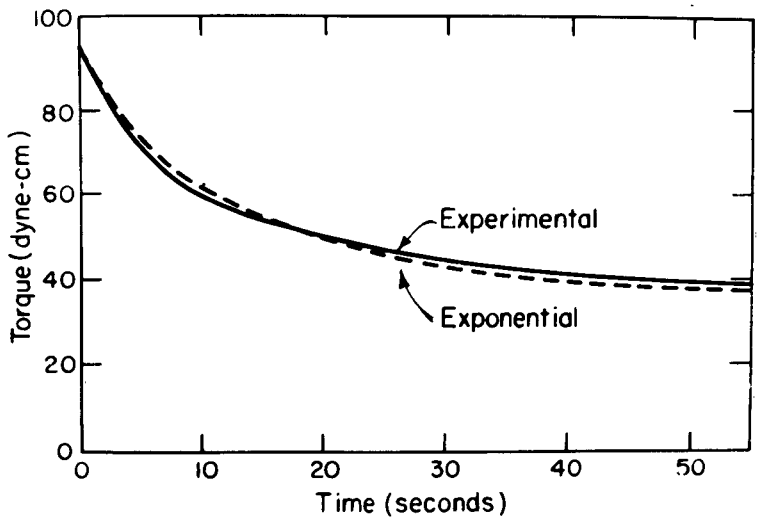

Fig. 5.2 - Relaxation of field-induced anisotropy in ceramic LuIG

where Θ is the angle measured from the field direction applied during initial cooling; α is the angle between the initial axis and the direction of reanneal. The constant K_o represents that component of the anisotropy energy which is "remembered" after cooling, while K_1 is the component of anisotropy that can be shifted by redirecting the applied magnetic field. The time function has the range zero to unity, its precise functional form being dependent upon the conditions of the experiment. If, for example, after the sample has been cooled in a field and "soaked", the field direction is suddenly shifted from $\Theta = O$ to $\Theta = \alpha$, f(t) will initially be unity and decay exponentially to zero.

The fact that in our experiments on lutetium iron garnet the relaxation time for reorientation of the anneal axis was comparable to the time required to take a torque tracing, accounts for the decay in torque amplitude as we proceed from left to right in Fig. 5.1.

The mechanism of an electronic ordering correlated with the axis of spontaneous magnetization has been put forth in the preceding section to account for the permeability relaxation. The same mechanism will account for the magnetic anneal. We suggest that at sufficiently low temperatures, where the time constant for diffusion is extremely long, the ordered electron arrangement becomes "frozen-in" relative to the spin axis. Thus, when a polycrystalline material of this type is cooled in a field, the common axis of directional ordering, and the polycyrstalline aggregate, which was initially magnetically isotropic, acquires a uniaxial magnetic character.

6. SCUARE LOOP BEHAVIOR

6.1 Experimental Results

In those garnets which exhibit permeability relaxation and magnetic anneal effects we find striking anomalies in the behavior of the hysteresis loop. As the temperature is lowered, the sixty-cycle hysteresis loop, normal at room temperature, at first grows considerably wider, a typical result for many materials. For still lower temperatures instabilities appear and the loop develops nearly perfectly vertical sides. This sequence of changes is shown in Fig. 6.1 for a lutetium iron garnet sample, in Figs. 6.2 and 6.3 for a YIG specimen.

Data of this kind has been reported previously[13], but the real significance

---

[13] B. A. Calhoun, J. Appl. Phys., Supplement to Vol. 30, No. 4, 293S (1959).

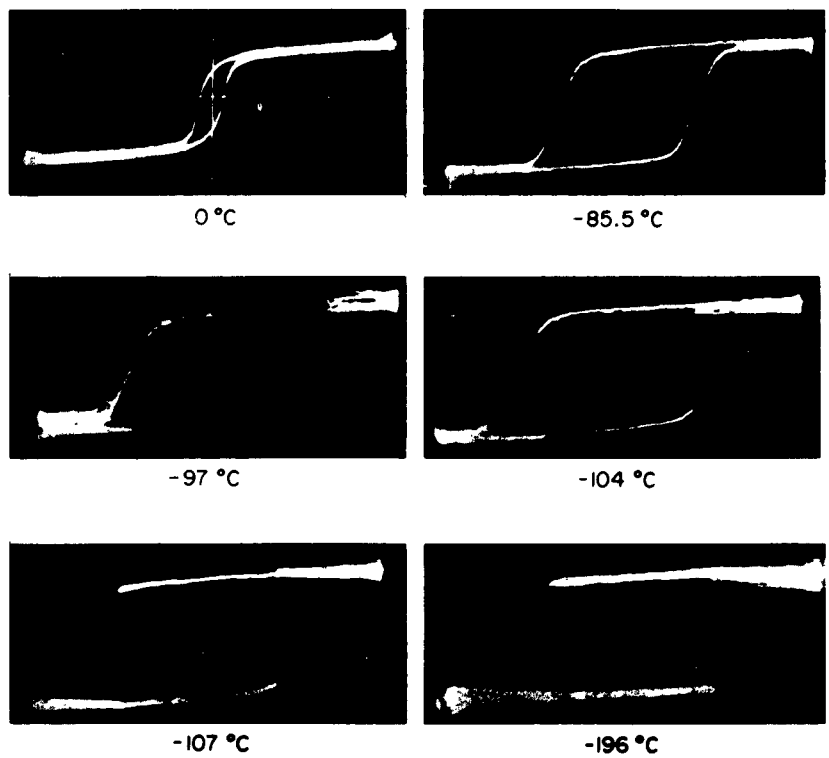

Fig. 6.1. Hysteresis loops for polycrystalline LuIG at 60 cps.

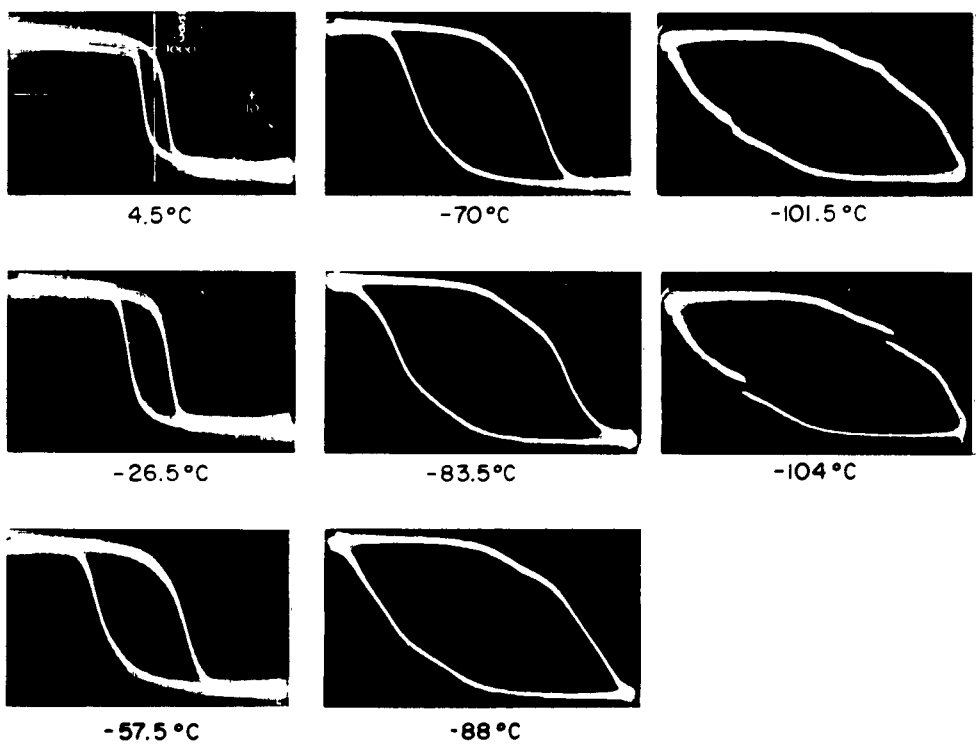

Fig. 6.2. Hysteresis loops for YIG at 60 cps.

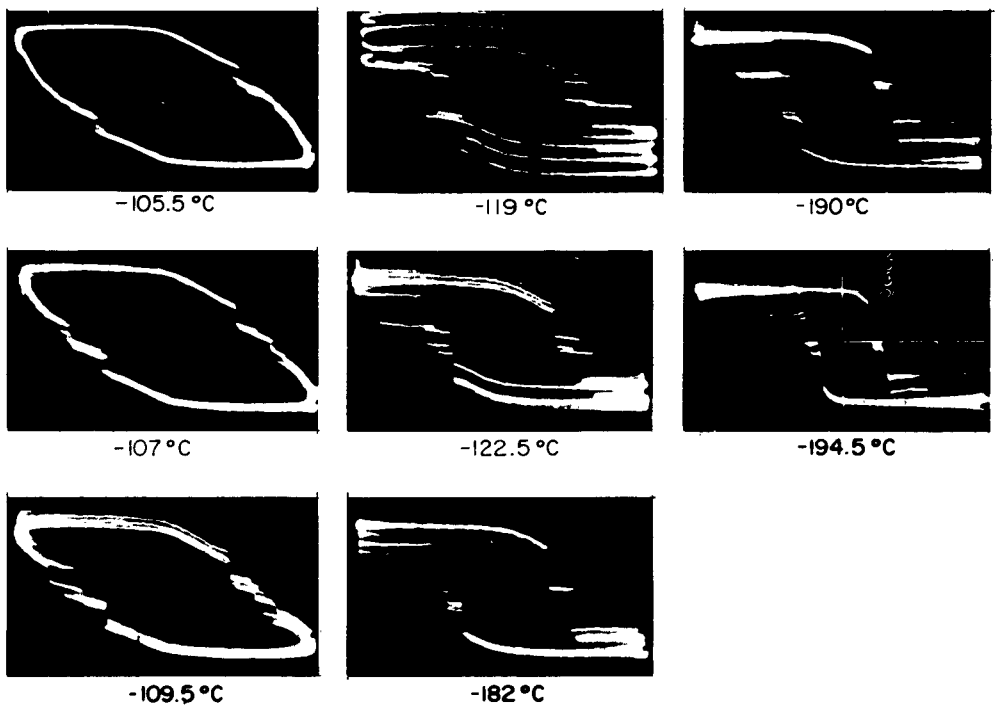

Fig. 6.3. Hysteresis loops for YIG at 60 cps.

of the square loop behavior has not been recognized. We find that these materials are not square loop in the usual sense, i.e. squareness does not occur when a quasistatic loop is taken but develops only above a critical frequency of excitation. This type of behavior, which we shall call "dynamic squareness," is illustrated by the sequence of loops shown in Fig. 6.4 for a representative, core excited, at 78°K, by a periodic triangular waveform of current at several different frequencies. At an excitation frequency of 0.26 cps the loop appears quite normal. However, as we increase the frequency irregularities appear. In (b), for example, one cycle is normal, another abnormal; a similar effect appears in (c). In (d), square loop behavior is well established. *

Detailed studies of loop behavior made with triangular wave current excitation reveal that, at fixed temperature, instability will occur for values of peak excitation H_p (Fig. 6.5) which exceed a critical value $H_{p\ crit}$ and for values of frequency which in excess of f_{crit}, these two threshold quantities having the inter-relation

$$H_{p\ crit} = \frac{c}{f_{crit}} \tag{6.1}$$

where c is a constant of proportionality. This relation implies that dynamic squareness, in fact, occurs when the slope of the triangular wave

$$\alpha = \frac{H_p}{\frac{\tau}{4}} = 4H_p f \tag{6.2}$$

exceeds a critical value α_{crit}. Under these circumstances we will have

$$H_p \geq \alpha_{crit} / 4f \tag{6.4a}$$

$$f \geq \alpha_{crit} / 4H_p \tag{6.4b}$$

Below the critical frequency, the loop shows no anomalies in shape, but the coercive force exhibits pronounced frequency dependence (Figs. 6.6 and 6.7.)

Measurements on samples initially in the demagnetized state reveals that some prior exposure to a magnetic field is required before dynamic squareness will

---

* The ringing effect observed in Fig. 6.4 is not a property of the core but is due to a natural resonance in the integrating circuit used. The resonance is excited by the voltage impulse generated at the instant the core switches.

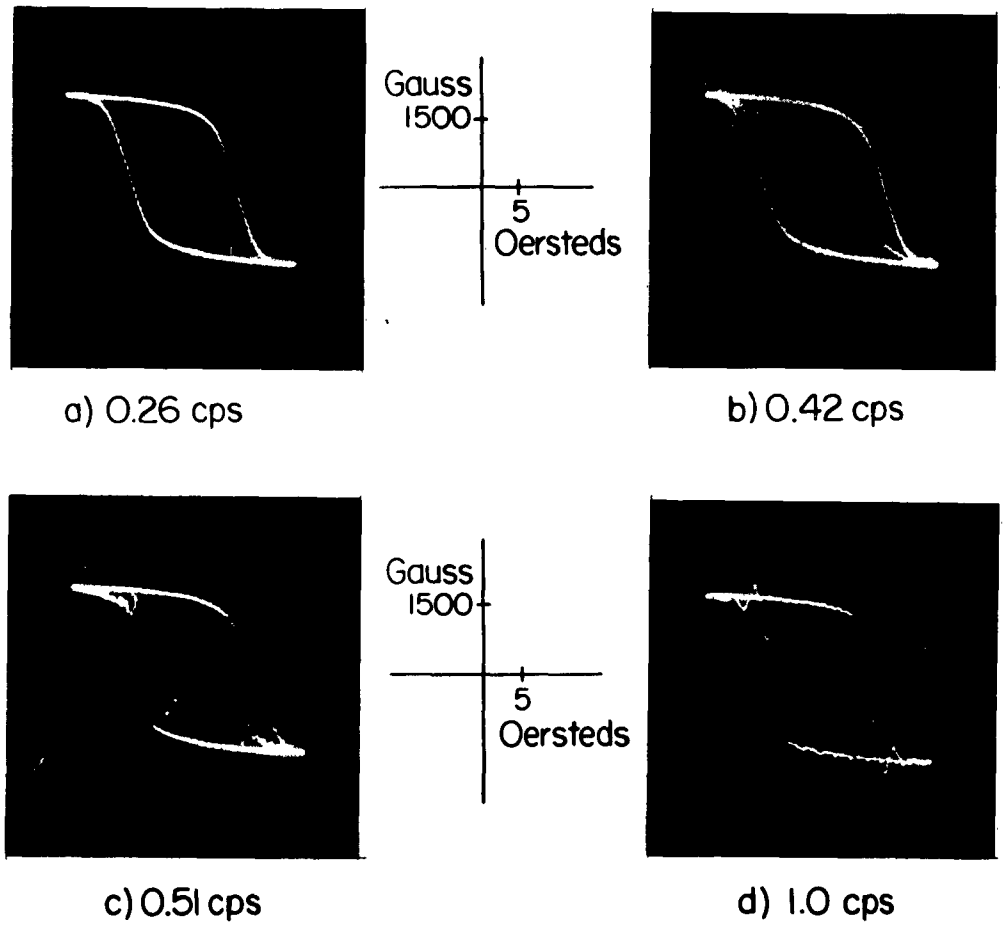

Fig. 6.4. Hysteresis loops of YIG at 77°K. The ringing effect in (b), (c), and (d) is due to galvanometer resonance in the flux indicating circuit.

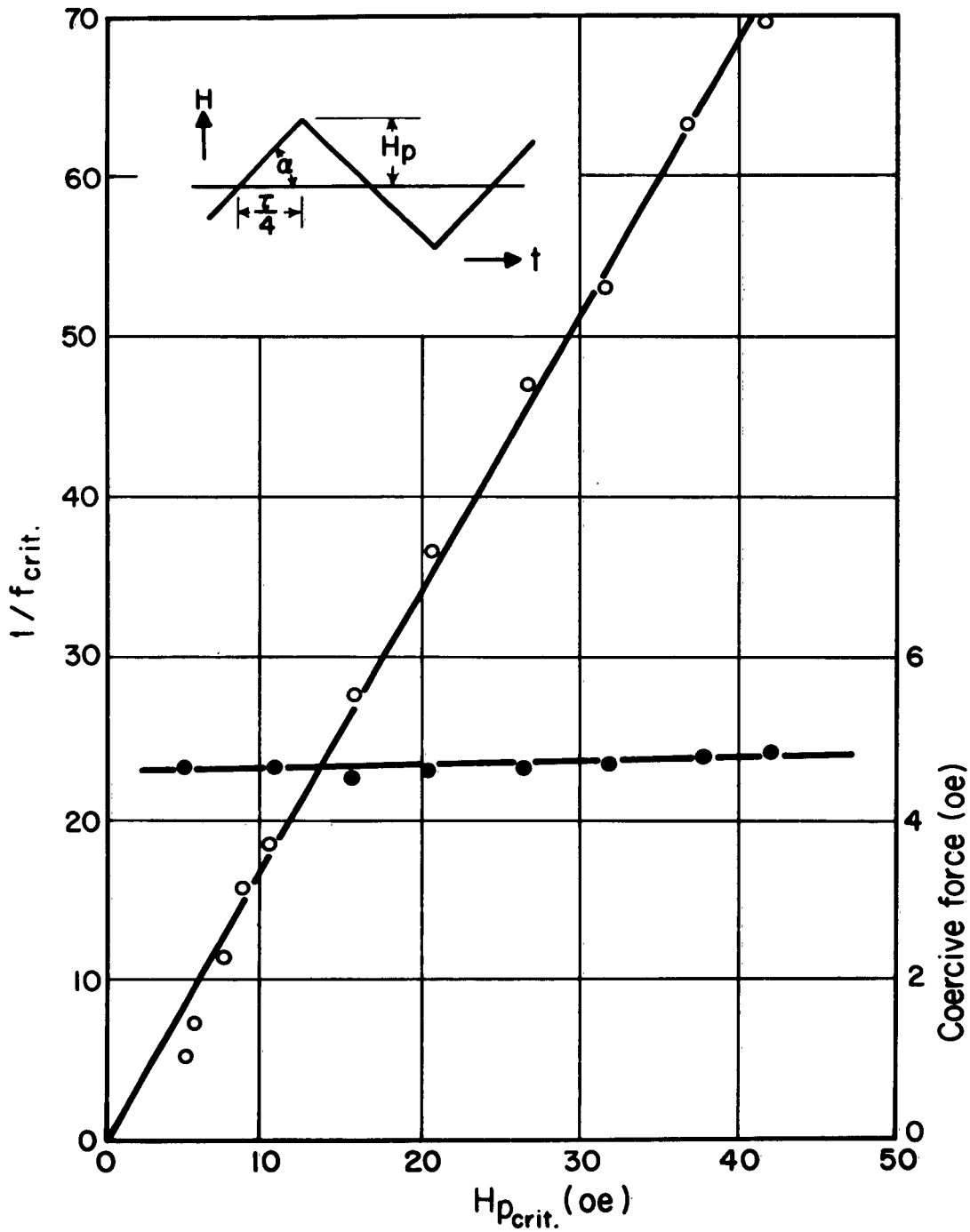

Fig. 6.5. Critical frequency and coercive field for polycrystalline YIG at -196°C. Excitation wave-form is shown in inset.

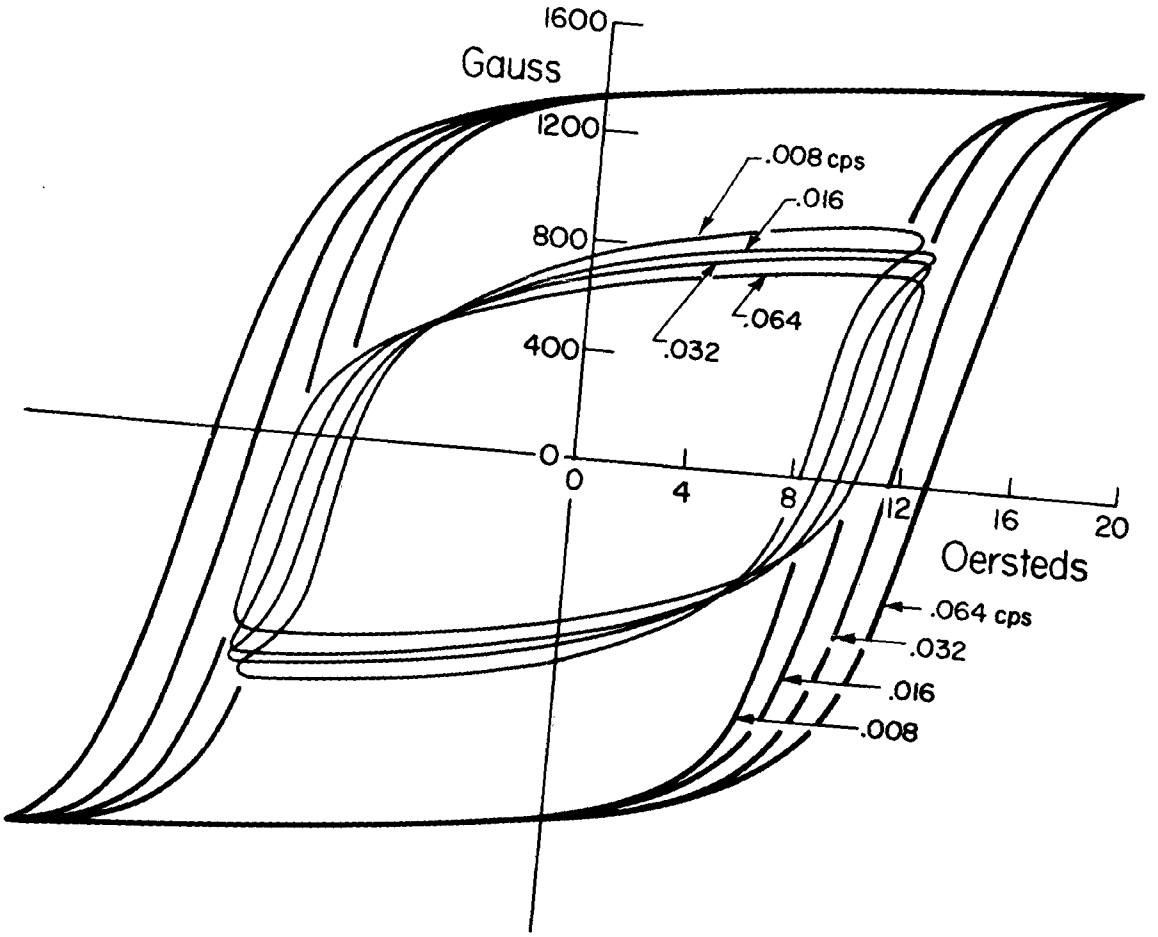

Fig. 6.6. Hysteresis loops for a YIG sample at -195°C. Frequency below threshold for dynamic squareness. Sinusoidal current excitation.

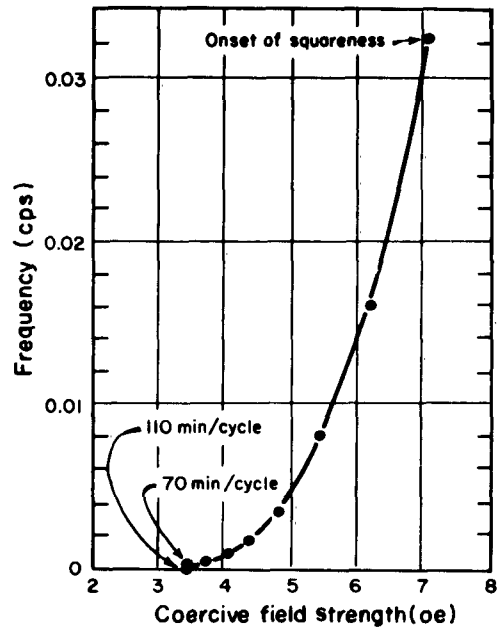

Fig. 6.7. Dependence of coercive force upon frequency for YIG sample at frequencies below threshold for dynamic squareness.

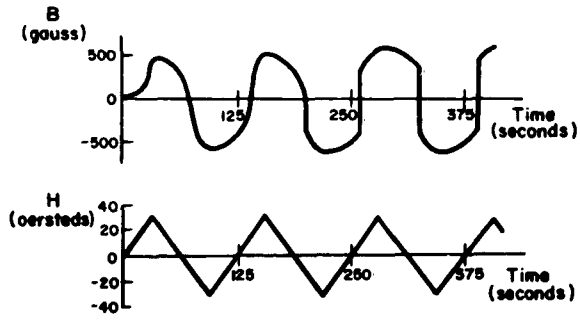

Fig. 6.8. Buildup of dynamic squareness in YIG.

occur. Fig. 6.8 shows measurements obtained on a YIG sample, demagnetized at room temperature, and then cooled to liquid nitrogen zero field. The upper curve in Fig. 6.8 shows, as a function of time, the magnetic induction which occurs in response to a triangular current excitation turned on at t = 0. It will be observed that the virgin curve (the response in the interval $0 < t < 31.25$ sec.) is normal. The response remains normal during the first full cycle of magnetization; in the second cycle a discontinuity in B occurs at the coercive field strength; in subsequent cycles, the discontinuity becomes more distinct, and eventually a steady state dynamically square loop is attained. This type of behavior strongly suggests that there is a close relation between dynamic squareness and magnetic anneal.

Low temperature loops in the region of dynamic squareness are shown in Fig. 6.9 for the series $(3 + x)Y_2O_3 \cdot (5 - x)Fe_2O_3$. The loop x = 0 was obtained on a high resistivity sample. Note that for this sample the loop is normal. Dynamic squareness is very pronounced in the compositions x = 0.1, -0.1, -0.2. With increasingly magnitude of x, there is a progressive deterioration of loop quality, but some evidence of squareness is present in all formulations except x = 0.4.

6.2 A Model for Dynamic Squareness *

The electron diffusion mechanism to which we have attributed permeability relaxation and magnetic anneal will also account for dynamic squareness. In what follows we present an analytical treatment of a model which, although simplified to make the problem tractable, contains those physical features we believe essential to dynamic squareness.

Consider the model for a magnetic crystal as shown in Fig. 6.10. Suppose there is present in the lattice some particle which can exhibit an activated mobility through the lattice and which can be trapped at a preferential site. Such a particle might, for example, be an impurity atom, an atomic defect, or, in our case, probably an electron attached to an iron atom. Because the model we will develop will apply to any one of these "defects" we shall not specify the precise nature of the "defect" but shall refer to the mobile particle, generically as a diffusant.

We shall assume that "1", "2", and "3" are trapping sites for diffusants.

---

* The analytical treatment of the model is presented here only in outline. A more detailed treatment is given by J. F. Janak in Technical Report 174, Laboratory for Insulation Research, November, 1962.

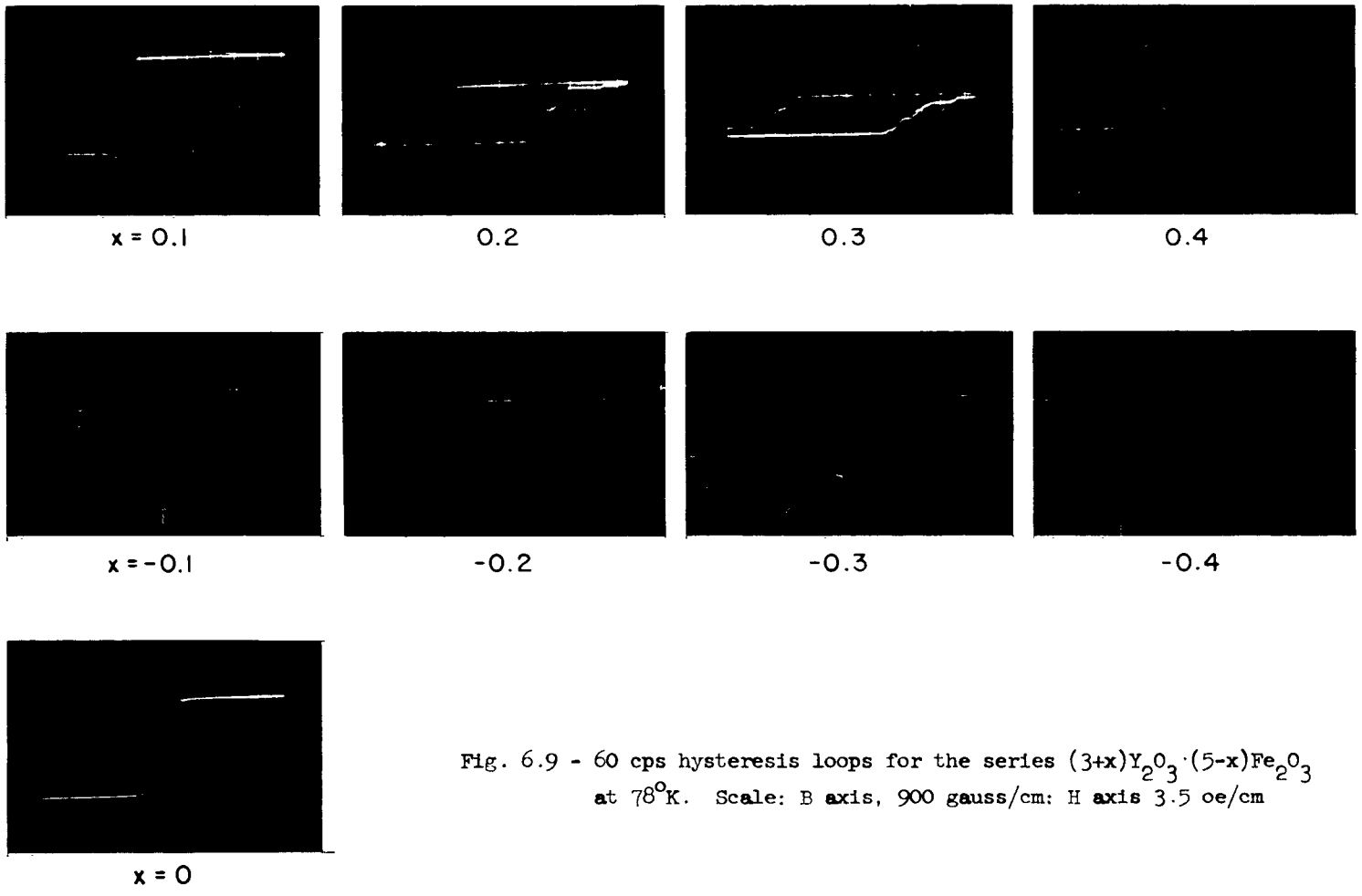

Fig. 6.9 - 60 cps hysteresis loops for the series $(3+x)Y_2O_3 \cdot (5-x)Fe_2O_3$ at 78°K. Scale: B axis, 900 gauss/cm: H axis 3.5 oe/cm

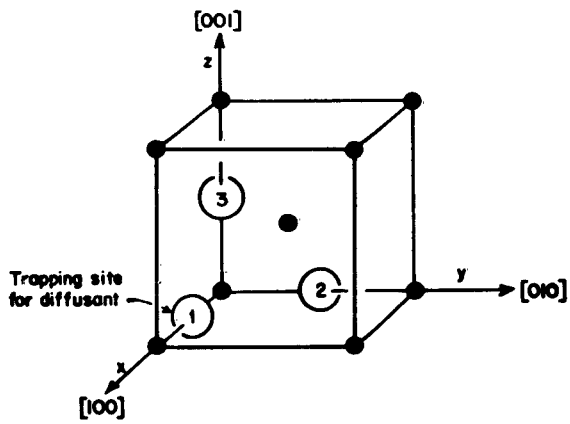

Fig. 6.10. Crystal structure employed in dynamic squareness model.

For a cubic crystal these are equivalent sites and, consequently, trapping at any one of the sites will occur with equal probability. However, we are dealing with a crystal which has a magnetic axis, one which is, therefore, only pseudo-cubic. Under these circumstances there will, in general, be a difference in trapping probability at the three sites. Let us assume that for the magnetic axis along x the preferred site is "1". If now, by the application of an external field, we shift the direction of spontaneous magnetization to y, site "2" becomes preferred and there must, accordingly, be a redistribution of diffusants. The process of redistribution is an irreversible one, hence energy extracted from the applied field has been dissipated within the lattice. Thus, the model provides a mechanism for magnetic loss.

In order to proceed on a quantitative basis we shall assume that the energy of the traps is related to the direction of spontaneous magnetization by the relation:

$$\epsilon_1 = \epsilon_o + a\alpha_1^2$$

$$\epsilon_2 = \epsilon_o + a\alpha_2^2 \qquad (6.5)$$

$$\epsilon_3 = \epsilon_o + a\alpha_3^2$$

where the α's are the direction cosines of the magnetization with respect to the cubic axes and "a" is an energy parameter. This energy level scheme is the same as that used by Néel[14] in analyzing some aspects of magnetic after effect in carbonyl iron. With the spontaneous magnetization along x, site "1" is preferred if $a < 0$, sites "2" and "3" are preferred if $a > 0$.

With N diffusants present per unit volume, the equilibrium population in one of the trapping sites, as obtained by the usual statistical procedures, is

$$n_{i\infty} = \frac{Ne^{-\epsilon_i/kT}}{\sum_i e^{-\epsilon_i/kT}} \quad ; \quad i = 1, 2, 3 \qquad (6.6)$$

and the average energy per diffusant is

$$u = \frac{\sum_i \epsilon_i e^{-\epsilon_i/kT}}{\sum_i e^{-\epsilon_i/kT}} \qquad (6.7)$$

---

[14] L. Néel, J. Phys. rad. 13, 249 (1952).

In a dynamic process, the direction cosines α_i are time dependent and, accordingly, the particle concentration at the several different sites and the energy of the system of diffusants both become functions of time. To evaluate the rate at which energy is dissipated it is necessary to know how the distribution of diffusants changes with time. We shall assume that the dynamic behavior of the distribution is such that the perturbed distribution will return to equilibrium according to a simple exponential law * governed by a single time constant τ. It is implicit in this assumption that the distribution function obeys the differential equation

$$\frac{dn_i(t)}{dt} = \frac{n_{i\infty}(t) - n_i(t)}{\tau} \tag{6.8}$$

which has the solution

$$n_i(t) = \int_{-\infty}^{t} e^{(\xi - t)/\tau} n_{i_\infty}(\xi) \frac{d\xi}{\tau} \tag{6.9}$$

where the initial conditions are specified somewhere in the interval $-\infty < t \leq 0$.

The energy of the system of N diffusants is

$$U = \sum n_i(t)\epsilon_i(t) = \int_{-\infty}^{t} e^{(\xi - t)/\tau} S(\xi, t) \frac{d\xi}{\tau} \tag{6.10}$$

where

$$S(\xi, t) = \frac{N \sum \epsilon_i(t)\, e^{-\epsilon_i(\xi)/kT}}{\sum_e e^{-\epsilon_i(\xi)/kT}} \tag{6.11}$$

We now consider the motion of a (001) domain wall in an infinite crystal having the structure shown in Fig. 6.10. For such a wall the magnetization lies in the (001) plane at an angle ϕ to the [100] direction, so that

---

* This assumption is the one used in simple rate theory.

$$\alpha_1 = \cos\phi$$

$$\alpha_2 = \sin\phi \qquad (6.12)$$

$$\alpha_3 = 0$$

It has been shown by Kittel[15] that such walls, under static conditions, have a structure given by

$$\tan\phi_s\,(z - z_o) = e^{(z - z_o)/d} \qquad (90^\circ \text{ wall}) \qquad (6.13)$$

$$\cot\phi_s\,(z - z_o) = -g \sinh\left(\frac{z - z_o}{d}\right) \qquad (180^\circ \text{ wall}) \qquad (6.14)$$

where z is the distance measured along [001] and z_o is the position at the center of the wall; g is a parameter which measures the ratio of magnetostrictive to anisotropy energy, * and d is the wall thickness parameter.

We shall assume that a moving wall retains its static structure during translation, an approximation which is good[16] as long as the wall velocity is so low that the kinetic energy density of the wall remains much smaller than the energy density in the static case. Velocities of ca 10^4 - 10^5 cm/sec are normally required before any significant alteration of the static structure will occur.

Within the domain wall the orientation of the magnetization changes with time, and thus the wall alters the local distribution of diffusants as it passes a given point. Because the modified distribution requires a finite relaxation time to settle back to equilibrium, the domain wall is followed by a wake of diffusants in out-of-equilibrium states. It is the energy dissipated in this wake that leads to the diffusion-damping force on the domain wall.

The rate at which work is done on the system of diffusants, per unit volume is

$$\frac{dW}{dt} = \sum_i n_i(t)\,\frac{d\epsilon_i}{dt} = \frac{d\phi}{dt}\sum_i n_i(t)\,\frac{\partial \epsilon_i}{\partial \phi} \qquad (6.15)$$

---

15 C. Kittel, Revs. Mod. Phys. 21, 541 (1950).

* For a 180° wall in the (100) plane it is necessary to introduce magnetostriction in order to make the wall determinate in z. Without magnetostriction the 180° wall consists of two 90° walls separated by an arbitrary distance.

16 J. V. Harrington, Lincoln Laboratory Technical Report 168 (1958).

Because the moving wall is functionally dependent on the quantity $z - z_o(t)$, i.e.

$$\phi = \phi_s \left[z - z_o(t) \right] \quad , \tag{6.16}$$

it follows that

$$\frac{d\phi}{dt} = - \frac{\partial \phi_s}{\partial z} \dot{z}_o \tag{6.17}$$

Using this relation and Eqs. 6.6 and 6.9, we can rewrite Eq. 6.15 in the form

$$\frac{dW}{dt} = - \dot{z}_o \frac{\partial \phi_s}{\partial z} \int_{-\infty}^{t} e^{(\xi - t)/\tau} f\left\{ \phi_s \left[z - z_o(t) \right] , \phi_s (z - z_o(\xi)) \right\} \frac{d\xi}{\tau} \tag{6.18}$$

where

$$f\left\{ \phi_1, \phi_2 \right\} = N \frac{\sum_i \frac{\partial \epsilon_i(\phi_1)}{\partial \phi_i} e^{-\epsilon_i(\phi_2)/kT}}{\sum_i e^{-\epsilon_i(\phi_2)/kT}} \tag{6.19}$$

The energy dissipated per unit area of domain wall is obtained by integrating over the complete extent of the wall in z. Accordingly, this dissipation is described by the function

$$R_d = h \dot{z}_o \int_{-\infty}^{t} e^{(\xi - t)/\tau} K\left[z_o(t) - z_o(\xi) \right] \frac{d\xi}{\tau} \tag{6.20}$$

in which,

$$K(u) = - \frac{N}{h} \int_{-\infty}^{+\infty} \frac{\partial \phi_s(z)}{\partial z} \frac{\sum_i \frac{\partial \epsilon_i \left[\phi_s(z) \right]}{\partial \phi_s} e^{-\epsilon_i \left[\phi_s(z+u) \right]/kT}}{\sum_i e^{-\epsilon_i \left[\phi_s(z+u) \right]/kT}} dz \tag{6.21}$$

with

$$u = z_o(t) - z_o(\xi)$$

and

$h = 1$, 90^o wall

$h = 2$, 180^o wall

In its exact form, K (u), which we shall refer to as the wall behavioral function, is quite unwieldy for computational purposes. However, it can be shown,[17] that to a good approximation we can take

$$K(u) = \frac{Na\ \lambda_o \tanh(cu/d)}{1 + 2\, e^{w/w_o} \cosh(u/w_o d)} \tag{6.22}$$

where

$$\cosh w = \frac{2}{g^2} - 1$$

and c, λ_o and w_o are curve matching parameters chosen to provide a fit to the actual behavioral function; all three parameters depend on a/kT. The approximation is a good one for $w \gtrsim 5$. (For carbonyl iron, for example, $w \simeq 8$.) The behavioral function for the 90^o wall is obtained by setting $w = \infty$.

The equation of motion for the wall is obtained by adding to the usual equation a dissipative force term $R_d/\dot{z}_o$:

$$\beta \dot{z}_o + h \int_{-\infty}^{t} e^{(\xi - t)/\tau} K(u)\, \frac{d\xi}{\tau} = h\mu_o M_s H(t) \tag{6.23}$$

The first term on the left, $\beta\, \dot{z}_o$, is a frictional force area resulting from intrinsic damping, the second term is the force area which originates in diffusion damping; the sum of these two are balanced by the pressure on the wall exerted by the driving

---

[17] J. F. Janak, M. I. T. Laboratory for Insulation Research Technical Report 174.

field H(t). *

The equation of motion may be written in a normalized form, convenient for further analysis, by defining

$$\rho = t/\tau \qquad \text{(normalized time)}$$

$$\zeta = \xi/\tau \qquad \text{(normalized time)}$$

$$y(\rho) = c\, z_o(t)/d \qquad \text{(normalized wall displacement)}$$

$$\gamma = \frac{\beta\, d}{Na\ \lambda_o c \tau\, h} \qquad \text{(normalized intrinsic damping constant)}$$

$$\Theta(\rho) = \frac{\mu_o M_s H(t)}{Na\ \lambda_o} \qquad \text{(normalized field)}$$

We then have

$$\gamma\, y'(\rho) + \int_{-\infty}^{\rho} e^{-(\rho - \zeta)} F\left[y(\rho) - y(\zeta)\right] d\zeta = \Theta(\rho) \qquad (6.24)$$

We now examine this result for a wall moving with constant velocity. For this situation we have

$$y(\rho) = 0, \quad \rho < 0 \qquad (6.25)$$

$$y(\rho) = p\, u_{-2}(\rho) \qquad (6.26)$$

where u_{-2} is a unit ramp function and

$$p = \frac{cv\tau}{d} \qquad (6.27)$$

is the normalized value of the actual wall velocity v.

For the assumed behavior of $y(\rho)$ the equation of motion reduces to

$$\gamma p + \frac{1}{2} e^{-\rho} F(\rho\rho) + \int_{o}^{\rho} e^{-x} F(px)\, dx = \Theta(\rho) \qquad (6.28)$$

---

* Here it must be understood that H(t) is the field in excess of that required to break the wall free of local traps.

In the limit $\rho \to \infty$, $e^{-\rho} \to 0$ and, because $F(p\rho)$ is always finite, we obtain the further simplification

$$\gamma p + G(p,\infty) = \Theta(\infty) \tag{6.29}$$

where

$$G(p,\infty) = \int_0^\infty e^{-x} F(p,x)\, dx \tag{6.30}$$

In its explicit form the function G is given by

$$G(p,\infty) = \int_0^\infty \frac{e^{-x} \tanh px\, dx}{1 + 2e^{-w/w_o} \cosh(px/cw_o)} \tag{6.31}$$

The evaluation of this integral has been carried out by Janak[17] who has obtained the curves of p vs. Θ shown in Fig. 6.11. It will be recognized that these are in fact plots of normalized velocity vs. the normalized field required to maintain constant wall velocity in the presence of diffusion damping; that is, the plots represent the functional relation

$$G(p,\infty) \triangleq \gamma_d p = \Theta(\infty) \tag{6.32}$$

where γ_d is a velocity dependent diffusion damping coefficient. If the intrinsic damping is added, the steady state wall motion is governed by the relation

$$(\gamma + \gamma_d)\, p = \Theta(\infty) \tag{6.33}$$

which is plotted in Fig. 6.12 for both 90° and 180° walls. These curves point up the significant difference between 90° and 180° wall behavior. For the former, the incremental damping $d\Theta/dp$ is always positive. For the 180° wall, however, there is a region of negative damping. This region is entered when the wall exceeds a critical velocity, at which point the wall becomes unstable. We suggest that dynamic squareness has its origin in this type of instability.

In our analysis we have focussed on the behavior of a single wall which has attained a steady state velocity in response to an applied field of constant amplitude.

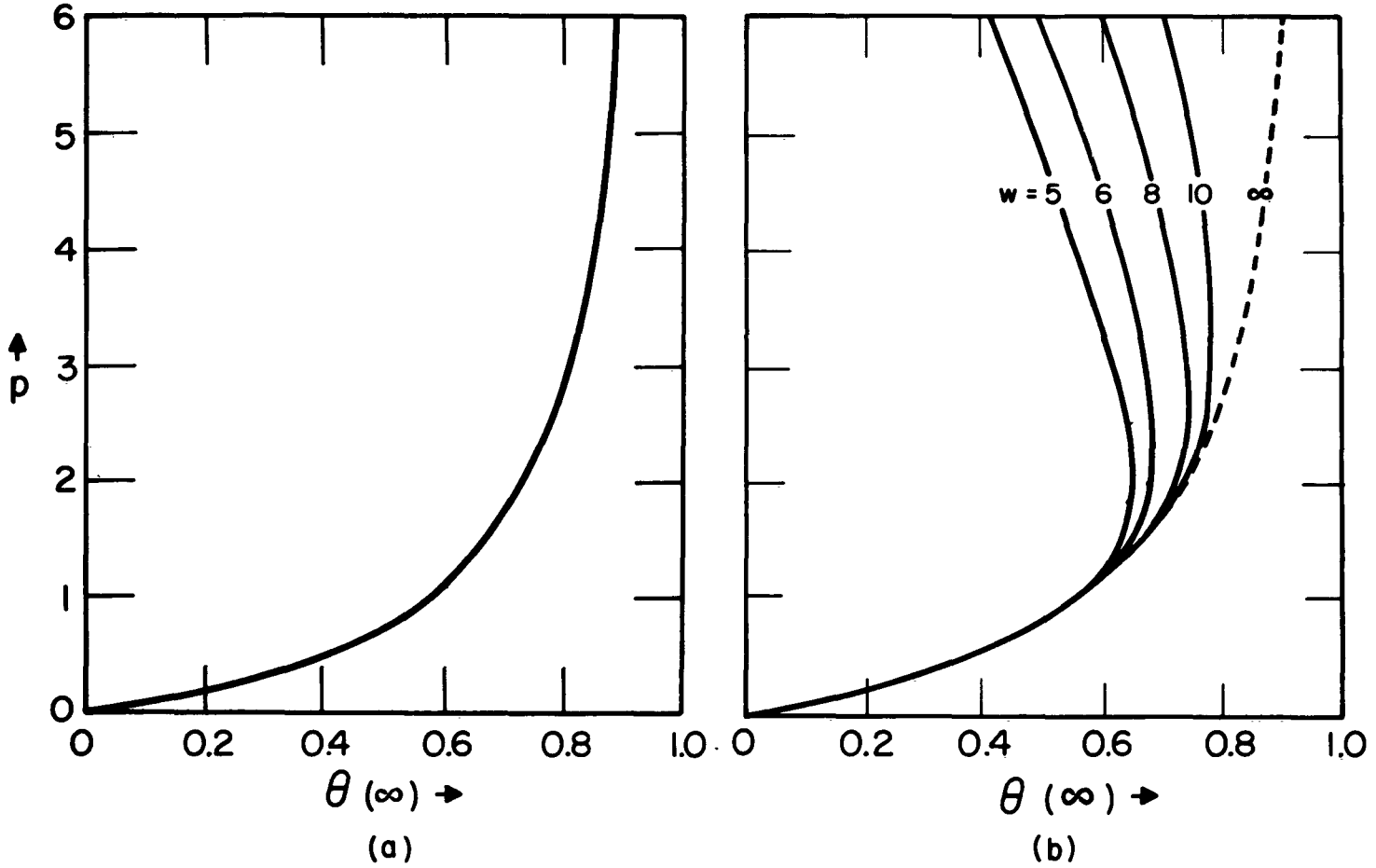

Fig. 6.11. Velocity vs. field for diffusion-damped domain wall: (a) 90°; (b) 180° wall. In (b), curve w = ∞ is identical to that for 90° wall.

In our experiments, however, we are dealing with polycrystalline material involving many walls and the excitation is cyclic. Under these circumstances the theory that has been developed can be used only as a guide in explaining the data. Viewed in this light, however, we find that the steady state analysis accounts for many features of the experimental results:

1. In the region of dynamic squareness the coercive force is found to be essentially independent of the amplitude or frequency of excitation (Fig. 6.5.) The analysis reveals that there is a critical field for instability (Fig. 6.12.)
2. Experimentally we find that the onset of squareness is determined by the slope of the triangular drive waveform. To explain this result we must first recognize that in a real material a domain wall is bounded in the distance it can travel. The bounded wall will only go unstable if it reaches critical velocity before it runs out of available space. Stated in a slightly different way, the wall will remain stable unless it achieves its critical velocity in a time less than that required to traverse its dimensional bounds. This requirement for a minimum time of excitation plus the existence of a critical field provides a qualitative explanation of the observed "critical slope."
3. We have noted that instability is a property of 180° walls and not of 90° walls. In our samples it would appear that the development of 180° walls is promoted by magnetic anneal. The data of Fig. 6.8 shows quite clearly that dynamic squareness does not occur unless there has been some prior exposure to a magnetizing field.

In connection with our steady state analysis, a final remark should be made. At low velocities the curves p vs. Θ for both 90° and 180° walls become identical. It can be shown that they take the form

$$p = \frac{\Theta(\infty)}{1+\gamma} + \frac{2\left[\Theta(\infty)\right]^3}{(1+\gamma)^4} + \ldots . \qquad (6.34)$$

For $\gamma \ll 1$, $a/kT \ll 1$, the expression can be shown to simplify to

$$v = \frac{4.5\,\mu_o M_s\, d}{\left(\frac{Na^2}{kT}\right)\tau} H \qquad (6.35)$$

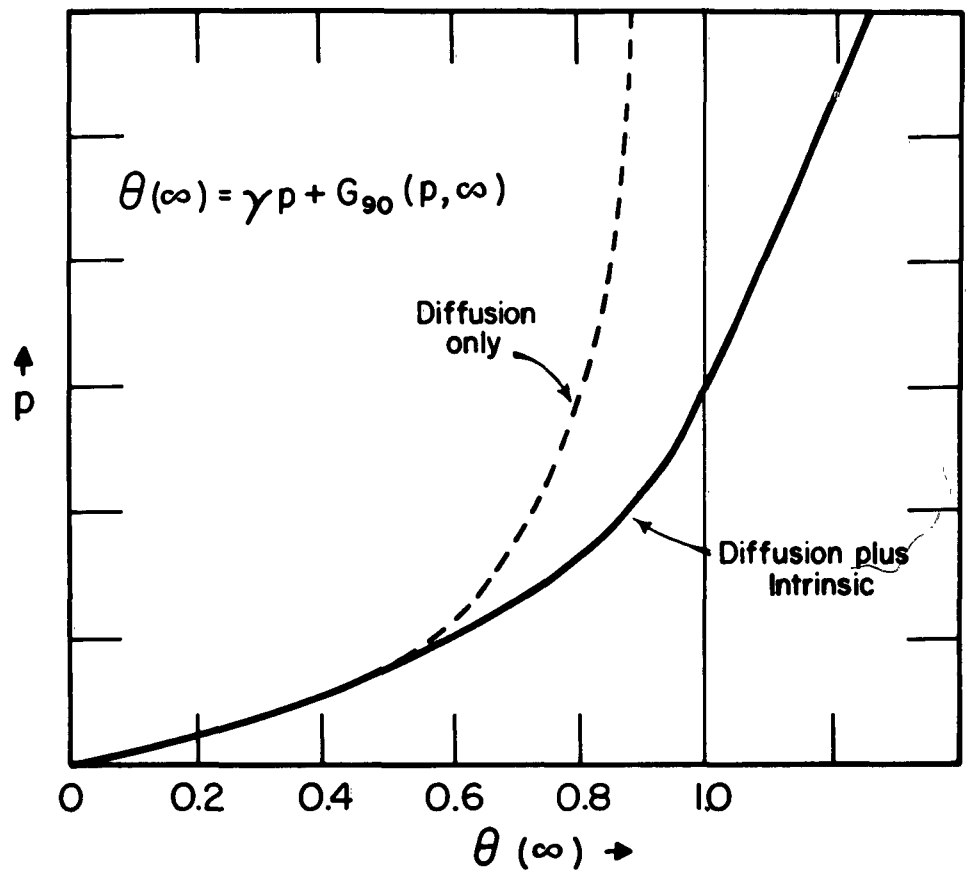

Fig. 6.12a. Velocity vs. field for 90° wall subjected to diffusion plus intrinsic damping.

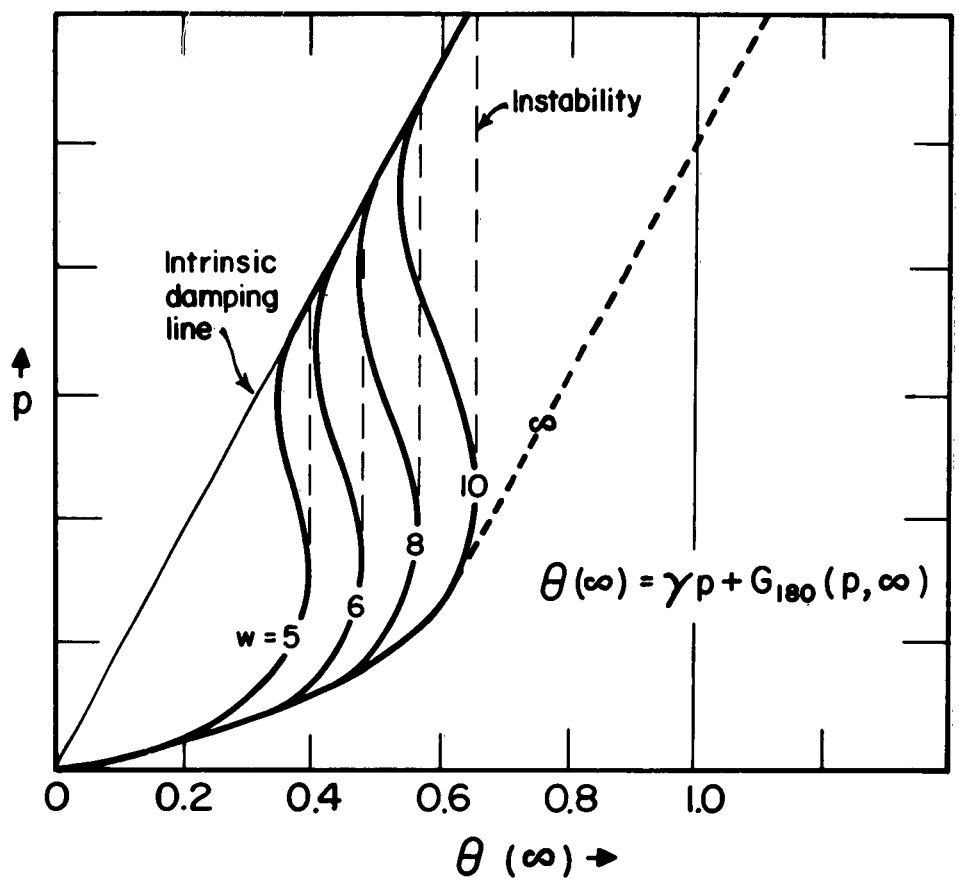

Fig. 6.12b. Velocity vs. field for 180° wall subjected to diffusion plus intrinsic damping. The dashed vertical lines indicate the discontinuous change in velocity at the point of instability. The curve $w = \infty$ is identical to that for the 90° wall (see Fig. 6.12a).

Except for the value of the numerical coefficient this result is identical to that obtained by Clogston (see Eq. 4.12) who treated the diffusion-damping problem in spinel in the limit of low velocities. The numerical differences arise because Clogston, in his analysis, considered a wall structure and an energy level scheme for diffusants appropriate to a typical ferrimagnetic spinel. The wall structure and energy level diagram used in the present work, as has already been noted, really applies to carbonyl iron rather than to garnet (or spinel). This particular choice was made in order to make the mathematics of the problem manageable. The use of the more appropriate model would lead to no alteration in the functional form of any results but only to slight modifications of numerical factors. Because the existing data does not yet permit a quantitative check with theory, further refinement of the theoretical treatment appears unwarranted at this time.

7. OPTICAL STUDIES

The existence of a pronounced optical Faraday effect in ferrimagnetic garnets makes it possible to study the magnetic domain structure in these materials by direct observation under the microscope. We have attempted to use the Faraday effect to determine whether any preferential domain alignment occurred in polycrystalline samples of YIG as a result of magnetic anneal.

A number of investigators [18, 19] have reported on magnetic domains observed in single crystal garnets and most of these results we were able to reproduce in our studies. However, there have been no reports in the literature of domains seen in polycrystalline garnets. Although we were successful in finding such domains, we were unable to find evidence of a preferential domain structure being formed after cooling in an annealing field. We attribute this failure to the fact that the domain structure in the thin polycrystalline wafers used in our optical investigation were determined by strains rather than by magnetic anisotropy. We feel that suitable polishing and etching techniques capable of producing strain free polycrystalline samples could have been worked out had we additional time.

---

[18] J. F. Dillon, J. Appl. Phys. 29, 1286 (1958).
[19] P. A. Miles, M. I. T. Laboratory for Insulation Research Prog. Rept. XXI, June, 1957, p.20.

7.1 Sample Preparation

The observation of domains by the Faraday effect requires plates about 0.001" thick. Samples of the required thickness can be prepared by the usual optical grinding and polishing techniques. However, considerable care must be exerted to prevent sample breakage as the finishing stages of polishing are reached. The following procedure was used.

The sample, either an oriented slice of single crystal, or a polycrystalline disk was cemented to a flat glass block about 2" x 2" and 1/2" thick. Several cementing agents were used; these included sealing wax, shellac, Duco cement, and Canada balsam. All were satisfactory in holding the sample until it was ground and polished to a thickness of about 5 mils. Below this thickness only Canada balsam was effective in preventing the sample from pulling away from the polishing block.

After polishing down to roughly 5 mils on the first side, the sample was remounted for grinding and polishing on the second side. To mount the sample the block was heated to 85°C; a layer of Canada balsam, thinned with xylene, was applied to the block and the sample was placed on the block, polished face down. Extreme care must be taken to avoid air bubbles under the sample lest local stresses capable of breaking the sample develop during subsequent grinding. Several brass washers, approximately the same thickness on the sample, were mounted around the sample to insure more even grinding, and the entire surface of the block was then covered with several thin layers of balsam. The block was heated for about 15 minutes at 85°C to allow the xylene thinner to evaporate. Slow subsequent cooling to room temperature minimized cracking of the balsam cement.

When the specimen is reduced to a thickness below ca 0.006" it begins to transmit red light. As the thickness further decreases to 0.002" the color changes to yellow. This effect is useful as a check on both the thickness and the uniformity of grinding.

The initial grinding was done with emery paper, followed by grinding and polishing with progressively finer abrasives in a water slurry. Final polishing was with A. O. 309 polishing compound for about 30 minutes.

7.2 Experimental Equipment

For studies at room temperature the prepared wafers are simply mounted on slides placed on the stage of a polarizing microscope. For studies at low

temperature a suitable observing cell must be provided.

The low temperature cell used in our early efforts is shown in Fig. 7.1. The central part of the brass tube assembly was immersed in a suitable low temperature bath during viewing. The sample was mounted on a glass slide supported by the central flange. The folded optical path was achieved by placing a front surface mirror at each bend. Observation of the sample was made with a long working-distance (lwd) microscope fabricated from two conventional objectives. The unit had a working distance of about 1" at 75x magnification.

This arrangement proved unsatisfactory due to warping of the optical path when the U-tube was cooled. In a second arrangement, we employed a Dewar with viewing slits in the silvering. The sample was immersed in liquid nitrogen in the Dewar, and observed through the liquid nitrogen and Dewar walls with the lwd microscope. Because of the lack of field flatness in the lwd microscope, and because of difficulties with sample vibration, this arrangement was abandoned.

A simple and effective scheme was finally evolved. A special low-temperature stage was designed to mount directly on the stage of a conventional polarizing microscope. The sample was mounted in a windowed inner chamber and cooled with nitrogen gas, the gas being kept cool by an outer jacket filled with liquid nitrogen. Only a single window intervenes between sample and microscope objective. The optics were kept from frosting by enclosing the entire microscope in a plastic bag filled with dry nitrogen gas under positive pressure.

7.3 Results

Single crystal plates prepared by the foregoing procedure show a maze pattern (Fig. 7.2.) On the first crystal we prepared we were able to eliminate the maze structure by etching the crystal for 30 minutes in boiling HCl. In subsequent plates, prepared from different crystals, * this etching technique failed to work. An explanation for this difference in behavior is not known. It is of interest to note that Dillon has reported that he was able to eliminate the maze only by very fine polishing and not by etching.

It has been suggested by Dillon that the maze patterns are a result of surface strains. As a check on this hypothesis we carried out the following experiment. Our etched single crystal, which initially showed no maze structure, was cemented to a heated glass substrate, and the assembly was allowed to cool. Observations on the cooled crystal showed the maze structure; upon dissolving away the restraining

---

* Several different slices of YIG crystal were obtained from Bell Telephone Laboratories; their detailed history is not known.

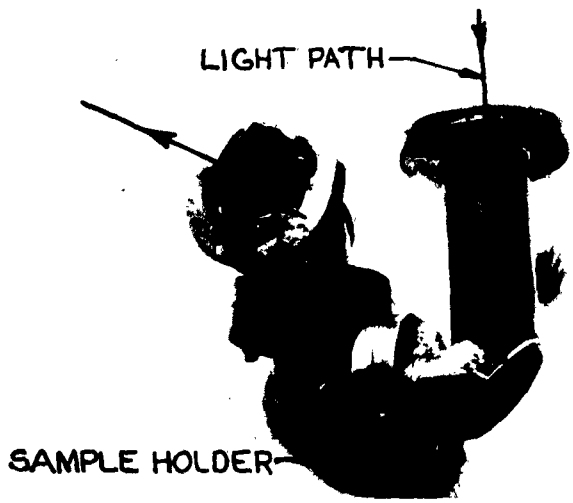

Fig. 7.1. The periscope sample holder.

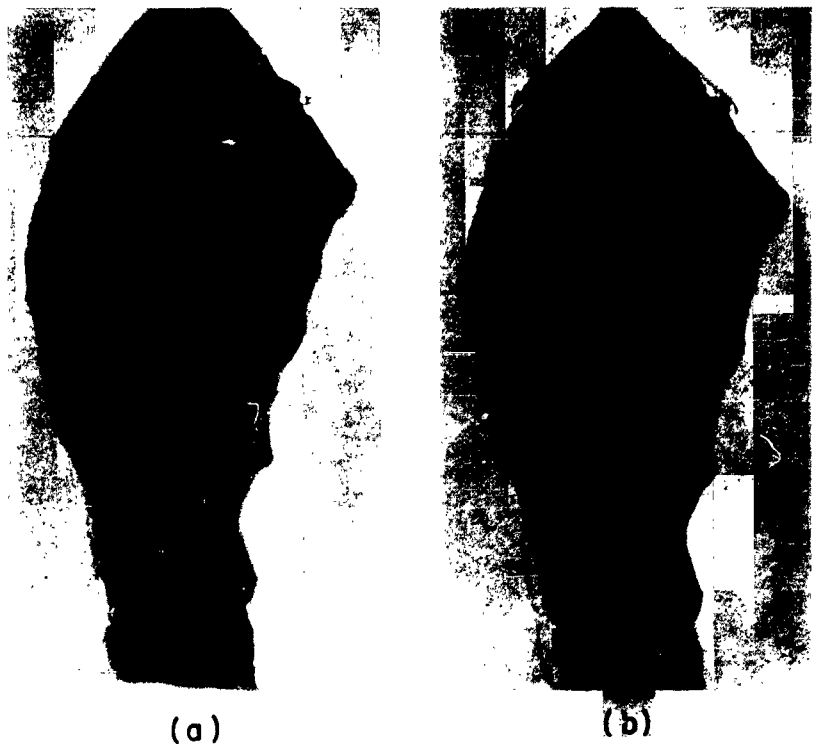

Fig. 7.2. Domain patterns in YIG single crystal: (a) no applied field; (b) field inclined to sample plane but with main component in [111] direction.

Fig. 7.3. Domain structure in polycrystalline YIG wafer: (a) no applied field; (b) applied field sufficient to saturate specimen in plane of sample.

cement the maze disappeared.

Our polycrystalline samples showed a complicated maze structure (Fig. 7.3) which we believe to be largely due to surface strains. Attempts to modify the domain pattern by etching were not successful; the etchant, as might be anticipated, preferentially attacks the grain boundaries, and the polycrystalline sample is destroyed long before there is an effect on the individual crystallites.

Polycrystalline samples were cooled to liquid-nitrogen temperature in an annealing field applied by passing d.c. current through a wire threading the sample. Fields up to 20 oersteds were obtained in this way. The domain pattern, in zero field, was found to be unaffected by magnetic anneal in its essential character.

8. MAGNETOSTRICTION *

The magnetostrictive properties of a magnetic material can have a profound effect upon its domain structure and, consequently, upon many of its technical properties. In stoichiometric YIG, where the only magnetic ion, Fe^{3+}, is in an s-state, we would anticipate that the magnetostriction is small. However, the existence of strain-induced maze patterns in single crystals indicates that under conditions of large strain the magnetostrictive energy can become comparable to the anisotropy energy.

At the beginning of the present study there had been, to our knowledge, no report in the literature of any magnetostrictive work on the garnets. During the course of our program the work of Nakamura and Sugiura[20] on polycrystalline YIG was published. Our results are in marked disagreement with theirs. In addition, we have carried out magnetostrictive measurements on a single crystal sample.

8.1 Experimental Procedure

Our magnetostriction measurements were made with a strain-gauge bridge (Fig. 8.1), using Baldwin-Lima-Hamilton SR-4 gauges, Model A-19. This is a paper-backed gauge with a wire-wound constantan element approximately 2 mm square.

---

* A fuller presentation of the work described in this chapter is contained in an M. I. T. Master's Thesis, Course VI, by A. S. Foster, January, 1961.

[20] A. Nakamura and Y. Sugiura, J. Phys. Soc. Japan 15, 1704 (1960).

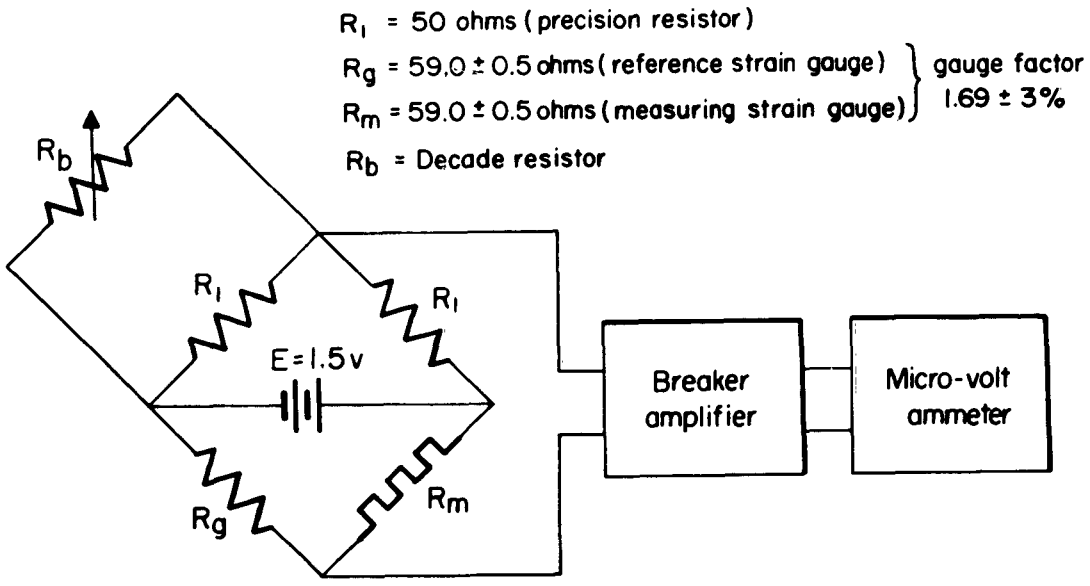

Fig. 8.1. Electrical arrangement for magnetostriction measurements.

The measuring gauge (R_m in Fig. 8.1) was fastened to the sample with Duco cement, with the primary axis of the gauge aligned along the desired crystallographic axis. Gauge sensitivity in the direction perpendicular to the primary axis was less than 0.5 percent of the primary sensitivity. Variations in gauge resistance with temperature were compensated for by using another gauge as one of the bridge arms, and including it in the same temperature environment.

When a strain occurs, the bridge is rebalanced by varying the resistance of one of the opposite arms of the bridge. In the system employed (Fig. 8.1):

$R_g = R_m = 59.0 \pm 0.5$ ohms

$R_1 = 50$ ohms, General Radio precision resistors

R_b: General Radio decade resistor, type 1432-M

$G = 1.69 \pm 3$ percent (gauge factor)

It is easily shown that the strain is related to the change in resistance setting of R_b by:

$$\frac{\Delta \ell}{\ell} = \frac{50\,\Delta R_b}{1.69\,(R_b + 50)^2} \qquad (8.1)$$

In order to minimize thermal junction effects in the bridge circuit, an insulated interconnection box was used. Connections were made on copper blocks inside a grounded aluminum box covered with styrofoam. All leads were shielded.

Bridge unbalance was measured with a Perkin-Elmer breaker amplifier feeding a Hewlett-Packard micro-volt-ammeter. The sensitivity was limited by system noise equivalent to a strain of about 10^{-7}.

Because the gauges used contained a small element area in a relatively large paper area, it was possible to maintain angular alignment in the sample holder by clamping the gauge paper border. The sample was then constrained only by the gauge paper and the cement, which contribute small but unknown stresses.

8.2 Phenomenological Theory

The fractional change in length of a single crystal measured in a direction, relative to the crystallographic axes, given by the direction cosines $\beta_1, \beta_2, \beta_3$ is[21]

$$\begin{aligned}\frac{\delta l}{l} &= h_1 (\alpha_1^2 \beta_1^2 + \alpha_2^2 \beta_2^2 + \alpha_3^2 \beta_3^2 - 1/3) \\ &+ h_2 (2\alpha_1\alpha_2\beta_1\beta_2 + 2\alpha_2\alpha_3\beta_2\beta_3 + 2\alpha_3\alpha_1\beta_3\beta_1) \\ &+ h_3 \\ &+ h_4 (\alpha_1^4 \beta_1^2 + \alpha_2^4 \beta_2^2 + \alpha_3^4 \beta_3^2 - 1/3) \\ &+ h_5 (2\alpha_1\alpha_2\alpha_3^2 \beta_1\beta_2 + 2\alpha_2\alpha_3\alpha_1^2 \beta_2\beta_3 + 2\alpha_3\alpha_1\alpha_2^2 \beta_3\beta_1)\end{aligned} \tag{8.2}$$

where the α's are the direction cosines of the magnetization and the h's are phenomenological coefficients. In this expression the right-hand side has been arranged to satisfy the zero condition $\frac{\delta l}{l} = 0$ when the domains are equally distributed among the easy conditions. The h_3 term, a contribution from the volume magnetostriction, is independent of the direction of magnetization.

Though experimental evidence has indicated that terms beyond those included above are sometimes necessary for a complete description, it is often found that the first two terms are sufficient to give reasonable results. It is then convenient to modify the form of the above equations. If we consider the magnetostriction in the direction of the magnetization, then we find that the saturation magnetostrictions along the principal axes are:

$$\lambda_{100} = 2/3\, h_1$$

$$\lambda_{111} = 2/3\, h_2$$

These are the coefficients that are usually measured, and used to specify the magnetostrictive properties of a single crystal. Under these circumstances

---

[21] K. H. Stewart, "Ferromagnetic Domains", Cambridge Press (1954); p. 45

Eq. 8.2 may be rewritten as

$$\frac{\delta l}{l} = \frac{3}{2}\lambda_{100}\left(\alpha_1^2\beta_1^2 + \alpha_2^2\beta_2^2 + \alpha_3^2\beta_3^2 - 1/3\right) + 3\lambda_{111}\left(\alpha_1\alpha_2\beta_1\beta_2 + \alpha_1\alpha_3\beta_1\beta_3 + \alpha_2\alpha_3\beta_2\beta_3\right) \tag{8.3}$$

For a polycrystalline material the saturation magnetostriction measured in the direction of the magnetizing field is obtained by averaging Eq. 8.3 over all possible crystallite orientations:

$$\frac{\delta l}{l} = \lambda_{s\text{-par}} = \frac{2\lambda_{100} + 3\lambda_{111}}{5} \tag{8.4}$$

For the strain measured at an angle Θ with respect to the applied field,

$$\frac{\delta l}{l} = \frac{3}{2}\lambda_{s\text{-par}}\left(\cos^2\Theta - 1/3\right) \tag{8.5}$$

8.3 Experimental Results

Magnetostriction measurements were made on a small single crystal disk (0 095" dia. by 0.0325" thick) of YIG * at several different temperatures. The variation of λ_{111} with applied field at 27°C is shown in Fig. 8.2. The magnetostriction in the other two principal directions, [100] and [110] was found to be very close to the limit of detectability. Saturation values for the magneotstriction coefficients at 27° C are listed in Table IV. Measurements at -76°C revealed that saturation values were essentially unchanged from the room-temperature figures.

---

* The disk was cut from a slice of crystal obtained from the Bell Telephone Laboratories.

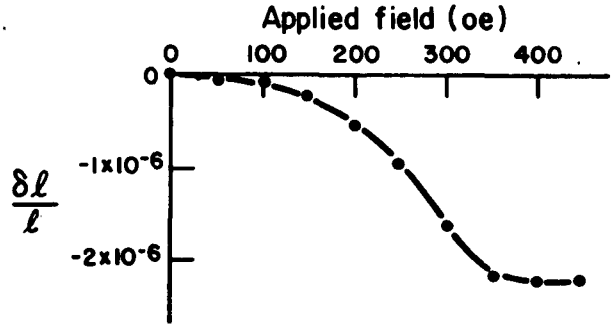

Fig. 8.2. Magnetostriction in [111] for single crystal (110)-plane disk of YIG.

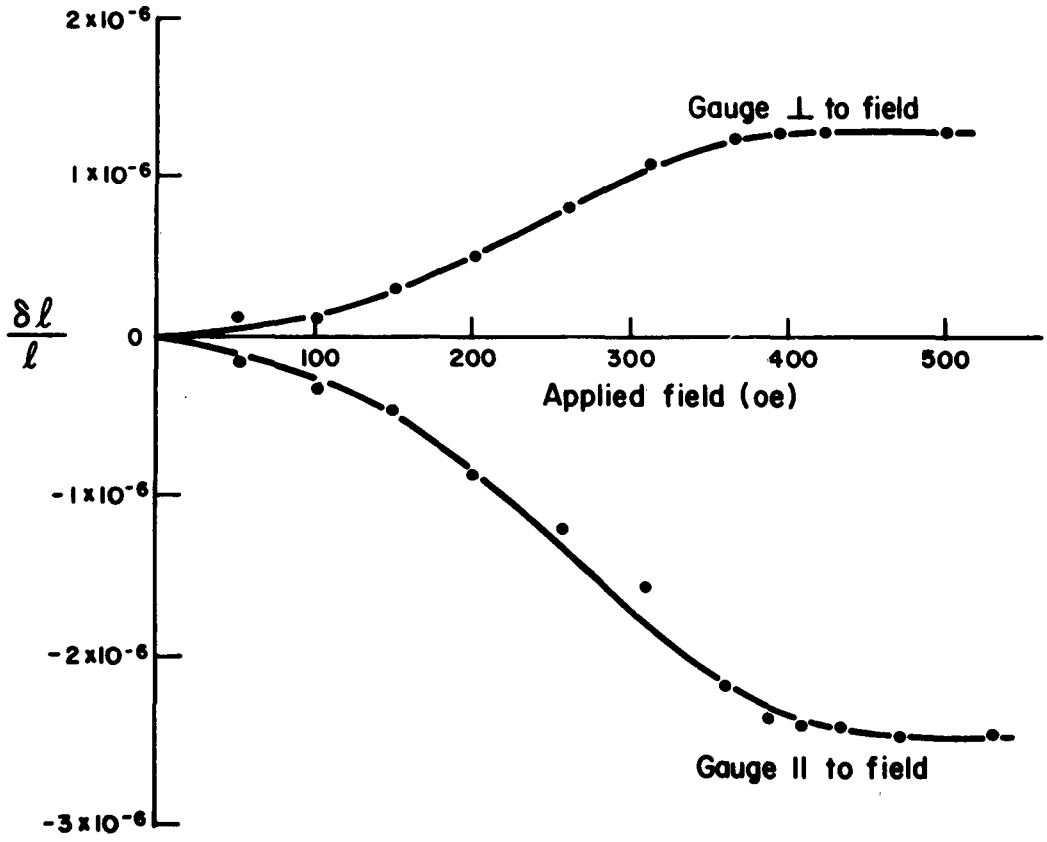

Fig. 8.3. Magnetostriction measurements on polycrystalline YIG disk at 25°C.

TABLE IV

Saturation Magnetostriction for Single Crystal YIG at 27°C

Coefficient	Value
λ_{111}	-2.1×10^{-6}
λ_{100}	$<0.1 \times 10^{-6}$
λ_{110}	$<0.5 \times 10^{-6}$

Measurements on a polycrystalline disk are shown in Fig. 8.3. Based on our single crystal data and the use of Eq. 8.4 we would predict for the polycrystalline disk $\lambda_{s\text{-}par} \approx -1.2 \times 10^{-6}$. Our actual measurements give -2.5×10^{-6}, in fair agreement with the predicted value, but at considerable variance with the value $\lambda_{s\text{-}par} = -0.37 \times 10^{-6}$ reported by Nakamura and Sugiura.[20]

9. CONDUCTIVITY IN VANADIUM AND TITANIUM OXIDES

The electrical conductivity studies described in the present Chapter, although an outgrowth of our interest in the electrical properties of garnets, represent a digression from the main theme of the contract. However, because the results are of general interest and, in many respects, are new, we felt that they should be included in this final report.

The present work, to our knowledge, represents the first systematic study of V_2O_3 as an oxidation-reduction semiconductor. We have established that the p-type metallic conduction observed in the vicinity of room temperature is independent of any deviation from the correct oxygen content; however, in the low-temperature phase of V_2O_3 (occurring below ca 160°K) reduced samples are n-type, oxygen rich samples p-type. We have also found that, when suitably doped, V_2O_3 is a well-behaved valency controlled semiconductor. In an effort to determine whether d-band impurity conduction might occur we studied V_2O_3 doped with Ti and Cr. The experimental results are presented, but their interpretation with respect to d-band conduction remains inconclusive.

Our conductivity studies on TiO_2 are for the most parts confirmatory of high-temperature data reported in the literature. What is new about this work is the experimental technique, one which involved the preparation in situ of TiO_2 from pure titanium metal. It was originally hoped that by making electrical measurements in a controlled environment at high temperature we could detect phase transformations among the several different oxides of titanium. However, under the conditions of our experiment only TiO_2 proved to be stable.

9.1 Properties of V_2O_3 *

Vanadium sesquioxide is one of a class of compounds having the general formula $Me_2^{3+}O_3$ where the metal cation may be Ga, Al, Ti, V, Cr, Fe, or two or more of these in solid solution. These compounds normally crystallize in the corundum structure.

V_2O_3 is known to exhibit two transitions, one a first order transition occurring at 160°K, the other, which is second order, occurs at 500°K. Upon warming through the low temperature transition the resistivity decreases by 5-6 orders of magnitude. Below 160°K the material is semiconducting while in the region 160°K - 300°K the conductivity appears metallic. At higher temperature the resistivity traverses a broad maximum centered at 500°K.

Although oxide semiconductors are known to be very sensitive to deviations from stoichiometry there has not, until this present study, been any comprehensive investigation of the effects of oxygen content on the electrical properties of V_2O_3. To acquire this essential information, a series of V_2O_3 samples were prepared by reducing bars of V_2O_5 in hydrogen at different temperatures. Conductivity and thermoelectric data on the resultant ceramic samples are shown in Figs. 9.1 and 9.2. Apart from differences in the magnitude of the low temperature conductivity, no essential difference among the samples appears in the conductivity data of Fig. 9.1. However, the thermoelectric data is extremely revealing. † Here, below the

---

* A more complete presentation of the work on V_2O_3 is contained in a Laboratory for Insulation Research Technical Report by A. J. MacMillan; No. 172.

† Our thermoelectric measurements required that a temperature gradient of at least 5°C be maintained across the sample. Consequently, reliable data could not be otbained in the vicinity of the transition. This state of affairs is indicated by the use of dashed lines in Fig. 9.2.

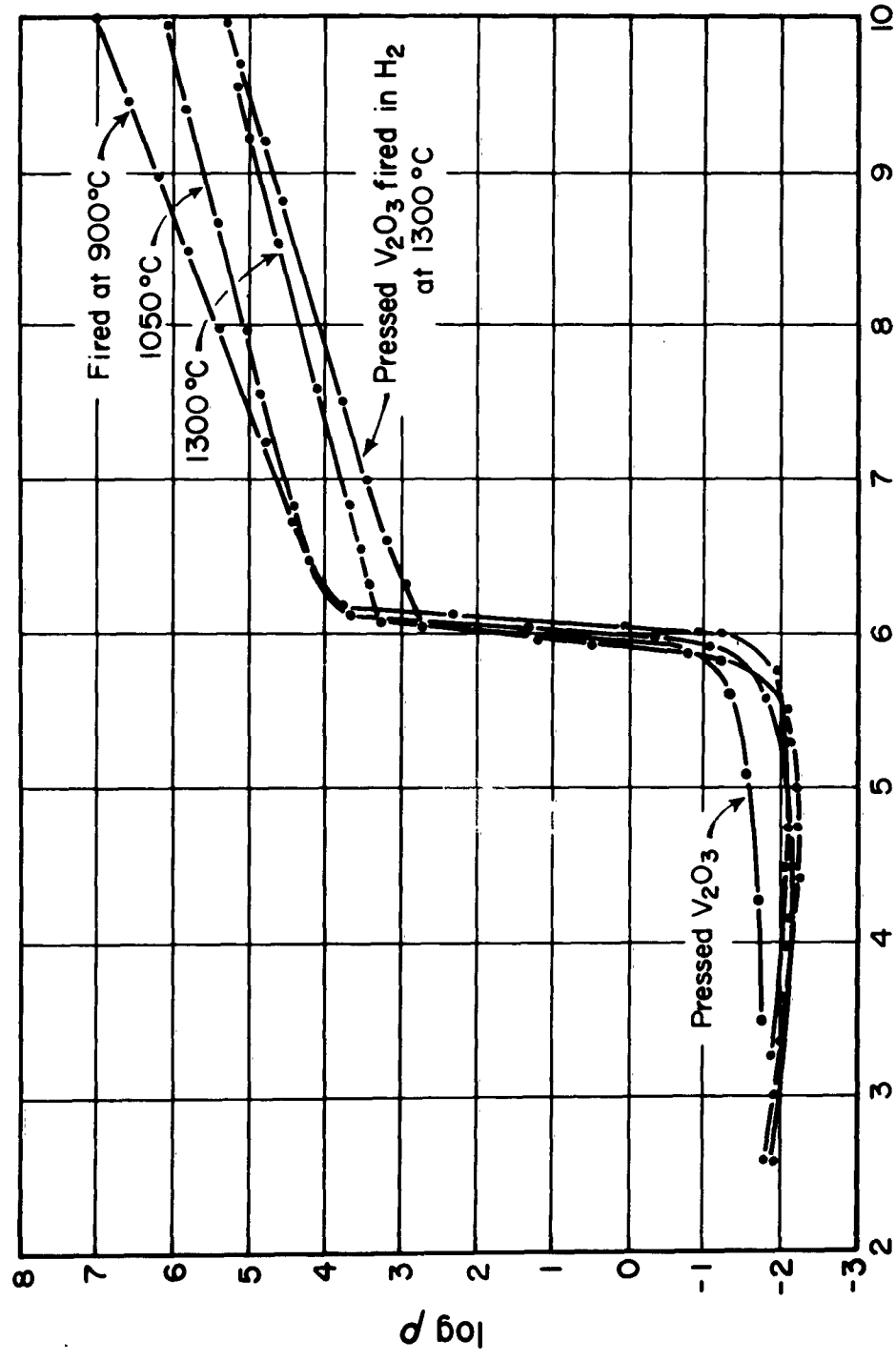

Fig. 9.1. Resistivity of V_2O_3 as a function of temperature.

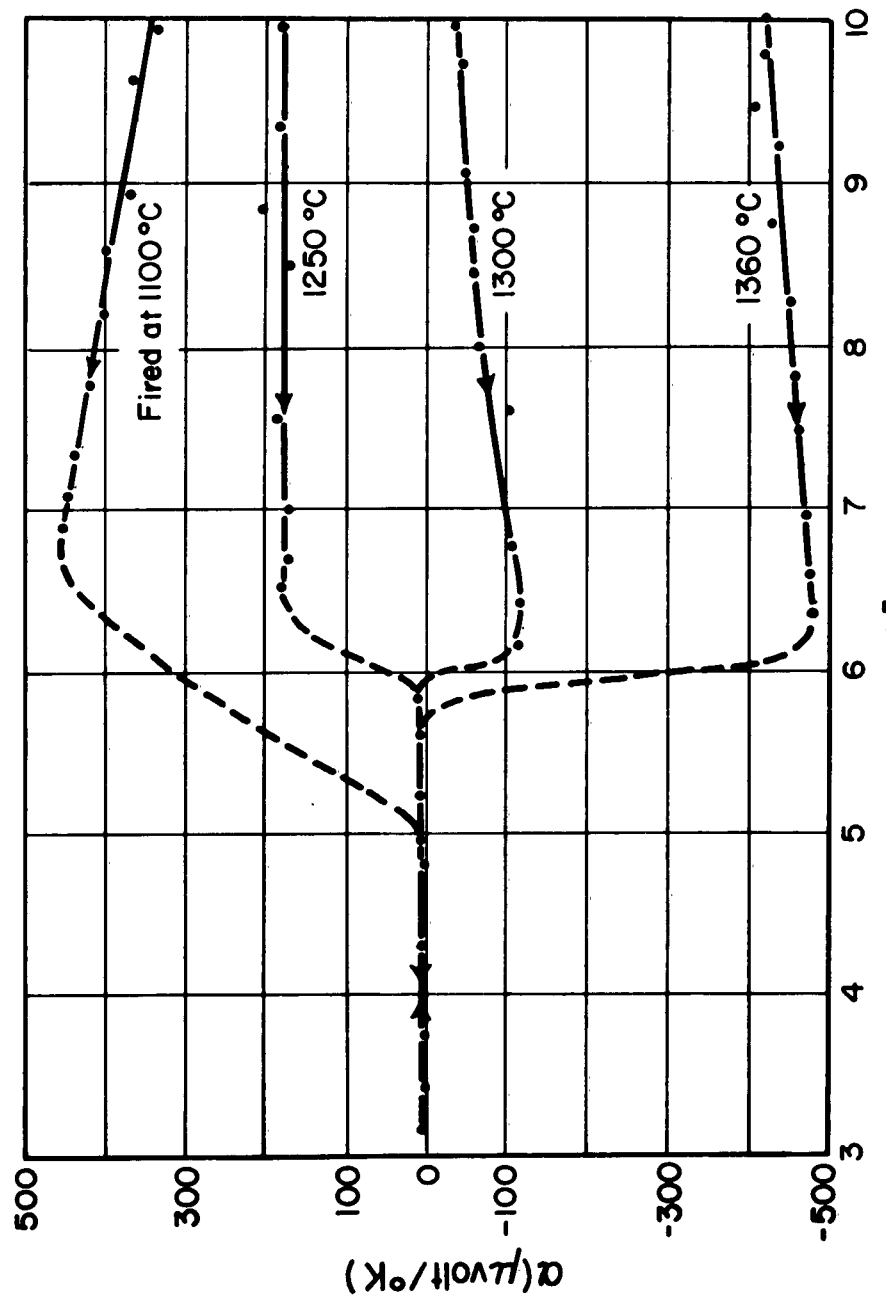

Fig. 9.2. Seebeck coefficient for V_2O_3 samples.

low-temperature transition, we find p-type conductivity for samples fired at low temperature, n-type behavior for samples fired at high temperature. Thus, where semiconducting behavior occurs the properties depend critically upon the extent to which the samples are reduced. However, the room-temperature behavior is insensitive to the details of firing, and one must, therefore, conclude that the observed p-type behavior is an intrinsic property of V_2O_3.

We have also examined the properties of V_2O_3 as a valence controlled semiconductor. The substitution of small amounts of Mg^{2+} into V_2O_3 to form the composition $Mg^{2+}_{2x}\ V^{4+}_{2x}\ V^{3+}_{2(1-2x)}\ O_3$ results in high conductivity in the low-temperature phase (Fig. 9.3.) The thermoelectric power is found to be positive in agreement with the concept of holes being created by V^{4+} cations in a V^{3+} lattice. The introduction of Zr^{4+} to form $Zr^{4+}_{2x}\ V^{2+}_{2x(1-2x)}$ also results in high conductivity at low temperature but now the thermoelectric power is negative (Fig. 9.4) because of the creation of V^{2+} donors in the V^{3+} lattice.

The reduction in the value of resistivity in the low-temperature phase accompanying Mg and Zr additions is in good agreement with the assumption that each added cation contributes one free carrier.

Compared to the low-temperature behavior the effect of additions on the room temperature conductivity is slight, presumably because the number of additional carriers are small compared to those inherently present.

The magnetic behavior of the doped compounds is unusual (Fig. 9.5.) Both Mg^{2+} and Zr^{4+} are closed shell ions and, therefore, in themselves give no paramagnetic contribution; thus, we would, at first sight, expect a simple dilution of the paramagnetism of V_2O_3 upon adding either ion. For both ions, however, concentrations of 4 mole percent cause a 50 percent increase in susceptibility above that of pure V_2O_3. Goodenough[22] has suggested that in V_2O_3 below the transition the vanadium d-electrons tend to pair off in bonding and that consequently, the net localized moment is extremely low (as is borne out by neutron diffraction results.)[23] Closed shell ions would not fit into such a pairing scheme and could conceivably effect the partial break-up of d-electron pairs, thereby, increasing the localized moment. The fact that the susceptibility above the transition is also increased suggests that here too the added closed shell ions act to decouple paired-off spins.

---

[22] J. B. Goodenough, J. Appl. Phys. Supplement to V. 31, 359S (1960).
[23] A. Paoletti and S. J. Pickart, J. Chem. Phys. 32, 308 (1960).

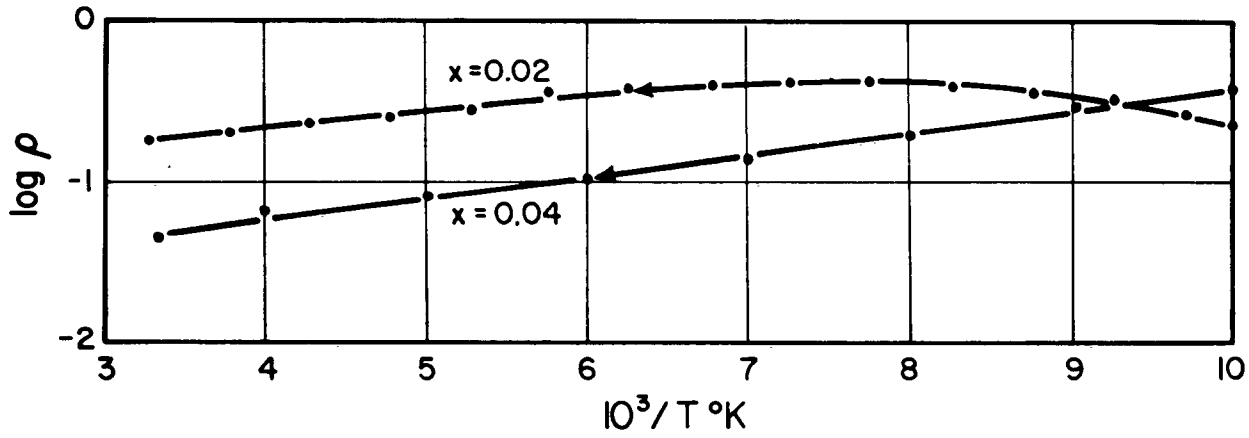

Fig. 9.3. Resistivity as a function of temperature for $Mg_{2x}V_{2(1-x)}O_3$ samples fired at 1360°C.

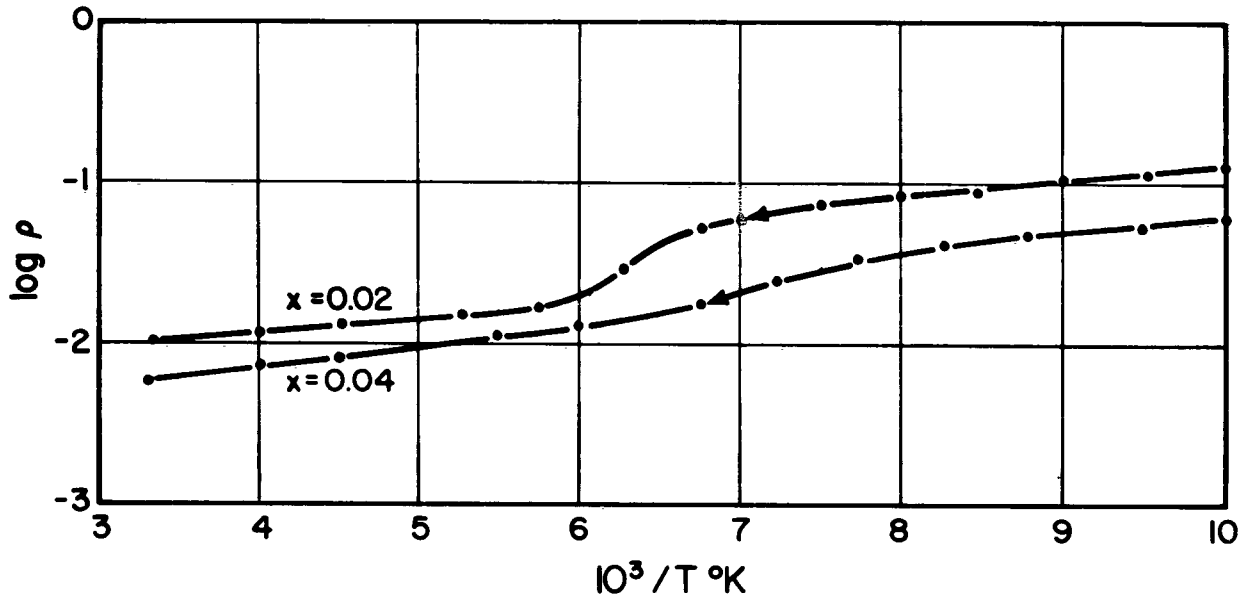

Fig. 9.4. Resistivity as a function of temperature for $Zr_{2x}V_{2(1-x)}O_3$ samples fired at 1360°C.

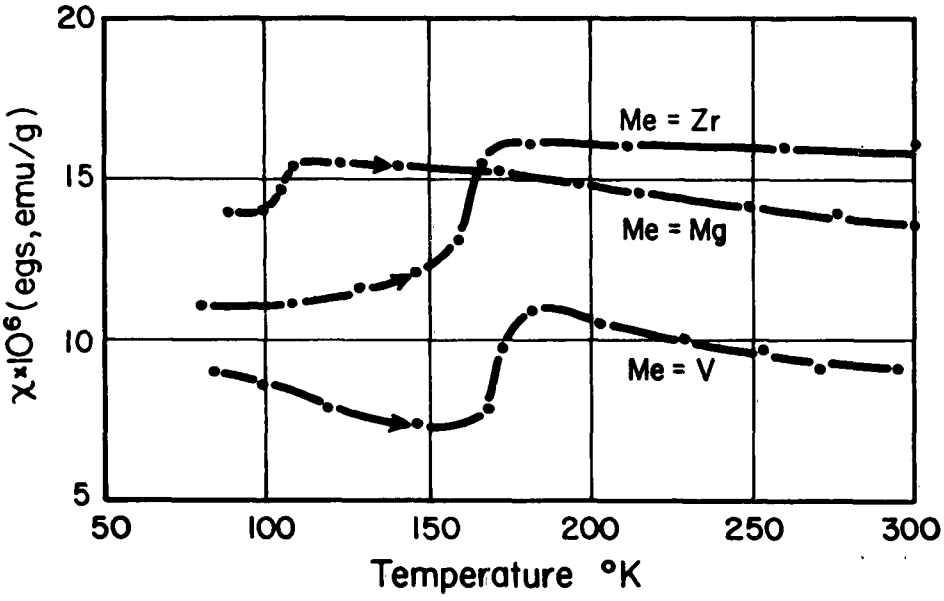

Fig. 9.5. Susceptibility as a function of temperature for compositions $Me_{0.04}V_{1.96}O_3$ fired at 1360°C.

It is to be noted that the impurity ions depress the transition temperature. This result is typical of the effect that impurities have on a first order transformation.

The metals Mg and Zr exhibit solid solubility in V_2O_3 only for small additions. However, Al, Cr, and Ti, each of which forms a sesquioxide with corundum structure, may be substituted for vanadium in any desired proportion. Because of the relative ease of substitution and because we were looking for the possible occurrence of impurity semiconduction within a d-band, the systems.

V_2O_3 - Cr_2O_3, V_2O_3 - Ti_2O_3 and V_2O_3 - Al_2O_3 were investigated in some detail.

Resistivity measurements for the series $Cr_{2x}V_{2(1-x)}O_3$, $0 \leq x \leq 0.5$, fired at 1300°C, are shown in Fig. 9.6. The resistivity above the transition increases sharply from 10^{-2} ohm-cm to 50 ohm-cm after the introduction of only 2 mole-percent chromium. With increasing Cr content the resistivity continues to increase and the character of the conduction process (as indicated by the temperature coefficient of resistivity) changes from metallic to semiconducting. The low-temperature region is less markedly affected by Cr substitution and it is only after 13 percent addition that significant changes in resistivity occur. It should be noted that Cr in concentrations less than 10 percent raises the temperature of transition.

The thermoelectric power (Fig. 9.7) of samples with Cr additions can be either positive or negative, both above and below the first order transition, depending upon the temperature of firing. It appears that the carrier concentration is controlled by deviations from stoichiometry in both phases in contrast to the behavior found for pure V_2O_3 where only the low temperature phase was found to be sensitive to firing temperature.

Resistivity behavior in the series $Al_{2x}V_{2(1-x)}O_3$ is quite similar to that for Cr substituted compounds (Fig. 9.8.)

The addition of titanium to V_2O_3 produces effects very different from those observed with Cr and Al. The substitution of Ti lowers the resistivity of the low temperature phase to values characteristic of the room temperature phase (Fig. 9.9). With large Ti additions the transition disappears entirely and the system takes on the characteristics of Ti_2O_3.

In contrast to the behavior found with Cr and Al substitutions, Ti causes a lowering of the transformation temperature.

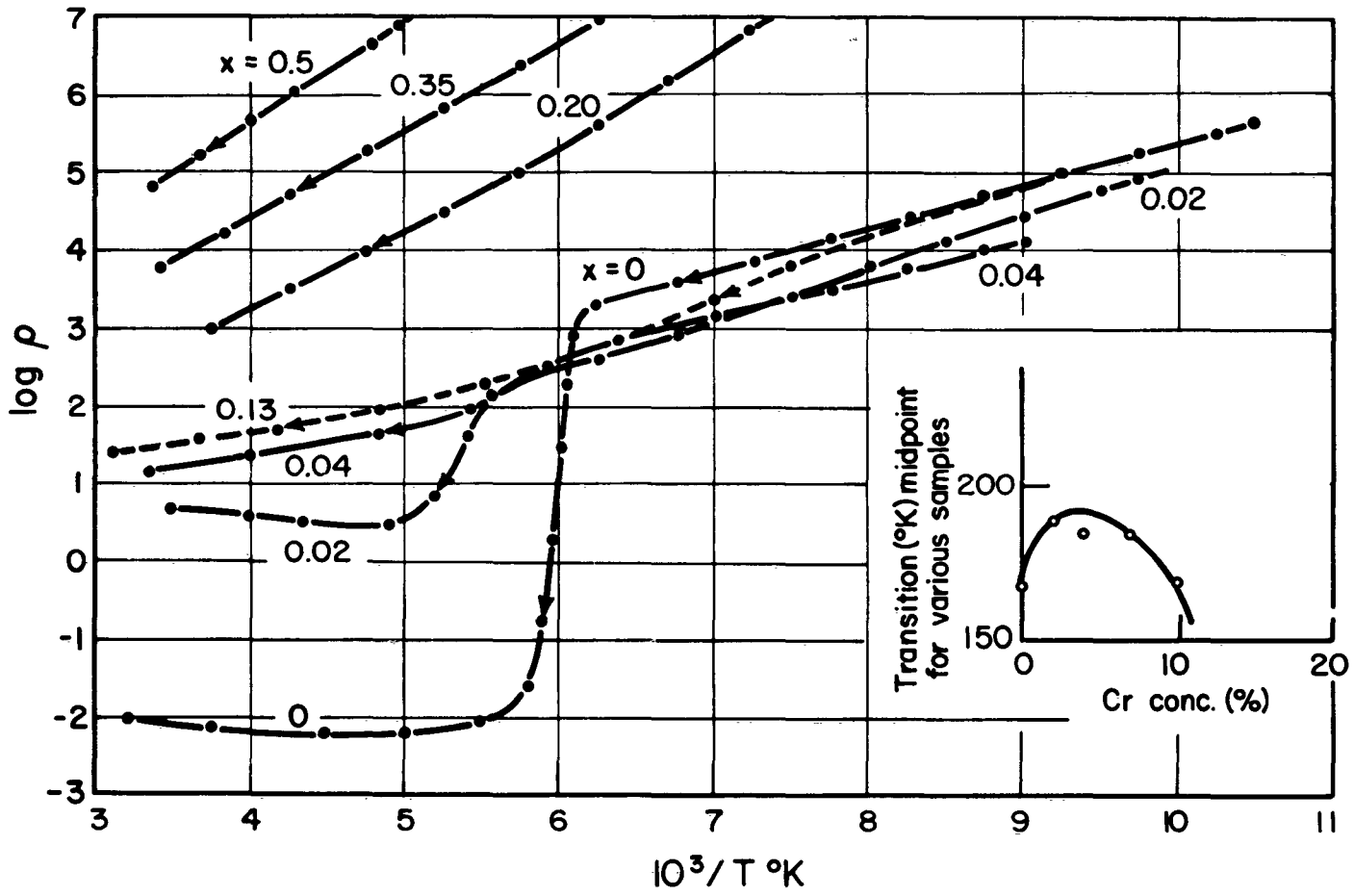

Fig. 9.6. Resistivity as a function of temperature for the series $Cr_{2x}V_{2(1-x)}O_3$ fired at 1300°C.

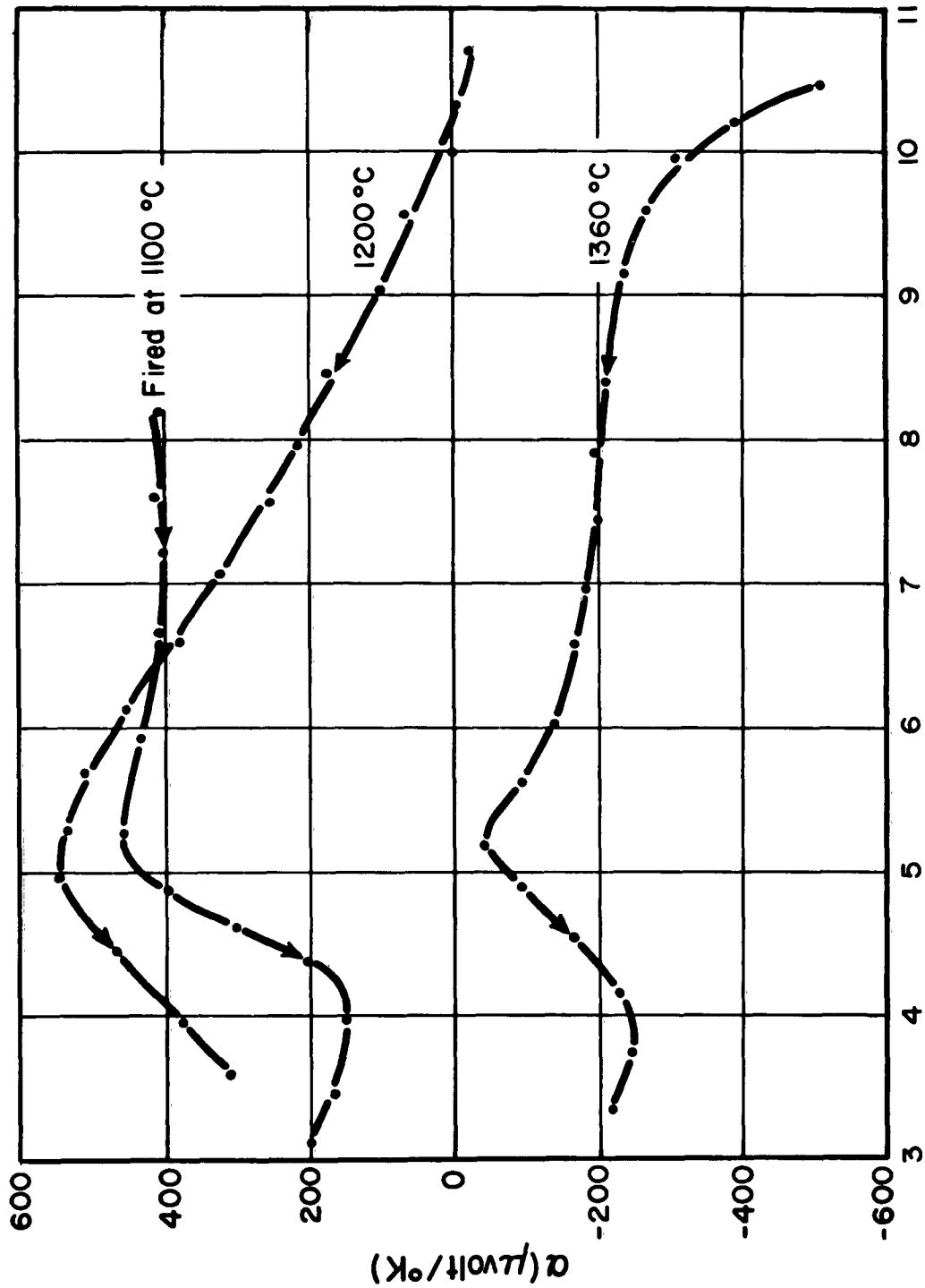

Fig. 9.7. Thermoelectric power for $Cr_{0.08}V_{1.92}O_3$ samples.

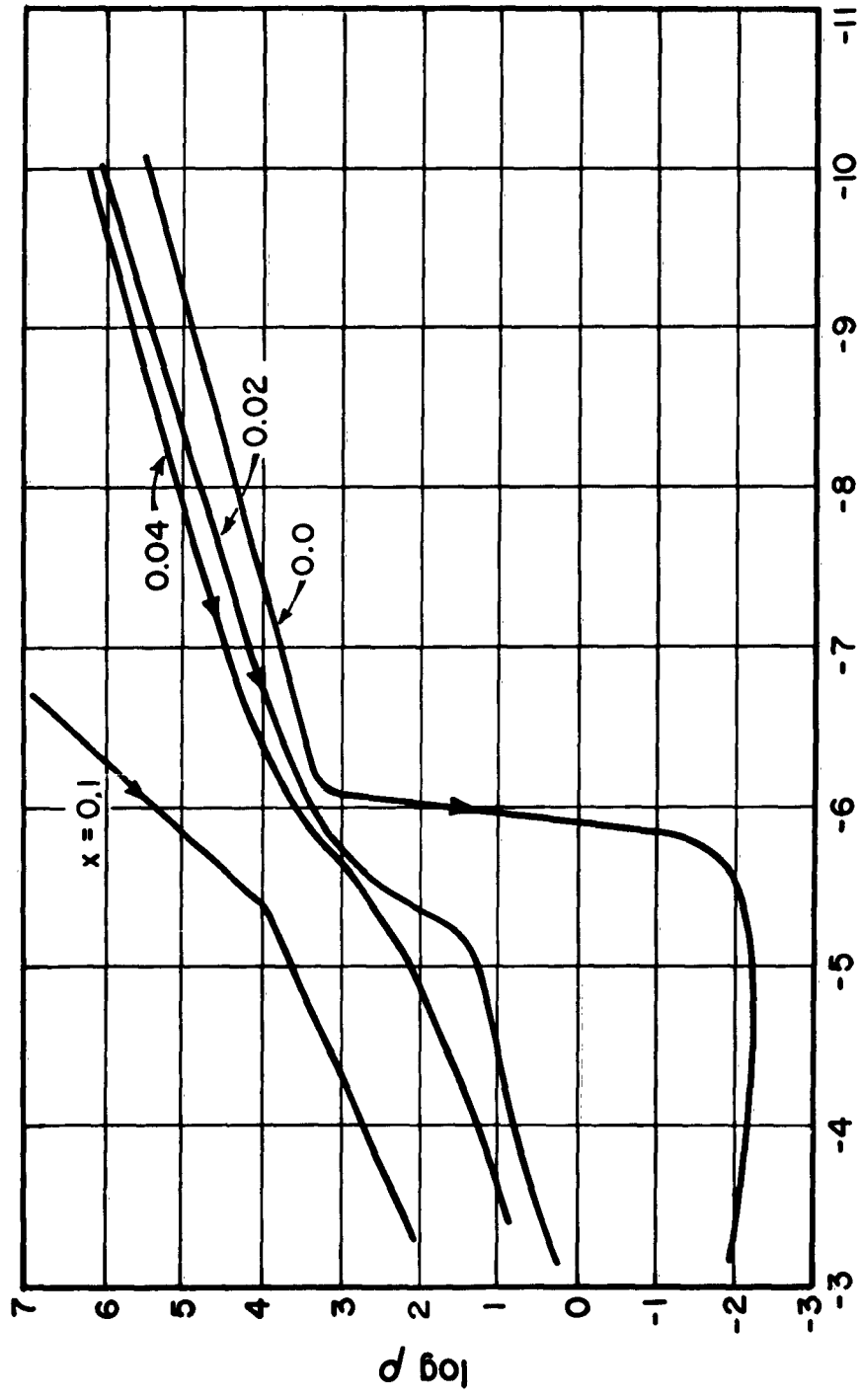

Fig. 9.8. Resistivity as a function of temperature for the series $Al_{2x}V_{2(1-x)}O_3$.

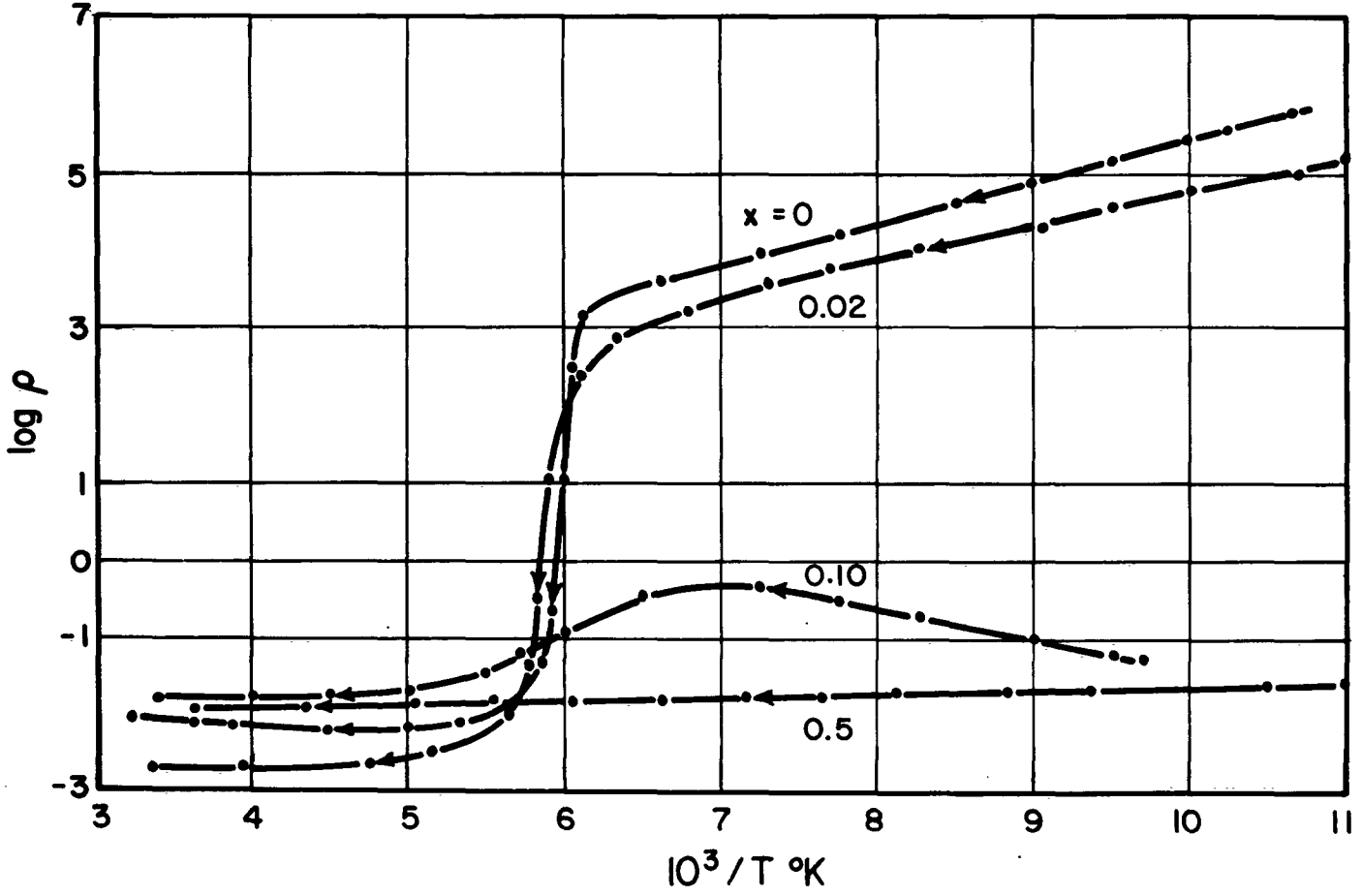

Fig. 9.9. Resistivity as a function of temperature for series $Ti_{2x}V_{2(1-x)}O_3$.

9.2 Conductivity Studies on TiO_2 *

The dependence of the conductivity of TiO_2 upon its state of oxidation was studied at elevated temperatures using a procedure due Tannhauser.[24] In this method, we started with a thin strip of pure metal (thickness about 0.1 mm) cut to the shape shown in Fig. 9.10. After platinum leads were attached by welding, the sample was heated in a controlled oxygen atmosphere. Continuous control of partial pressure of oxygen from one atmosphere to 10^{-13} atmospheres was obtained by using O_2, $O_2 + CO_2$ and CO_2 and CO gas mixtures, the total pressure always being kept at one atmosphere.

The metal was first brought to its highest oxidation state by heating in CO_2 to 1450°C, followed by an anneal in one atmosphere of pure oxygen for several hours at this same temperature. The partial pressure of oxygen was then slowly reduced in steps by introducing suitable gas mixtures.

Conductivity measurements were made using an a. c. four-terminal method.[24] At the high temperatures used, the equilibrium conductivity was established relatively soon after the partial pressure of oxygen was changed, the time varying from 10 to 45 minutes depending on the exact temperature. To enable an X-ray structure determination to be made, a dummy sample was hung near the conductivity specimen and arrangements were made to quench the dummy to room temperature at a selected point in the reduction process.

This procedure has been applied successfully by Tannhauser in his studies of the conductivity of iron oxides. Tannhauser was able to start with pure iron which he oxidized to hematite and then proceeded to reduce to magnetite, wüstite and, finally, to iron again.

In the present work, the starting material was 99.84 percent pure titanium metal which was oxidized to TiO_2 as described above. During reduction, a dummy sample was quenched at various stages and X-ray powder patterns of the resultant products were taken. It was found that in the range 1100-1450°C all compositions conformed to the rutile structure.

The conductivity measurements on five different samples of TiO_2 at different temperatures yielded five isotherms as shown in Fig. 9.10, where the conductivity is plotted as a function of $\log_{10} P_{O_2}$. At low temperatures the plot of log vs. $\log_{10} P_{O_2}$ can be approximated by two straight lines. At high temperatures the plot is almost a straight line conforming to the relation

---

* A more complete description of this work is contained in an M. I. T. Master's Thesis, Course VI, "Semiconducting Properties of Titanium Oxides", N. G. Anantha, August, 1960.

[24] D. S. Tannhauser, M. I. T. Laboratory for Insulation Research Technical Report 153 (1960).

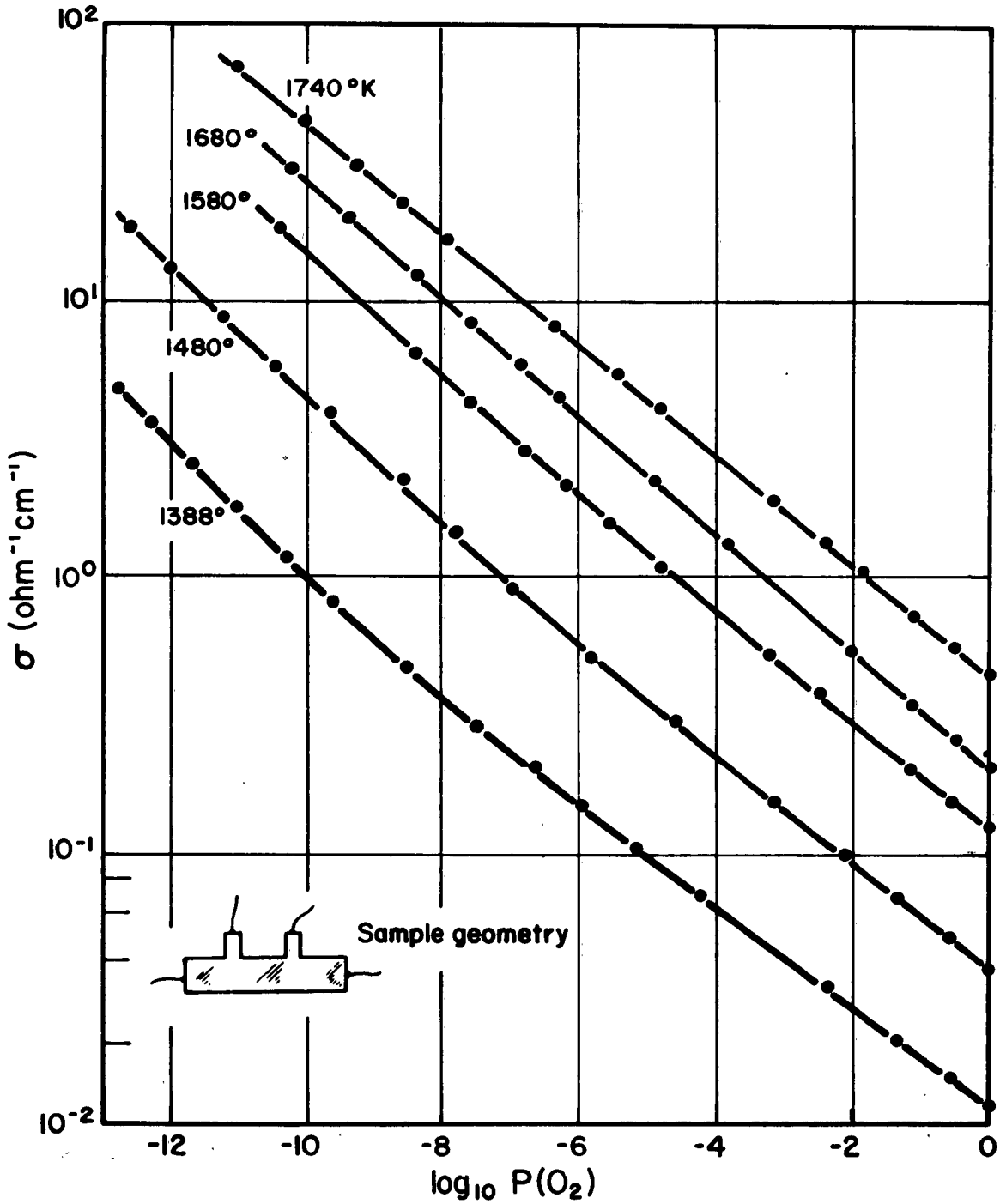

Fig. 9.10. Conductivity isotherms for TiO_2 as a function of partial pressure of oxygen (in atmospheres).

$$\log \sigma = A - B \log_{10} P_{O_2} \qquad (9.1)$$

where B = -1/5. Similar results have been reported by Hauffe.[25] Several models for the oxidation-reduction process in rutile have been proposed which predict a value B = -1/6.[26] Buessem and Butler,[27] for example, suggest that the oxidation-reduction is governed by a reaction in which the ionic components of the lattice dissociate to form free oxygen which is lost from the crystal leaving behind anion vacancies (AV) and Ti^{3+} ions:

$$2Ti^{4+} + O^{2-} \rightleftharpoons (AV) + \frac{1}{2} O_2 + 2Ti^{3+} \qquad (9.2)$$

When the law of mass action is applied to this reaction we find that the concentration of Ti^{3+} cations varies as the -1/6 power of the free oxygen concentration. These cations acting as donors become fully ionized at high temperature and, consequently, the conductivity, too, should exhibit the -1/6 power dependence and should be n-type. The latter prediction is consistent with the thermoelectric data that we have obtained (Fig. 9.11.) However, as has been pointed out by von Hippel et al[26] this model is by no means unique, and much detailed work is required if the choice of model is to be narrowed down.

In Fig. 9.12, the conductivity is plotted against 1/T for various oxygen pressures. From the plot it is seen that the activation energy (ca. 2ev) is independent of the concentration of charge carriers, which suggests that the donor levels are localized and do not overlap to form a band.

10. INSTRUMENTATION

Two major instruments were constructed under the subject contract. One of these, a vibrating-sample magnetometer, provides for the accurate and rapid measurement of susceptibility and magnetic moment. The other, a self-balancing torque magnetometer, has been an indispensable tool in our studies of field-induced anisotropy in garnets. The two instruments are described below.

---

[25] See review article by F. A. Grant, Revs. Mod. Phys. 3, 646 (1959).

[26] A. Von Hippel, J. Kalnajs and W. B. Westphal, MIT Laboratory for Insulation Research Technical Report 164, June 1961.

[27] W. R. Buessem and S. R. Butler, "Kinetics of High Temperature Processes", W. D. Kingery, Ed., The Technology Press of M. I. T. and John Wiley and Sons, N. Y., 1959, pp. 13 ff.

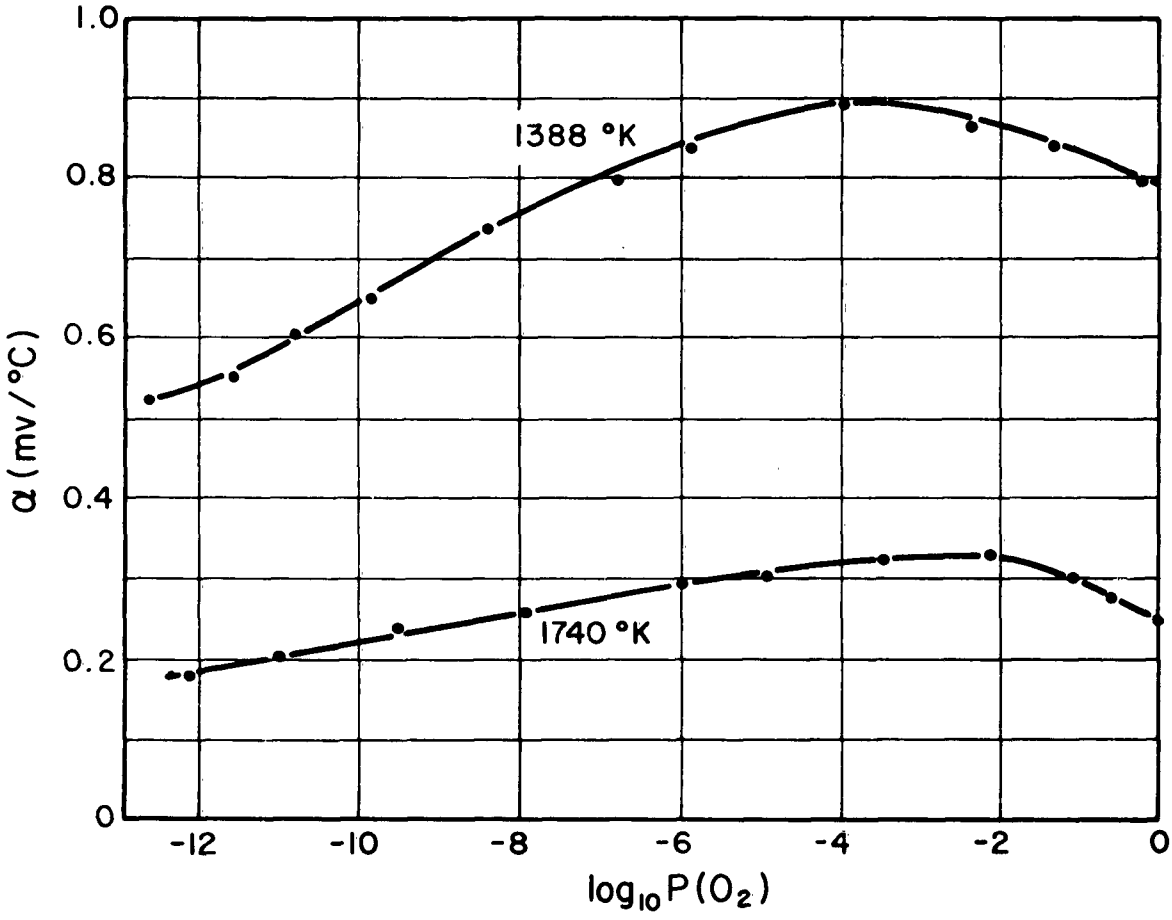

Fig. 9.11. Thermoelectric power of TiO_2 as a function of oxygen pressure (in atmospheres).

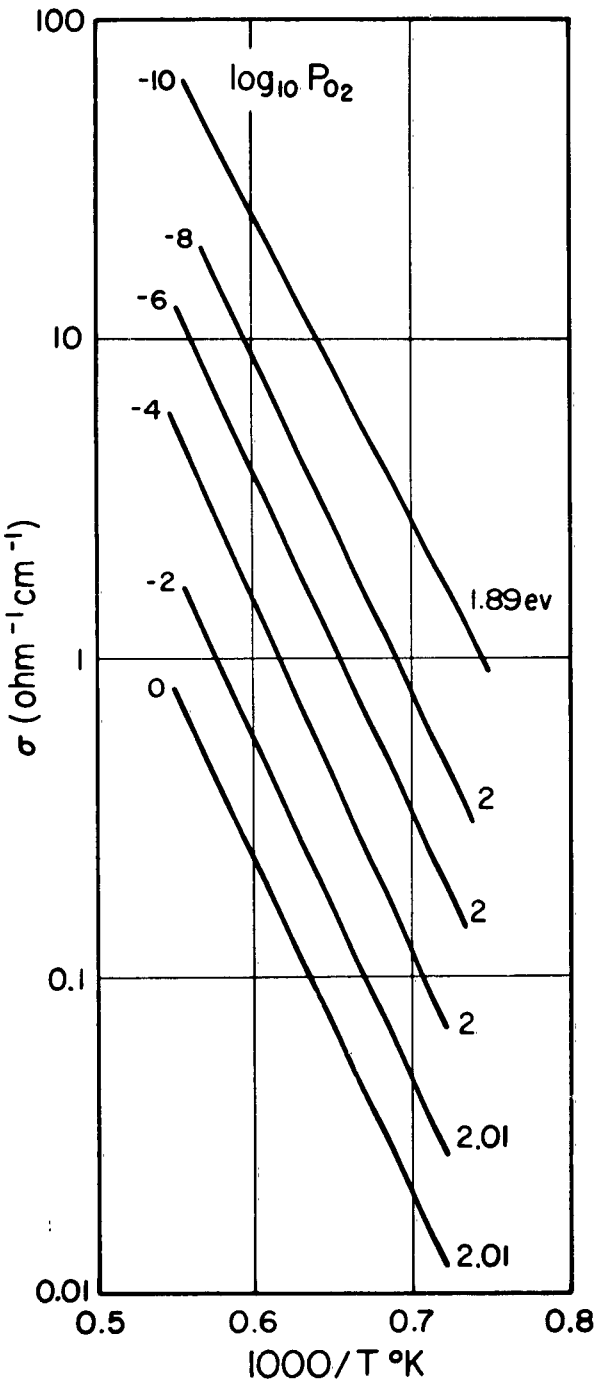

Fig. 9.12. Conductivity of TiO_2 as a function of reciprocal temperature for various oxygen pressures. Activation energy ranges from about 1.9 to 2 ev.

10.1 Vibrating-Sample Magnetometer

10.1a General Description

The instrument described in this section is a vibrating-sample magnetometer, similar to one developed by Foner[28]. It is used to measure the magnetic dipole moment existing in a magnetic sample which is at a known temperature in a known polarizing magnetic field. Proper interpretation of the magnetic moment, as a function of both the sample temperature and the applied field, enables us to obtain such properties as spontaneous moment, magnetic susceptibility, Curie constant, etc.

The material to be measured may be in the form of solids or powders. The solids, such as metals, crystals, or sintered preparations, are simply fastened to an appropriate sample holder. If desired, single crystals may be oriented with respect to the applied H field. Powdered materials may be packed into small capsules or pressed in a die to obtain samples which may be handled as solids.

The vibrating-sample magnetometer has several design features which make it attractive for laboratory use. First, the sample need not be large. Sample size is typically a 1/8" cube; it is never more than 1/4" cube and is occasionally less than a cubic millimeter for a magnetically "strong" sample. Second, there is no need for any special configuration of applied field, as required, for example, in some gradient-type magnetometers; a field of reasonable uniformity is entirely adequate. Third, the output of the instrument is directly proportional to the magnetization of the sample. A single multiplying factor determined by previous measurement of a standard material corrects all readings to actual magnetic moment in the desired system of units.

A block diagram of the instrument is shown in Fig. 10.1 and the mechanical arrangement in Fig. 10.2. The sample is attached to the lower end of a long phenolic resin rod which is vibrated vertically at 90 cps. Mechanical drive is provided by attaching the rod at its upper end to the cone of a small speaker. The sample, when magnetized, develops a magnetic moment, and the resulting dipole field, moving with respect to a pair of nearby 10,000 turn coils, induces in these coils an a.c. voltage proportional to M and to the amplitude of vibration. A reference signal proportional to the vibrational amplitude is obtained from a second set of pick-up coils excited by a ferrite permanent magnet attached to the vibrating shaft but located well outside the main magnetizing field. Each of these signals is amplified and the reference signal is

---

[28] S. Foner, Lincoln Laboratory Report M82-2.

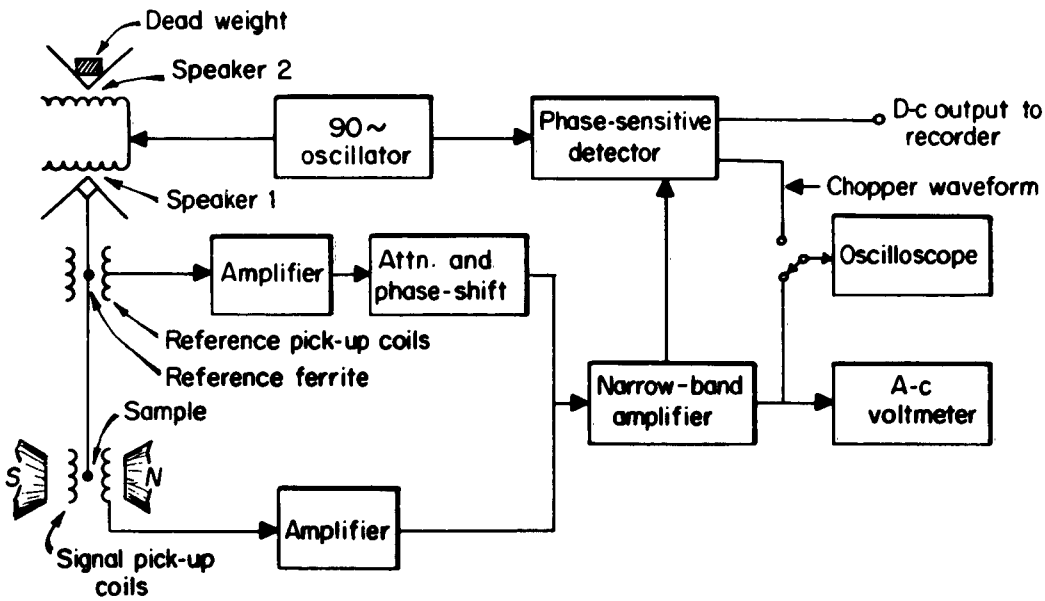

Fig. 10.1 - Block diagram of vibrating sample magnetometer

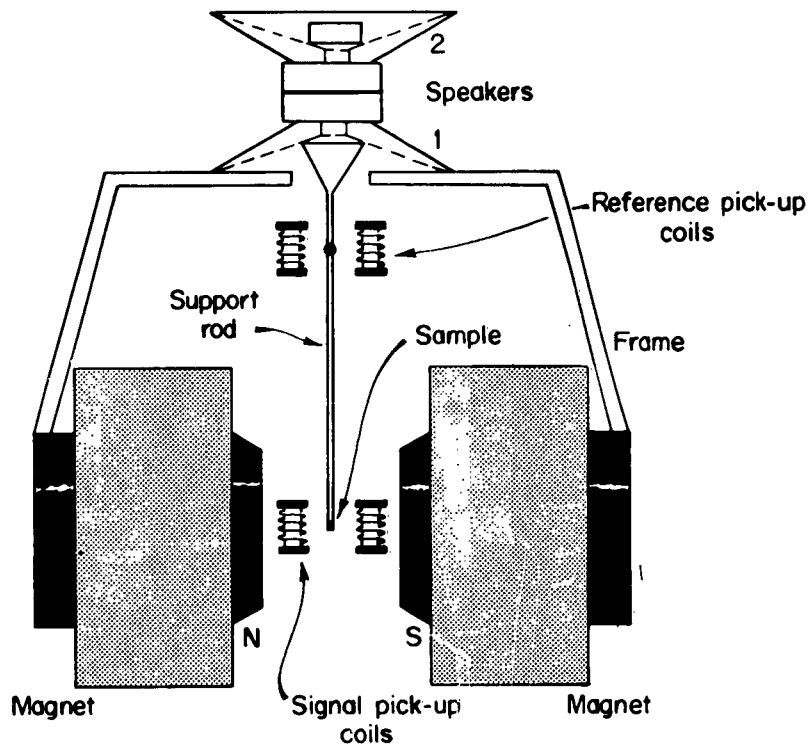

Fig. 10.2 - Basic mechanical features of vibrating sample magnetometer

passed through an attenuator and phase shifter. In one mode of operation the sum of the two signals is fed to a narrow band amplifier and monitored with an a.c. voltmeter. The amplitude and phase of the reference signal are varied to produce a null on the voltmeter, and the magnitude of M is then proportional to the reference amplitude setting. In the other mode of operation, the reference signal is not used and the sample signal is rectified by a phase sensitive detector to furnish a D-C output for automatic recording.

A second speaker, shown in Fig. 10.2 driving a dead weight, is included to minimize the excitation of mechanical vibrations in the supporting framework.

10.1b Equipment for Use at Low Temperature

For operation between 80°K and room temperature, the apparatus of Fig. 10.3 is used. The vibrating part of the system is completely enclosed so the area around the sample can be evacuated and refilled with dry nitrogen. This procedure eliminates ice formation and spurious signal due to paramagnetic liquid oxygen. The sample is cooled by liquid nitrogen in the long, slim neck of a dewar flask. The dewar is guided into position by a block of polystyrene foam, and is supported by an elevating mechanism so it may be adjusted to any desired height. After a sample has been cooled to liquid N_2 temperature, the Dewar can be lowered as much as is necessary to establish the desired rate of rise to room temperature.

The temperature of the sample is measured by means of a copper-constantan thermocouple situated in the sample holder. An ice-bath reference junction is used. When desired, the thermocouple output may be used to drive the X-axis of an X-Y recorder, and plots of magnetization vs. temperature may be made automatically.

Measurements may be made at temperatures between 4°K and 55°K with the apparatus shown in Fig. 10.4. In this arrangement the sample is located in the center of a cylindrical chamber machined from lucite. The enclosed space above the sample is maintained at a controlled partial vacuum by means of an external vacuum pump and a needle valve. The partial vacuum pulls cold helium gas up the thin Cu-Ni tube, into the lucite chamber, and around the sample, thus cooling the sample. The lucite chamber, although small (outer diameter $\approx 0.4''$), is designed to allow as much turbulence and as much opportunity for heat exchange as possible, to provide a near isothermal environment for the sample. The temperature at the sample is regulated by manipulation of the needle valve. As long as the liquid helium level is above the end of the thin gas supply tube, it is always possible to reduce the sample temperature to 4.2°K. Thermal insulation for the sample chamber is provided by the long neck of the helium dewar. The maximum temperature for this apparatus is roughly 55°K,

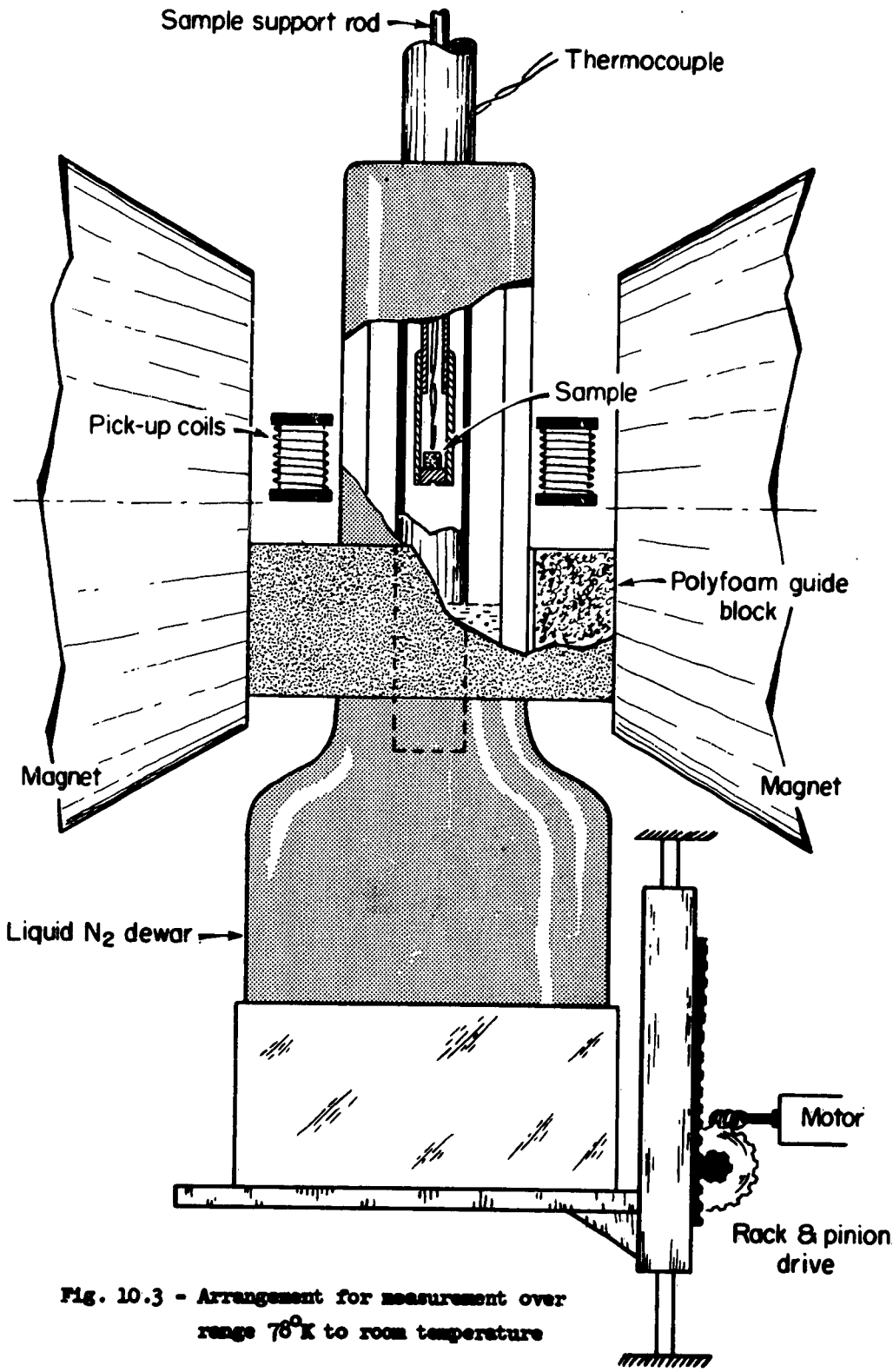

Fig. 10.3 - Arrangement for measurement over range 76°K to room temperature

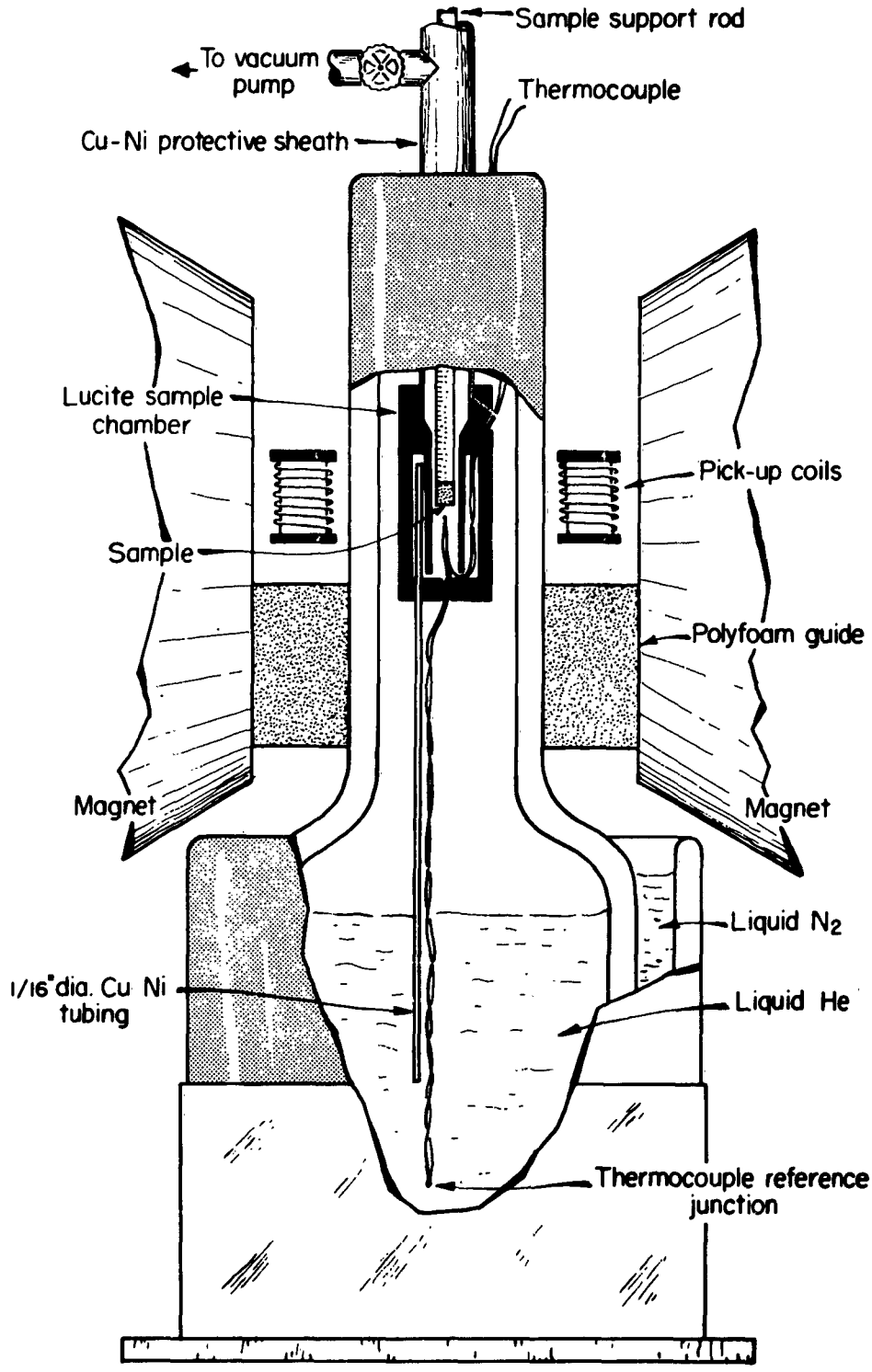

Fig. 10.4 - Auxiliary apparatus for measurement over range 4-55°K

at which temperature the nitrogen which has collected and frozen in the dewar neck above the helium is melted by the sample chamber and falls into the helium. This causes the remainder of the helium to evaporate, terminating the experiment. The elevator mechanism is used only to raise the dewar into place.

The temperature of the sample is measured with a copper-constantan thermocouple located in the gas stream just below the sample. Since the thermocouple junction is not in direct contact with the sample, it is necessary to maintain enough gas flow to insure thermal equilibrium within the chamber. The reference junction is immersed directly in liquid helium.

10.1c Equipment for Use at High Temperature

For measurements at higher than room temperatures, a sample holder machined from solid silver is used. A heater, consisting of a non-inductive platinum winding on a cylindrical ceramic form, surrounds the sample holder, and is itself surrounded by a water jacket. If the temperature is to exceed 300°C, a platinum-rhodium vs. platinum thermocouple is used in place of the copper-constantan thermocouple.

10.1d Performance Specifications for Magnetometer

Maximum available H field (2" gap)	12.8 Kgauss
Minimum observable moment	3×10^{-3} emu or
	3×10^{17} aligned spin moments
Reproducibility	$\pm$ 1 percent for moment>10^{-2}emu
Temperature range	4.2°K to 55°K
	55°K to 300°K
	300°K to 875°K

10.2 Torque Magnetometer

10.2a General Description *

We have designed and constructed a magnetometer that measures the torque

---

* A more complete description plus detailed design data is given by R. P. Hunt in Technical Report 155, M. I. T. Laboratory for Insulation Research, Oct. 1960.

on a magnetic sample automatically and continuously as a function of the direction of the applied field. The instrument is basically a self-balancing torsion balance which substitutes an electronic feedback system for the torsion fiber. The essentials of the unit are shown in Fig. 10.5.

The field applied to the crystal is provided by a Varian six-inch magnet, mounted on a gun-sight mount so that the field may be rotated about a central axis at the midpoint of the magnet's gap. A ten-turn potentiometer coupled to the magnet provides an electrical signal, proportional to the magnet's angular position, which may be used to drive the X axis of an X-Y recorder.

The sample is placed at the midpoint of the air gap and is suspended by a shaft, on the upper end of which is attached a d'Arsonval type coil assembly, similar to that described by Penoyer,[29] which is situated between the poles of a small magnetron magnet. The coil and suspension mechanism pivot on a jewel bearing; the shaft is guided by a Teflon knife-edge bushing to reduce friction.

Below the coil assembly a small galvanometer mirror is fixed to the shaft. Light from a stationary source is directed by the mirror onto the cathodes of a dual phototube, which is the input electrical stage of a balancing amplifier. The beam is adjusted so that normally an equal amount of light flux falls on each cathode. When a torque is applied to the sample shaft, the beam is displaced to one side of the phototube. The latter "senses" the displacement of the shaft and produces an error voltage proportional in magnitude and sign to the displacement. The amplifier converts the error signal to a d-c restoring current which is fed to the balancing coil. The torque developed by the balancing coil is equal but opposite to the applied torque of the crystal. A direct measure of this applied torque is the coil current, which is then plotted on the Y axis of the X-Y recorder.

With this apparatus the torque exerted by a crystal sample versus the angle of the applied field can be plotted easily and quickly. The angle of the field may be readily related to the crystallographic axes, which are known as priori, e.g., from X-ray measurements.

The instrument is capable of measuring torques from 5 to 20,000 dyne-cm, over several ranges, with a full-scale accuracy of $\pm$ 2 percent.

10.2b Temperature Control

Temperature control equipment has been provided to give a temperature range

---

[29] R. F. Penoyer, "An Automatic Torque Balance", IBM Technical Publication (1957).

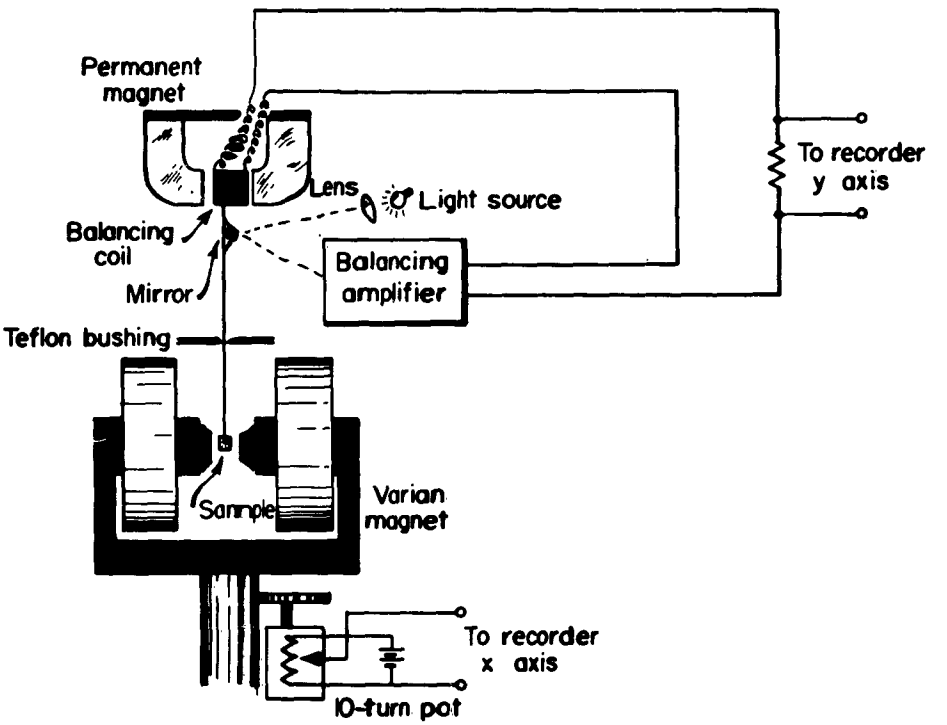

Fig. 10.5. Basic elements of self-balancing torque magnetometer.

from 66°K to about 700°K with a long time stability (ca 15 minutes) of about 1°. Temperatures from 77°K to 300°K are achieved by raising a liquid nitrogen filled dewar up around the sample and making use of the natural temperature gradient. The sample is enclosed in a copper-nickel jacket to provide uniformity of control and eliminate mechanical interaction of the boiling nitrogen with the sample shaft. The range from 66°K to 77°K is attained by pumping out over the nitrogen. Temperatures above 300°K are achieved with a ceramic heating element. Temperature measurement is by means of a thermocouple attached directly to the sample. The leads are taken off the shaft and dipped into two pools of mercury to provide torque-free transfer of the thermocouple voltage.

10.2c Application of the Instrument

As a check on the performance of the instrument torque measurements were run on a single crystal disk of nickel (volume $\cong 6 \times 10^{-2}$ cm^3; radius = 9 mm), a material whose anisotropy is well known. A typical torque curve is shown in Fig. 10.6. Analysis of the data gives $K_1 = -50{,}000$ ergs/cm^3, a value which compares favorably with $K_1 = -49{,}000$ ergy/cm^3, the average of ten values cited by Bozorth. *

Torque, data was also taken on two single crystal samples of magnetite, one a (100) plane disk (volume $\cong 1.1 \times 10^{-2}$cm^3) and the other a sphere (volume $\cong 4.4 \times 10^{-3}$cm^3) measured in the (110) plane. The value $K_1 = 1.12 \times 10^{-5}$ obtained from these measurements is consistent with those given in the literature, which run from -0.98 to -1.20×10^5 ergs/cm^3.

A temperature run on a yttrium-iron garnet sphere * (volume $\cong 4.2 \times 10^{-3}$cm^3) was also made (Fig. 10.7.)

Data on the several single crystals is summarized in Table V.

---

* Grown in a PbO-PbF_2 flux by a process similar to that described by Nielsen.[30] The sample was obtained from Air Force Cambridge Research Center.

[30] J. W. Nielsen, J. Appl. Phys. Supplement to V. 31, No. 5, 51S (1960).

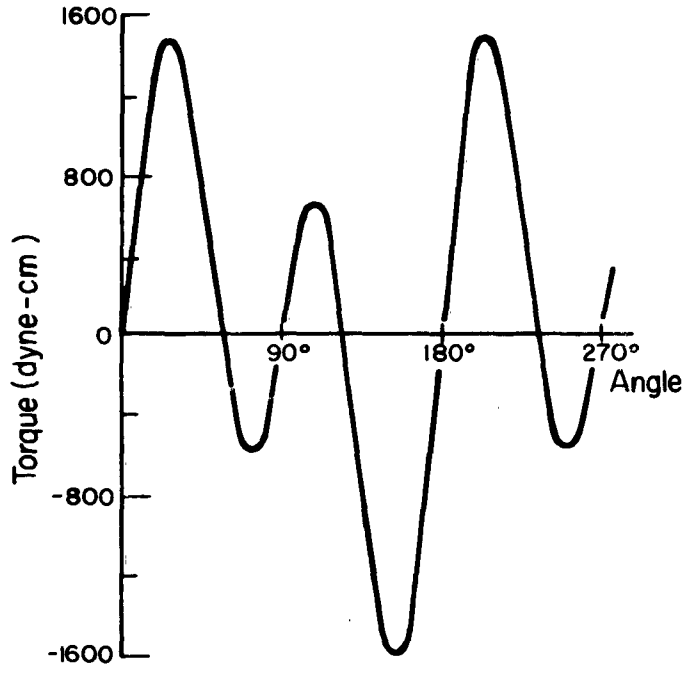

Fig. 10.6. Torque vs. angle from [100] direction for a nickel crystal in the (110) plane at 20°C.

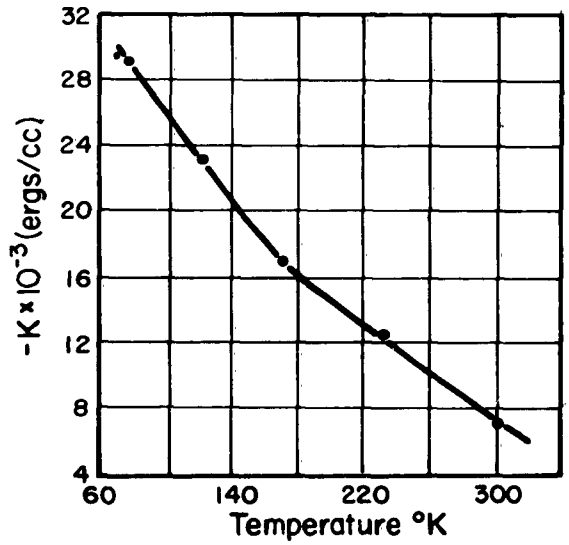

Fig. 10.7. First order anisotropy constant of YIG.

TABLE V

Anisotropy Constants for Single Crystals at 20°C

	K_1 (ergs/cm^3)	K_2 (ergs/cm^3)
Magnetite ellipsoid	-1.13×10^5	-
Magnetite sphere	-1.12×10^5	$(6 \pm 3) \times 10^4$
Nickel disk	-5.0×10^4	$(1.4 \pm 0.5) \times 10^4$
Yttrium iron garnet sphere	-6.1×10^3	$(1.0 \pm 0.5) \times 10^4$
Yttrium iron garnet disk	-6.5×10^3	$(0.5 \pm 0.5) \times 10^4$

11. BIBLIOGRAPHY

1. L. Néel, J. Appl. Phys., Supplement to Vol. 30, No. 4, 3S (1959).
2. H. P. J. Wijn and H. van der Heide, Revs. Mod. Phys. 25, 98 (1953).
3. D. J. Epstein, Conference on Magnetism and Magnetic Materials, A. I. E. E. Publication T-91, Feb. 1957.
4. A. R. Von Hippel, "Dielectrics and Waves," John Wiley and Sons, Inc., New York (1959), Ch. 31.
5. J. Smit and H. P. J. Wijn, "Ferrites," John Wiley and Sons, New York (1959), p. 244.
6. C. Kittel, Colloques Internationaux, CNRS 28, 184 (1951).
7. L. Landau and E. Lifshitz, Physik Z. Sowjetunion 8, 153 (1935).
8. W. Doering, Z. Natur. 3a, 373 (1948).
9. C. J. Kriessman, S. E. Harrison and H. S. Belson, J. Appl. Phys. 29, 452 (1958).
10. D. F. Gibbons and V. C. Chirba, Phys. Rev. 110, 770 (1958).
11. J. K. Galt, Bell System Technical J. 33, 1023 (1954).
12. A. M. Clogston, Bell System Tech. J. 34, 739 (1955).
13. B. A. Calhoun, J. Appl. Phys, Supplement to Vol. 30, No. 4, 293S (1959).
14. L. Néel, J. Phys. Rad. 13, 249 (1952).
15. C. Kittel, Revs. Mod. Phys. 21, 541 (1950).
16. J. V. Harrington, Lincoln Laboratory Technical Report 168 (1958).
17. J. F. Janak, M. I. T. Laboratory for Insulation Research Technical Report 171: in press.
18. J. F. Dillon, J. Appl. Phys. 29, 1286 (1958).
19. P. A. Miles, M. I. T. Laboratory for Insulation Research Prog. Rept. XXI, June 1957, p. 20.
20. A. Nakamura and Y. Sugiura, J. Phys. Soc. Japan 15, 1704 (1960).
21. K. H. Stewart, "Ferromagnetic Domains," Cambridge Press (1954); p. 45.
22. J. B. Goodenough, J. Appl. Phys. Supplement to Vol. 31, 359S (1960).
23. A. Paoletti and S. J. Pickart, J. Chem. Phys. 32, 308 (1960).
24. D. S. Tannhauser, M. I. T. Laboratory for Insulation Research Technical Report 153 (1960).
25. See review article by F. A. Grant, Revs. Mod. Phys. 3, 646 (1959).
26. A. Von Hippel, J. Kalnajs and W. B. Westphal, M. I. T. Laboratory for Insulation Research Technical Report 164, June 1961).
27. W. R. Buessem and S. R. Butler, "Kinetics of High Temperature Processes", W. D. Kingery, Ed., The Technology Press of M. I. T. and John Wiley and Sons, New York, 1959, pp. 13 ff.

28. S. Foner, Lincoln Laboratory Report M82-2.

29. R. F. Penoyer, "An Automatic Torque Balance," IBM Technical Publication (1957).

30. J. W. Nielsen, J. Appl. Phys., Supplement to Vol. 31, No. 5, 51S (1960).

31. K. S. Cole and R. H. Cole, J. Chem. Phys. 9, 341 (1961).

12. PUBLICATIONS UNDER SUBJECT CONTRACT

Papers

D. J. Epstein, B. Frackiewicz, and R. P. Hunt, Uniaxial Anisotropy in Polycrystalline Garnets, J. A. P. Supplement to Vol. 32, 270S (1961).

Technical Reports

B. W. Lovell and D. J. Epstein, "Dynamic Squareness in Polycrystalline Garnets", Technical Report 173, Laboratory for Insulation Research, M. I. T.

J. F. Janak, "Dynamic Behavior of Diffusion-Damped Domain Walls", Technical Report 174, Laboratory for Insulation Research, M. I. T.

A. J. MacMillan, "Properties of V_2O_3 and Related Sesquioxides", Technical Report 172, Laboratory for Insulation Research, M. I. T.

R. P. Hunt, "A Torque Magnetometer for Crystalline Anisotropy Measurements", Technical Report 155, Laboratory for Insulation Research, M. I. T., Oct. 1960.

Theses

A. J. MacMillan, "Properties of V_2O_3 and Related Sesquioxides", Sc. D. Thesis, Sept. 1961.

J. F. Janak, "Transient Behavior of Diffusion-Damped Ferromagnetic Domain Walls", S. M. Thesis, Sept. 1961.

A. S. Foster, "Magnetostriction in YIG and Other Garnets", S. M. Thesis, Jan. 1961.

N. G. Anantha, "Semiconducting Properties of Titanium Oxides, S. M. Thesis, Aug. 1960.